Challenges in the Adjoint-based Optimization of Bare Tube Heat Exchangers

G. O. Bociar

Technische Universiteit Delft

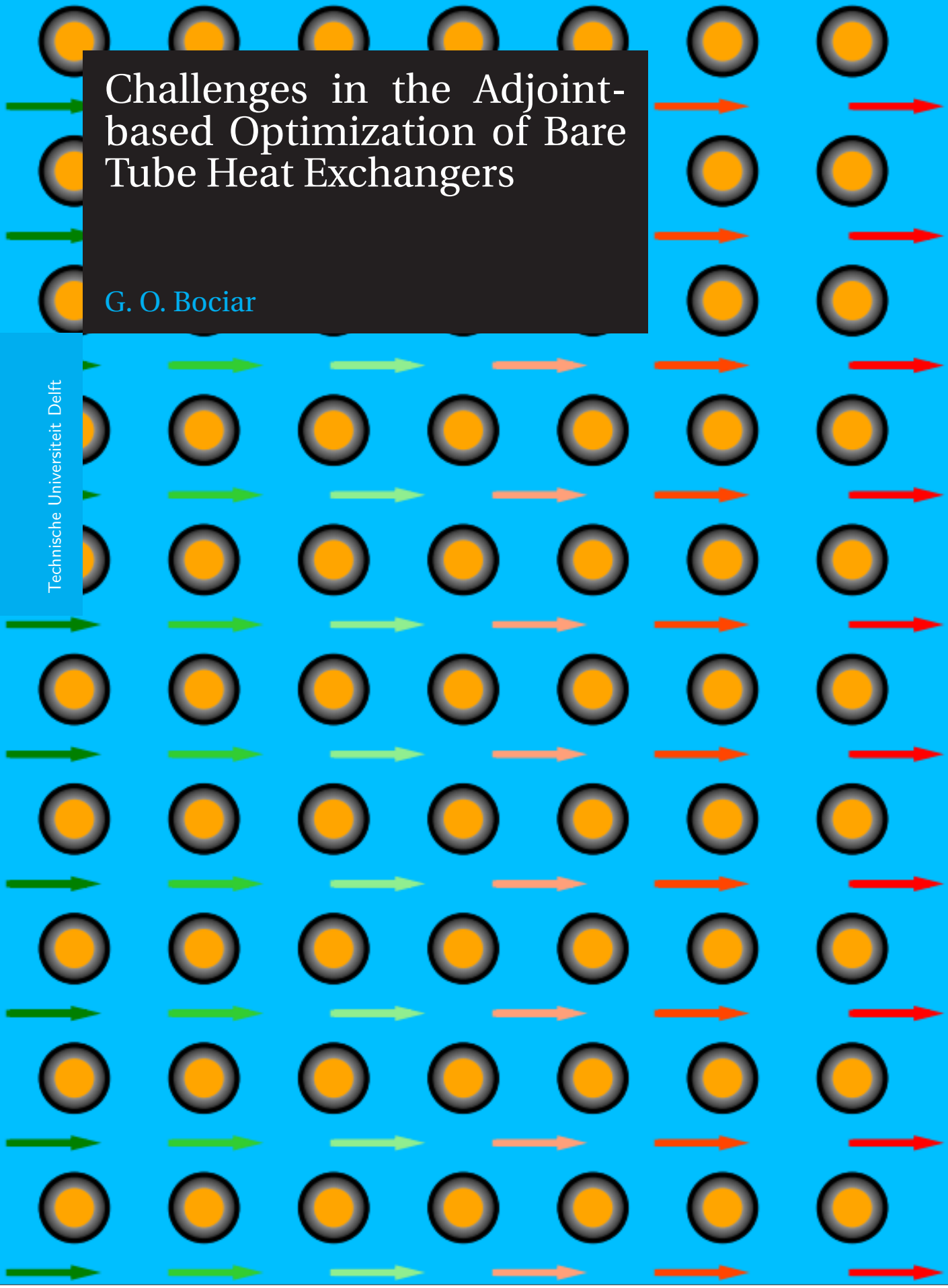

TU Delft Delft University of Technology

Challenge the future

Challenges in the Adjoint-based Optimization of Bare Tube Heat Exchangers

by

G. O. Bociar

in partial fulfillment of the requirements for the degree of

Master of Science
in Aerospace Engineering

at the Delft University of Technology,
to be defended publicly on Tuesday February 17, 2024 at 10:00 AM.

Supervisor:	Dr. ir. Carlo De Servi	
Thesis committee:	Dr. ir. Matteo Pini ,	TU Delft
	Dr. ir. Carlo De Servi ,	TU Delft
	Dr. ir. Marc Gerritsma ,	TU Delft

An electronic version of this thesis is available at http://repository.tudelft.nl/.

TU Delft Delft University of Technology

ABSTRACT

The demand for more efficient propulsion systems in the aerospace industry has driven the investigation of novel engine configurations. Many of these innovative engine configurations incorporate heat exchangers as components for thermal management. Therefore, to improve the efficiency of these new propulsion systems, it is necessary to design heat exchangers that offer the best characteristics in terms of heat transfer, pressure losses, volume and weight. With advancements in additive manufacturing, it has become possible to create bare tube heat exchangers with tubes of different shapes and dimensions that are comparable with microchannel heat exchangers in terms of thermal efficiency. Bare tube heat exchangers also have advantages in terms of weight, volume, and reduced pressure losses compared to microchannel heat exchangers, making them preferable in aerospace applications.

This thesis presents an investigation into the adjoint-based optimization of bare tube heat exchangers with the objective of minimizing air-side pressure drop. The present research focuses on the shape optimization of the tubes for an in-line bare tube heat exchanger configuration. The in-line configuration was chosen for its advantages in terms of reduced pressure drop.

The optimization process employs the adjoint method for shape optimizations and utilizes the SU2 CFD tool for flow simulations, targeting flow conditions characterized by a Reynolds number of approximately 1000. For these flow conditions, it was determined that the accuracy of CFD simulations was highly dependent on the turbulence model used. Three turbulence models (SA, SST and Realizable $k-\epsilon$) were benchmarked against a set of empirical correlations, and the Realizable $k-\epsilon$ model was determined to produce the most accurate results. However, the SU2 software, which is used for the optimization framework, only offers the SST and SA models for the CFD evaluations. As a result, the Realizable $k-\epsilon$ model was used to recompute the flow field of the optimized bare tube heat exchanger designs as a post-processing step.

The optimization was performed for both round and elliptical tubes. Despite challenges in turbulence modelling, the optimizations reduced the pressure drop (Δp) by up to 20% for round tubes, depending on the optimization algorithm used. The reduction in Δp for the optimized elliptical tubes was lower, achieving only a 10% improvement at best. However, this 10% reduction is in addition to the significant improvement that can be obtained from simply substituting round tubes with elliptical ones.

NOMENCLATURE

ABBREVIATIONS

Abbreviation	Definition
2D	two-dimensional
3D	three-dimensional
BTHX	bare tube heat exchanger
CAD	computater-aided design
CFD	computational fluid dynamics
CFL	Courant–Friedrichs–Lewy
DNS	direct numerical simulation
FEM	finite element method
FFD	free form deformation
FSI	fluid structure interaction
FV	finite volume
FVM	finite volume method
EB-RSM	Elliptic Blending Reynolds-stress model
FTHX	plate-and-fin heat exchanger
HX	heat exchanger
J	Joule(s)
K	Kelvin
kg	kilogram(s)
kW	kiloWatt(s)
LES	large eddy simulations
L.E.	leading edge
m	meter(s)
max	maximum
MCHX	microchannel heat exchanger
min	minimum
mm	millimetres
MUSCL	monotone upstream-centered schemes for conservation laws
NACA	National Advisory Committee for Aeronautics
NURBS	non-uniform rational basis spline
ORC	orgainc Rankine cycle
QUICK	quadratic upstream interpolation for convective kinematics
Pa	Pascal(s)
RANS	Reynolds averaged Navier-Stokes
RNG	renormalization group
RSM	Reynolds-stress model
s	second(s)
SA	Spalart-Allmaras
SLSQP	sequential least squares quadratic programming
SNOPT	sparse nonlinear OPTimizer
SQP	sequential quadratic programming
SSG	Speziale-Sarkar-Gatski
SST	shear stress transport

Abbreviation	Definition
T.E.	trailing edge
URANS	unsteady Reynolds averaged Navier-Stokes
W	Watt(s)
XDSM	extended design structure matrix

SYMBOLS

Symbol	Unit	Definition
A	m^2	area
A	m^2	area
a	m	semi-major axis
b	m	semi-minor axis
c	m	chord
cp	$J/kg \cdot K$	specific heat capacity at constant pressure
D	m	diameter
D_H	m	hydraulic diameter
$f(...)$	-	Function of (...)
h_c	$W/m^2 \cdot K$	heat transfer coefficient
I	%	turbulece intensity
$J(...)$	-	objective function
k_c	$W/m \cdot K$	thermal conductivity
k	m^2/s^2	turbulent kinetic energy
l	m	turbulent lenght scale
$\dot{m}$	m/s	mass flow rate
Nu	-	Nusselt Number
n_R	-	Number of tubes
p	Pa	pressure
P	m	perimeter
P_L	-	longitudinal relative pitch
P_T	-	transverse relative pitch
Pr	-	Prandtl number
$\dot{Q}$	W	heat transfer rate
$\dot{q}$	W/m^2	heat flux
R	$J/kg \cdot K$	ideal gas constant
$R(...)$	-	state equation
$\vec{r}$	-	normal vecotr
Re	-	Reynolds number
RF	-	Relaxation Factor
S_{ij}	1/s	strain rate
S_L	-	longitudinal pitch
S_T	-	transverse pitch
S_μ	K	Sutherland constant
T	K	temperature

Symbol	Unit	Definition
T_i^u	m	thickness distribution upper side
T_i^l	m	thickness distribution lower side
t	s	time
U	m/s	velocity magnitude
$U(...)$	-	state variables
u_i	m/s	velocity vector
x_i	m	coordinate vector
y^+	-	y-plus
α	-	Design variables
α_c	m^2/s	thermal diffusivity
Δ	-	Difference of
Δx	m	grid spacing
δ_{ij}	-	Kronecher delta
ϵ	m^2/s^3	Difference of
λ	-	Adjoint variable
μ	$Pa \cdot s$	dynamic viscosity
μ_t	$Pa \cdot s$	turbulent dynamic viscosity
ν	m^2/s	kinematic viscosity
$\tilde{\nu}$	m^2/s	working variable
ν_t	m^2/s	turbulent kinematic viscosity
ϕ	-	cell quantity
ξ	-	Friction factor
ρ	kg/m^3	Density
τ_w	Pa	shear stress
τ_{ij}	m^2/s^2	Reynolds stress tensor
χ	-	Factor
ω	1/s	specific dissipation rate
∇	-	Del operator
f_{v1},f_w,C_{w1},f_{t2}, C_{b2}	-	constants for the SA turbulence model
f_1,f_2,C_μ,$C_{\epsilon 1}$,$C_{\epsilon 2}$,L_ϵ,σ_ϵ	-	constants for the $k-\epsilon$ turbulence model
α_s,Ω	-	constants for the $k-\epsilon$ RNG turbulence model
A_0,A_s,C_μ	-	constants for the Realizable $k-\epsilon$ turbulence model
α,β,a_1,S,$F2$,P_k,σ_k,σ_ω,$\sigma_{\omega 2}$	-	constants for the $k-\omega$ SST turbulence model
E, κ	-	empirical constants for standard wall function

SUBSCRIPTS

Subscript	Definition
0	reference values
c	quantities computed based on tube chord
CD	central difference shceme
D	quantities computed based on tube diameter
d	downstream
$diff$	difference between two quantities
e	cell egde
err	error between the numerical and empirical quantities
i	indexing variable
j	indexing variable
in	inlet quantities
LM	logarithmic mean value
m	value at the minimum cross section
out	outlet quantities
SU	second order upwind
u	upstream
w	wall quantities
$\overline{}$	mean value
$'$	fluctuation value
∞	inflow

CONTENTS

List of Figures

List of Tables

1

INTRODUCTION

Heat exchangers (HXs) are components used to transfer heat from one fluid to another and can be commonly found as subsystems of thermodynamic cycles. The efficiency of the overall thermodynamic cycle can be greatly affected by the efficiency of the HXs utilized. To optimize energy efficiency, the design and operation of HXs are critical to achieving the desired system performance. Depending on the specific cycle requirements, HXs can serve various functions, such as acting as condensers, evaporators, or radiators. For aerospace applications, HXs can be used to improve the thermal efficiency of propulsion systems. Tanatsugu et al. [14] propose using an in-line tube bank as a hydrogen heater for an engine with a combined turbojet-ramjet architecture. Other applications of HXs in the aerospace sector, in particular for the implementation of intercooled and recuperated aero-engines are presented by Patrao et al. [15].

There are multiple design parameters that need to be tuned to obtain an optimal heat exchanger geometry. Besides the high heat transfer rate, it is also desirable to have a low-pressure drop inside the HX, which is associated with the minimization of mechanical losses in the working fluids. Minimizing the weight and volume of a HX is also desirable, especially for applications where compactness is critical.

There are multiple types of HX configurations, such as bare tube HX (BTHX), plate-and-fin HX (FTHX) or microchannel HX (MCHX). For applications such as condensers evaporators and radiators, BTHX has shown great potential for cases where compactness is necessary, such as in the aerospace industry. This was shown by the experimental studies of Huang et al. [16], who found that BTHX can achieve the same performances as louvred-fin and flat tube FTHX while having significantly less material volume. The limiting factor for the BTHX was the minimum size of the tubes. In the past, tubes of small diameters and limited thickness could not be easily manufactured. However, in recent years, it has become possible to achieve smaller tube dimensions and produce different tube shapes due to the advancements in additive manufacturing. As shown by Bacellar et al. [9], additive manufacturing technology makes it feasible to manufacture optimized tube geometries of different shapes and sizes.

1.1. IN-LINE BARE TUBE HEAT EXCHANGERS

The architecture of a BTHX is relatively simple when compared to other types of HXs. At a basic level, the BTHX is simply an array of tubes arranged in different configurations. As stated by Zukauskas [17], the two most common arrangements are staggered and in-line tube banks. These two types of arrays are displayed in Figure 1.1. Zukauskas [17] also indicates that the two configurations exhibit different flow patterns. For the staggered tubes, the flow is similar to that inside a curved channel, whereas the flow inside an in-line array is more similar to that inside a straight channel.

One of the possible applications of in-line BTHX is as an evaporator of an organic Rankine-cycle waste heat recovery system. One such application is presented by Krempus et al. [18], where an in-line BTHX is used as an evaporator for a combined cycle engine integrating a turboshaft engine with an ORC heat recovery unit. The ORC presented by Krempus et al. [18] also uses an MCHX as a condenser. As pointed out by Bacellar et al. [19], MCHXs exhibit a larger pressure drop on the air side compared to BTHXs. Therefore, the efficiency of the combined cycle engine could be improved by substituting the MCHX for a BTHX with equivalent heat transfer performance, due to the lower pressure drop on the exhaust gases of the engine. A further reduction in pressure drop can be achieved by optimizing the shapes of the BTHX tubes. To optimize the tube shape, it

is crucial to model the flow conditions on the air side of the BTHX to calculate the pressure drop. In the case of the ORC presented by Krempus et al. [18], based on the mass flow rate of air of the MCHX, the equivalent flow conditions on the air side of the BTHX correspond to $Re_D \approx 1000$. Bacellar et al. [19] also state that BTHXs can potentially be smaller in volume than MCHXs.

Of the two types of BTHX configurations, the staggered one has advantages in terms of compactness and heat transfer rate. However, the in-line configurations show a considerably smaller pressure drop on the air side at certain flow conditions. Zukauskas [17] states that for the transition region from laminar to turbulent flow, for $5 \cdot 10^2 < Re < 5 \cdot 10^4$, the in-line BTHX displays a lower pressure drop than the staggered configuration. For increasing Reynolds numbers $Re \geq 2 \cdot 10^5$, because of the increasing turbulence intensity, the pressure drop of the two array configurations tends to become comparable. At higher Reynolds numbers, the hydraulic efficiency of BTHXs is primarily determined by pitch ratios rather than flow conditions. Therefore, for flow conditions corresponding to $Re \approx 1000$, in-line BTHXs are preferable in order to minimize pressure drop. For these flow conditions, the optimal longitudinal and transverse pitches depend on the thermal and material (volume and mass) requirements of the specific application for the HX.

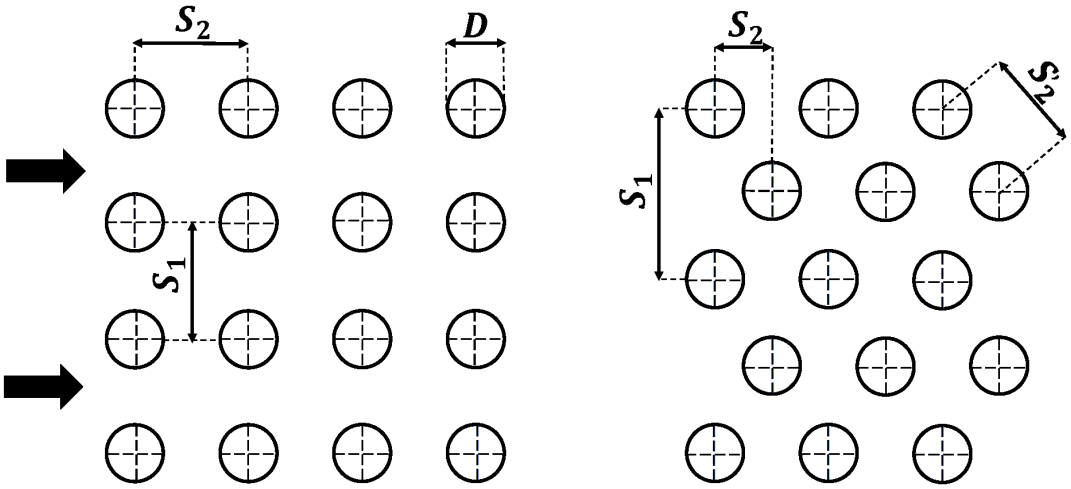

Figure 1.1: In-line and staggered tube arrays

The most common shape for BTHX tubes is cylindrical due to their ease of manufacturing. Other simple shapes, such as oval tubes, have been proposed by Merker et al. [13]. As previously mentioned, additive manufacturing enables the use of more complex shapes to enhance BTHX performance. Kaur et al. [20] also state that additive manufacturing could be used to reproduce the complex tube shapes resulting from a shape optimization process. Bacellar et al. [9] have presented various tube shapes, ranging from round and elliptic to airfoil-shaped tubes, each offering distinct advantages depending on the specific parameters of interest.

The shape optimization of BTHX tubes has been a subject of research in works such as those of Bacellar et al. [9], or by Hilbert et al. [8], both of which use genetic algorithms to perform the optimization. The adjoint-based shape optimization of BTHX tubes has not been extensively studied in the literature. This method has been used in a previous study (Raikar et al. [10]) and has proven capable of providing significant improvements in minimizing the pressure drop of an in-line BTHX.

1.2. RESEARCH OBJECTIVE AND METHODOLOGY

1.2.1. RESEARCH OBJECTIVE

The overall aim of this research is to identify the best practices for minimizing the pressure drop of the air-side of BTHXs through the use of the adjoint-based shape optimization method. In this thesis, flow conditions of interest are those that could possibly be found in condensers and evaporators for aerospace applications, which would correspond to a $Re \approx 1000$ based on the diameter of a round tube.

A secondary objective of this thesis is to examine the best practices for the numerical modelling of in-line BTHX under the flow conditions of $Re \approx 1000$. In this context, steady-state RANS simulations are the primary numerical modelling technique that has been explored.

1.2.2. METHODOLOGY

The optimization framework used in this thesis is similar to that presented by Pai Raikar et al. [10], utilizing the SU2 CFD simulation tool to evaluate pressure drop and heat transfer on the air side of the BTHX. The design surfaces were parameterized using NURBS curves, and the thickness distribution was chosen as the design variables. The gradient of the objective function, determined through the adjoint method, was computed with respect to these design variables.

For the given Reynolds number, it is important to first assess whether the turbulence models available in SU2 are suitable for simulating the air-side flow. To achieve this, simulations using the turbulence models in SU2 were benchmarked against different models from ANSYS Fluent and the available empirical correlation for in-line BTHXs. The primary parameters of interest for this comparison were the friction factor and the Nusselt number. If the turbulence models from ANSYS-Fluent provide more accurate results than those available in SU2, a subsequent assessment of the optimal solution obtained with SU2 with the more accurate model is necessary. Thus, the primary challenge in optimizing the BTHX tubes is accurately modelling the flow within the tube bank.

Other aspects of the optimization process must also be addressed. It is important to determine which optimization algorithm yields the best results in reducing pressure drop while maintaining the heat transfer rate. Finally, assessing the effect of the initial tube shape on the optimization process's output and efficiency is crucial. This investigation was performed by applying the optimization framework to elliptical tube arrays using equivalent inflow conditions as for the round tube arrays.

This thesis focuses exclusively on optimizing the geometry of the air side of the BTHX. The working fluid inside the tubes is modelled by imposing an isothermal condition on the tube walls.

1.3. REPORT OUTLINE

This report documents the numerical work carried out on the numerical modelling and optimization of in-line BTHX. Chapter 2 documents the challenges in the numerical modelling of in-line BTHX for flow conditions of $Re \approx 1000$. This chapter provides a review of the available literature on the experimental and numerical work carried out on BTHX. Chapter 2 also presents the results of a numerical study targeting the modeling of an in-line BTHX with round tubes using various turbulence models. The objective here is to identify which model performs better in predicting the performance of the given BTHX. Chapter 3 presents the optimization framework based on the adjoint method. This framework is applied to optimize the geometry of a 7-round tube inline BTHX, and the results obtained using two different optimization algorithms are compared. Chapter 4 applies the simulation and design methods described in the previous two chapters to target the design of tube bundles adopting non-cylindrical tubes, specifically elliptical tube banks. Finally, Chapter 5 summarizes the findings of this study and offers recommendations for future work on adjoint-based shape optimization of in-line BTHX tubes.

2

Numerical Modelling of Air-Side Flows for In-Line Tube Banks

This chapter provides guidelines for the numerical modelling of the airflows through an in-line bare tube HX. This chapter covers the simulations performed with a steady state RANS solver using three turbulence models (SA, SST and Realizable $k-\epsilon$)

Section 2.1 covers the existing literature on experimental and numerical studies for air flows through BTHXs. Section 2.2 discusses the governing equations for an incompressible flow and the equations used to model the properties of the working fluid. Sections 2.3 and 2.4 discuss the numerical aspects of the solver and review the turbulence models available in SU2 and ANSYS-Fluent.

Using this theoretical background, a case study for an in-line 7-tube BTHX with an air-side flow of $Re_D \approx 1000$ is defined in Section 2.5. In this Section, a grid convergence study was carried out to determine the optimal mesh density. The accuracy of the three turbulence models was also assessed in this Section. Section 2.6 examines the influence of boundary conditions on the accuracy of the result for the three turbulence models. The accuracy of these models was also tested at the flow condition corresponding to $Re_D \approx 200$ by replicating the results of an experimental study by Kasagi et al. [7]. The results of this validation test are discussed in Section 2.7. Finally, Section 2.8 discusses the best practices derived from the theoretical background and CFD simulations carried out in Chapter 3.

2.1. Background

2.1.1. Experimental Studies

The results of the numerical models implemented in this thesis were validated and verified by comparison with experimental data (Section 2.7) and with models derived from empirical correlations (Section 2.5). Both the experimental data and the empirical correlations (HeXacode) were derived from the available literature on experimental studies on the flow through BTHX. The analytical model is based on the empirical correlations for heat transfer and pressure drop available for BTHX as a function of the layout and the flow conditions inside the tube bank. In literature, the heat transfer and pressure drop correlations are generally expressed in a dimensionless form. For the heat transfer coefficient, the correlations are expressed in terms of Nusselt number, namely:

$$Nu = f\left(Re, Pr, \rho, \mu, cp, P_T, P_L\right) \tag{2.1}$$

while dimensionless form for the friction factor, ξ, reads as:

$$\xi = f\left(Re, P_L, P_T, n_R\right). \tag{2.2}$$

These dimensionless numbers are a function of the number of tubes, flow conditions, fluid properties and relative pitches.

The numerical analyses conducted in this thesis were verified against the predictions of the Python tool HeXacode, which is based on the empirical correlations reported for tube banks in the VDI Atlas. This tool was previously used in the works of Krempus et al. [18] to size an evaporator (a multi-pass BTHX) for an ORC

waste heat recovery system. HeXacode is used to size HXs based on the required heat transfer area for a given set of inlet conditions and provides as output the final HX dimensions, mass and pressure drop.

Owing to their prevalent use in industrial applications, tube banks have been the subject of numerous experimental studies. Brevoort et al. [21], in their 1942 study, conducted one of the earliest investigations of the fluid flow inside a staggered cylindrical tube bank. The aim of this study was to visualize the flow patterns and to record the pressure (both static and dynamic) across tube banks. The purpose of these measurements was to understand the phenomena occurring inside a BTHX and to determine their effects on the pressure drop and heat transfer in the tube bank. As noted by Blackall et al. [2], the literature on experimental studies of staggered tube banks is more extensive than that for the in-line configurations. The former has significant advantages over the latter BTHX configuration, with staggered tube banks being more compact and having better performance in terms of heat transfer. The main advantage of in-line BTHX configurations is the tendency to lower pressure drops. Further details on the correlations for pressure drop and heat transfer for staggered arrays can be found in the VDI Heat Transfer Atlas [22].

For the in-line tube banks, the most comprehensive experimental studies were carried out by Zukauskas et al. [1] and by Achenbach in [23] and [24]. Zukauskas derived accurate correlations for both heat transfer and pressure drop over a wide range of Reynolds numbers for square arrays ($P_L = P_T$) of round tubes of various pitch ratios. Figure 2.1 shows the friction factor derived for pitch ratios of 1.25, 2, 2.5 and 3 at various flow conditions, from a Reynolds number of 1 to $2 \cdot 10^6$. This empirical correlation for friction factor can be used to compute the pressure drop according to:

$$\Delta p = \left(\frac{\xi}{\chi}\right) \chi \frac{1}{2} \rho U_m^2 n_R \tag{2.3}$$

Where n_R represents the number of tubes in a row. All empirical correlations provided in this experimental study are valid for a tube array of at least 5 tubes in the streamwise direction.

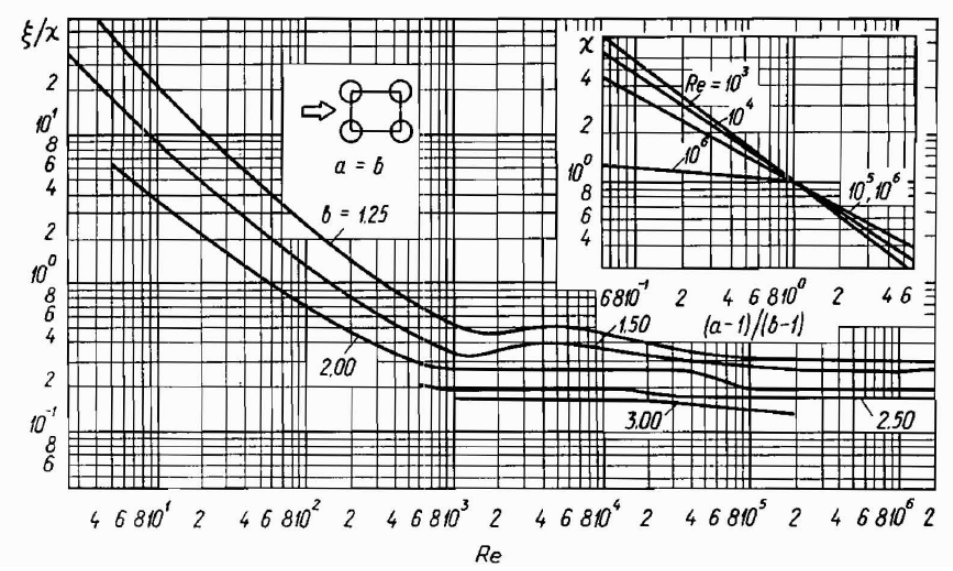

Figure 2.1: Correlations for pressure drop coefficient across in-line tube bundles at different flow regimes, from Zukauskas et al. [1].

Similarly, Zukauskas [17] provides empirical correlations for the average Nusselt number in an in-line tube bank as a function of the Reynolds and Prandtl numbers. For a Reynolds number over 1000, the empirical correlation for a round tube array of $P_L = P_T$ is given in eq. 2.4:

$$Nu = 0.27 Re^{0.63} Pr^{0.36} \left(\frac{Pr}{Pr_w}\right)^{0.25} \tag{2.4}$$

Where Pr_w is the Prandtl number in the near wall region and is computed using the average wall temperature as opposed to the bulk mean temperature used to compute all other thermodynamic properties.

Another aspect discussed by Zukauskas [17] is the type of flow expected through a tube bank depending on the Reynolds number. Zukauskas identifies a region of predominantly laminar flow conditions for $Re <$ 1000 but with the transition to a mixed flow starting to occur near $Re \approx 500$. In the region of $500 < Re < 2 \cdot 10^5$, the flow regime is considered to be mixed, namely the flow exhibits characteristics of both turbulent and laminar flow. This region is also commonly referred to as the subcritical region in the literature and is generally characterized by strong turbulent behaviour in the wakes of the tubes, as noted by West [5]. The next region is the critical region for $Re > 2 \cdot 10^5$, where the flow is predominantly turbulent.

Achenbach [23] provides similar correlations for a higher Reynolds number range that reaches 10^5. Achenbach [23] also provides a detailed analysis of the effects of the roughness of the tube surface on the skin friction factor. However, for the present study, only smooth tubes are considered. Similarly, Traub [25] provides a number of correlations for a range of turbulent flow conditions between $Re = 10^4$ and 10^5. Such studies form the basis for the empirical correlations presented in the VDI Heat Transfer Atlas [22] for the flow inside an in-line tube array. The correlations found in the VDI Atlas for in-line arrays of at least 5 tubes in the streamwise direction are also presented in Annex C.

Another important aspect investigated in the experimental studies is the flow pattern inside the tube bank. Information about the expected flow field is crucial for evaluating whether the numerical models accurately reproduce the flow through a BTHX. Figure 2.2 displays five possible flow patterns for a subcritical flow regime, depending on the combination of longitudinal and transverse pitch of the tube array. This figure provided by Blackall et al. [2] is based on the findings by Ishigai and Nishikawa [26] for different BTHX configurations. As stated in Blackall et al. [2], all these flow patterns presented in Figure 2.2 are valid for subcritical flows. The first region, corresponding to pattern A, corresponds to a bundle configuration where tubes are spaced sufficiently apart to allow vortices to form in the wake of each tube. Each vortex interacts with the tube downstream, leading to the formation of the next vortex in the opposite direction (180^o out of phase). The next flow pattern, namely that indicated with B, exhibits a similar behaviour, but since the longitudinal spacing is smaller, the wakes of each tube are deflected diagonally by the downstream tube. Vortices are still present for pattern B, and each consecutive vortex is out of phase compared to the previous one. Pattern C and the flow regime corresponding to the lower bound of B are particularly relevant for the purposes of this thesis. In this region of $1 < (P_L, P_T) < 2$, the tube array is highly packed, and the compactness of the BTHX is maximized. Here, each tube lies directly in the not-yet-fully-formed wake of the tube upstream. Consequently, vortices in the wake are either absent or less pronounced. This is because the free shear layer of a tube tends to attach directly to the tube downstream. Another important observation is that, in this case, most of the fluid will flow through the bulk jet region in between tube rows. This type of flow pattern is favourable in terms of reducing the pressure drop through the HX. By concentrating the flow through the bulk region and minimizing vortices in the wake, a significant amount of energy dissipation is removed from the flow. This, however, reduces mixing inside the tube bank and thus can have a detrimental effect on heat transfer.

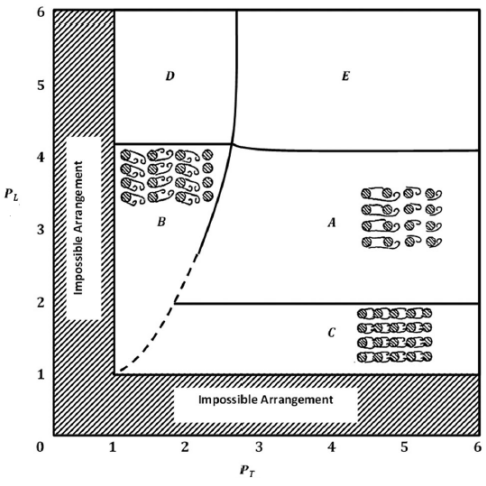

Figure 2.2: Flow patterns typically exhibited by in-line tube banks with variable relative pitches P_T and P_L for a subcritical flow regime, from Blackall et al. [2].

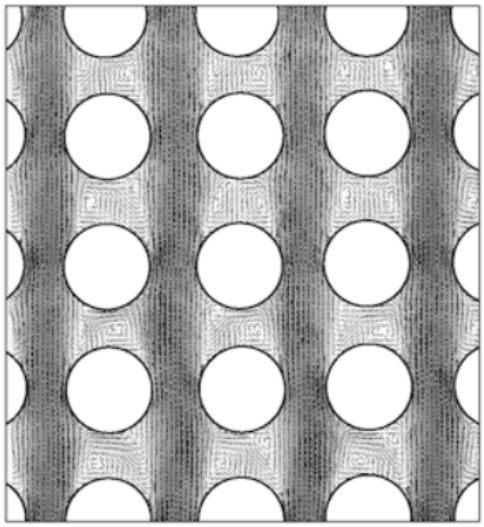

Figure 2.3: Mean velocity vector field obtained for a $P_L = P_T = 1.5$ array at Re=27000 by Iwaki et al. [3].

The relative pitches in Figure 2.2 are based on the tube diameter D, on the longitudinal pitch S_L:

$$P_L = \frac{S_L}{D} \tag{2.5}$$

and on the transverse pitch S_T:

$$P_T = \frac{S_T}{D} \tag{2.6}$$

Figure 2.3 displays the mean velocity vector field obtained for a $P_L = P_T = 1.5$ array at $Re = 27000$ by Iwaki et al. [3]. At this Reynolds number, the flow is still in the subcritical range, meaning that the flow patterns found here and those at $Re \approx 1000$ are similar for the same pitch ratios. This is an example of a packed array whose flow patterns are similar to those of regions B and C from Figure 2.2. This image was obtained through the use of particle image velocimetry (PIV) and provides a clear representation of the kind of flow that should be expected for an array of these dimensions for a subcritical flow regime. The dark arrows represent the bulk area of high velocity, whereas the light arrows denote the wakes of each tube and the region of low velocities. While the wakes are not long enough to see full vortex structures due to the limited spacing between tubes, there is still some amount of vorticity present in the flow. Iwaki et al. [3] identify three types of vortex patterns in the wakes of the tubes: asymmetrical pairs of vortices, symmetrical pairs, or one large vortex. These characteristics of the recirculation region should be considered when assessing the flow field predicted by the numerical models.

Other similar studies that describe the flow fields and flow parameters of in-line tube banks were undertaken by Aiba et al. [27]. This study mainly covered highly packed tube bundles ($P_L = P_T < 1.6$) at $Re = 4.1 \cdot 10^4$ and provides useful data on the velocity profiles between tubes, as well as the streamwise variation of maximum and minimum velocities. Aiba et al. [27] also report useful data about the local Nusselt number and pressure coefficients near each tube. With regards to pressure losses, Aiba et al. [27] show that the first tube has a significantly higher drag coefficient than the subsequent tubes. With regards to heat transfer, Aiba et al. [27] show that the local Nusselt number of the first tube is significantly lower than that of the subsequent tubes. This indicates that the overall heat transfer coefficient of a BTHX is much more dependent on the number of downstream tubes.

2.1.2. NUMERICAL STUDIES

The available literature on numerical analysis of flows through tube banks is primarily focused on the staggered configuration. In-line tube banks have not been studied that extensively, especially with flow conditions of $Re_D = 1000$ where the transition from laminar to subcritical flow occurs (as described by Zukauskas [17]). For this reason, the literature on numerical analysis for both in-line and staggered configurations at different Reynolds numbers was surveyed in order to determine the best modelling practices for tube bundles.

Beale and Spalding [28], [29] were among the first researchers to analyze flows through both in-line and staggered arrays in the ranges of $Re = 10 - 1000$ and $Re = 30 - 3000$, respectively. These studies cover the entire laminar flow region and the transition to subcritical flow, as described by Zukauskas [17]. The flow simulations were conducted on streamwise periodic domains in both studies. The calculations were done by ignoring turbulence since they consider the boundary layer to be laminar in this Re range and employing unsteady time-marching flows. Both studies found discrepancies with experimental data for flows not under the laminar flow regime. Thus, these studies confirm the need to model turbulence in order to accurately predict heat transfer and pressure drop.

Benhamadouche et al. [30] simulated a staggered tube array using three URANS models and one LES model. This study showed that of all types of CFD models, the LES (large eddy simulations) one exhibits the best accuracy in reproducing experimental data. The URANS turbulence model that provided the best match with the experimental data was the Elliptic Blending Reynolds-stress model (EB-RSM). The accuracy of EB-RSM was also contingent on the flow conditions; the model performed well at $Re_D = 10000$, where the results were close to the experimental data, but not at $Re_D = 30000$, where the error was large. The doctoral thesis of West [5] makes similar observations regarding the accuracy of LES and URANS for the simulation of flows through in-line tube banks.

The most comprehensive work carried out on in-line tube bundles is presented by West [5], where multiple computational approaches were assessed against the available experimental data. West [5] carried out a number of flow simulations on an in-line tube array of $P_L = P_T = 1.6$, at $Re = 41000$ using both URANS with multiple turbulence models and LES solvers. Two types of flow domains were investigated, as seen in Figure 2.4. Due to high computational cost, only URANS simulations were carried out on the full domain from

Figure 2.4(a). LES was performed only on a stream-wise periodic domain shown in Figure 2.4(b). While the stream-wise periodic domain is more computationally efficient, it was found that the turbulence levels and the velocity profiles are sensitive to the domain size. In order to capture large flow structures, the streamwise periodic domain has to be sufficiently large. With regards to LES simulations, West [5] mentions that it is necessary to model confining walls in order to accurately predict the pressure and heat transfer around the central tube.

An important aspect discussed by West [5] is the difference in the velocity fields predicted by different models. For example, $k-\omega$ SST was found to slightly overpredict velocities in the free stream region compared to those predicted by the $k-\epsilon$ model and the LES simulations. As shown in Figure 2.9, the $k-\epsilon$ model also was able to predict the expansion and compression in the flow as the air passes through the minimum cross sections between the tubes, while the SST model results featured a continuous increase in velocity throughut the free stream region. SST has also shown a greater tendency to display asymmetrical flow patterns in the wakes of the tubes while this was not the case of the $k-\epsilon$ model. As shown in Figure 2.2, these asymmetrical flow patterns should be expected for pitch ratios of $P_L = P_t = 1.6$.

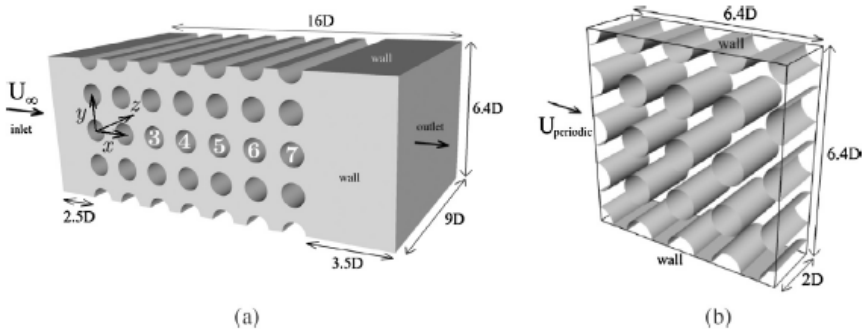

Figure 2.4: Flow domains used by West et al. [4] for the URANS simulations (a) and the LES simulations (b).

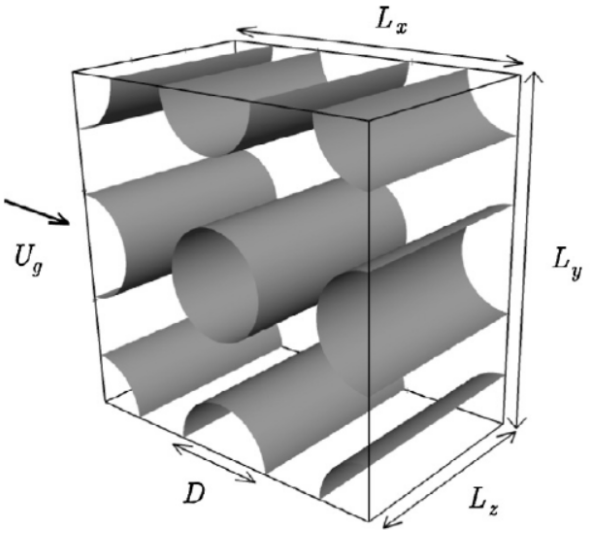

Figure 2.5: Streamwise periodic domains used By West et al. [4] used for both URANS and LES simulations

West [5] also used a smaller streamwise periodic domain to compare the pressure distribution and heat transfer around the central tube predicted by the URANS and LES models. This streamwise periodic domain is composed of 4 tubes arranged on 3 rows and is displayed in Figure 2.5. The results for the flow simulations carried out on this domain are displayed in Figures 2.6 and 2.7 which show the pressure coefficient and the Nusselt number around the central tube of the computational domain. The results obtained for the LES simulations better match the experimental data for both the Nusselt number and pressure coefficient. The best performing URANS models in terms of predicting the pressure coefficient are those adopting the $k-\epsilon$ Linear

Production method among the eddy viscosity models and the SSG for the Reynolds stress models. For the Nusselt number, the SSG model however, displays somewhat worse results than the $k-\epsilon$ Linear Production model. For a domain with confining walls, both models suffer from decreased accuracy in the prediction of heat transfer if an inadequate wall function is used. The difference in accuracy between LES and RANS solvers for flows across tube bundles is also pointed out in an earlier study by Rollet-Miet et al. [31]. This study deals with staggered arrays at a flow regime of Re = 16000 over a wide range of pitches from 1.5 to 4. The RANS simulations carried out in this study also failed to accurately match the LES results, with the latter showing good agreement with the experimental data.

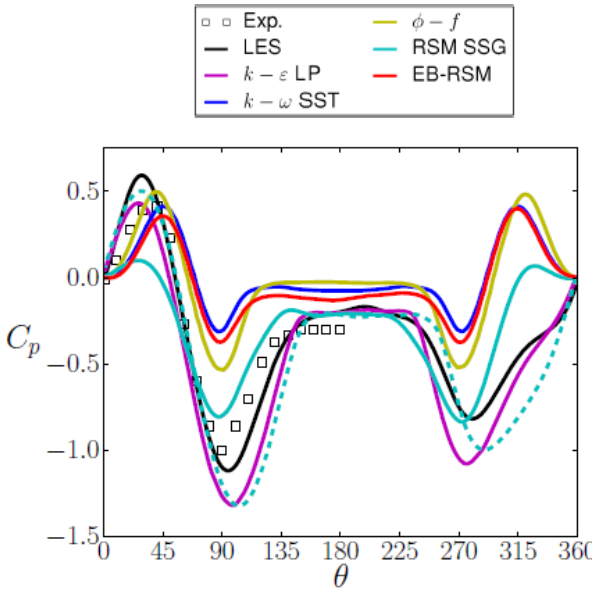

Figure 2.6: Pressure coefficient around a tube obtained for various turbulence models for the streamwise periodic domain (Figure 2.5) presented in the thesis of Alastair West [5].

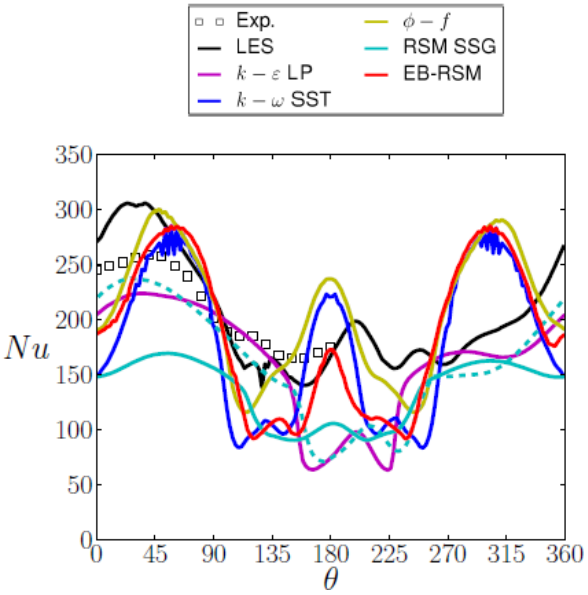

Figure 2.7: Nusselt number around a tube obtained for various turbulence models for the 2x2 streamwise periodic domain (Figure 2.5) presented in the thesis of Alastair West [5].

Another study that confirms the findings of West [5] is the one carried out by Blackall et al. [2], for a $Re \approx 41000$. This study also notes that low-Reynolds turbulence models such as $k-\omega$ predict flow separation from the walls of the tubes too early, whereas high-Reynolds models are better at estimating the location of adverse pressure gradients and thus delaying flow separation. This has a significant effect in estimating the friction factor and, consequently, the pressure drop.

While LES and Reynolds-stress models such as EB-RSM or SSG can provide accurate results, they are computationally expensive, making them impractical to employ in an optimization process. An important aspect to consider is the accuracy of steady-state RANS simulations. While this type of CFD analysis is the least accurate of the various modelling approaches found in the literature, it is the most computationally efficient. This computational cost advantage makes RANS simulations appealing for the implementation of the shape optimization framework. Consequently, it is important to know which steady RANS turbulence model performs best in reproducing the flow characteristics in tube bundles.

Deeb [6] reports accurate numerical results, compared to experimental data, obtained with RANS simulations using the RNG $k-\epsilon$ model. Deeb [6] analyses a packed non-cylindrical tube array on a range of Reynolds numbers between $1.78 \cdot 10^3$ and $18.72 \cdot 10^3$. To validate the model used, the author simulated an array of round tubes over the Re range mentioned previously and the results were compared to the predictions of the empirical correlations developed by Zukauskas [1]. The results show an excellent match with correlation data for both friction factor and Nusselt Number. Figure 2.8 shows the comparison between the results of the CFD and correlation data.

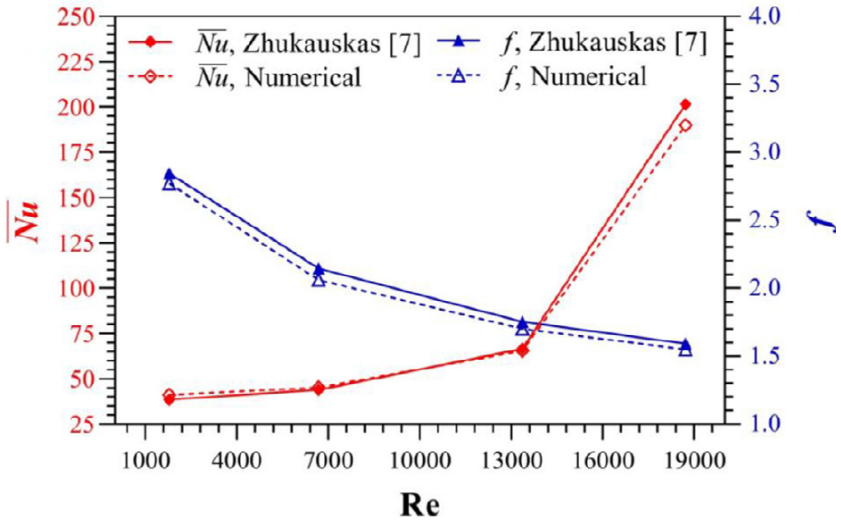

Figure 2.8: Nusselt number and friction factor obtained by Deeb [6] for a cylindrical staggered array using the RNG $k-\epsilon$ model.

Another study that shows similar results obtained with the RNG $k-\epsilon$ model is that carried out by Elmekawy et al. [32]. This study compares the performance of finned tube heat exchangers (FTHX) to that of BTHX, both with staggered circular tubes. The validation of the model is carried out using the BTHX array, and the performance is compared to the experimental and CFD data provided by Mangrulkar et al. [33].

Overall, the literature provides some good insight into the modelling of turbulent flows through BTHX. Although no single study addresses the modelling of turbulent flows in the range of $Re = 1000$ for cylindrical in-line tube arrays, the literature does point towards some useful directions. As illustrated by Deeb [6], for steady-state RANS simulations with eddy viscosity models, it would be preferable to use one of the $k-\epsilon$ models to obtain high-fidelity results. Blackall et al. [2] point out that the separation and reattachment of the flow on the tube walls are better predicted by $k-\epsilon$ than $k-\omega$ models. On the other hand, West [5] showed that low Reynolds models such as $k-\omega$ SST are better at reproducing the expected asymmetrical flow patterns in the wake of the tubes. Based on these insights, the following sections present the steady state RANS model implemented in this work to simulate an airflow through an in-line BTHX.

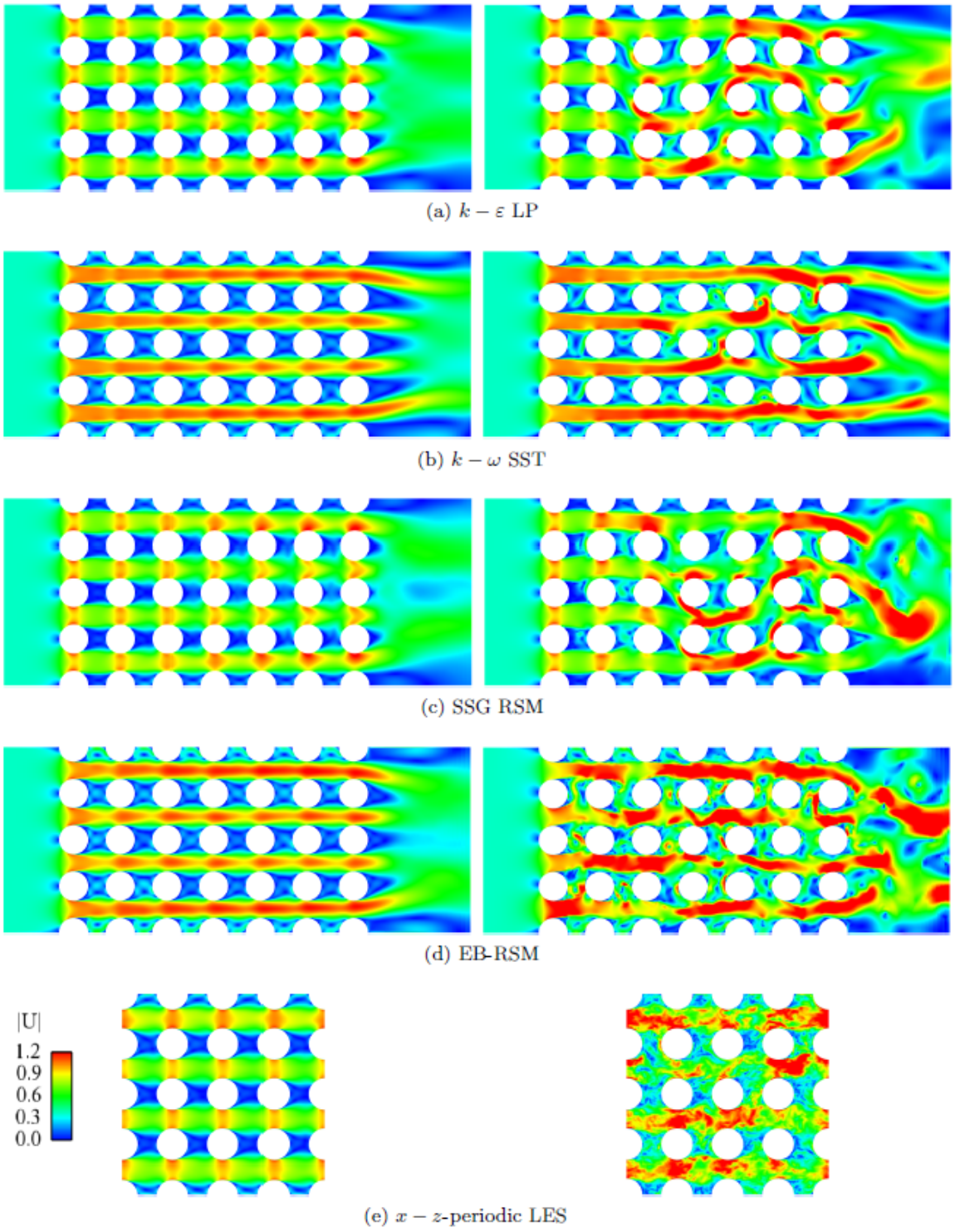

Figure 2.9: Time-averaged (left) and instantaneous (right) velocity contours obtained by West [5].

2.2. FLOW PROBLEM

2.2.1. GOVERNING EQUATIONS

The flow problem that has to be modelled is the airflow through an in-line BTHX. A generic representation of the flow domain is presented in Figure 2.10, where the airflow direction is perpendicular to the transverse pitch of the tube array. Since the flow velocity is considered uniform in the lengthwise direction, the flow can be modelled as purely 2D.

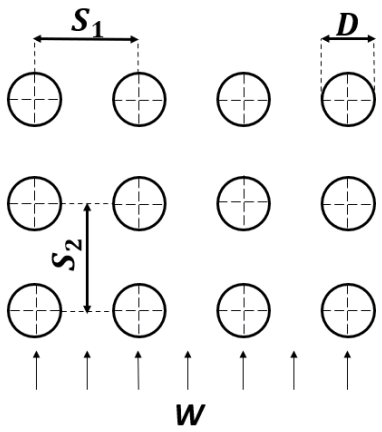

Figure 2.10: In-line tube bundle

Before implementing the numerical model, a few simplifying assumptions will be made. First, the flow is considered incompressible since the maximum Mach number does not exceed 0.045 for any of the simulations presented in the following chapters. Compressibility effects for flows of $M << 0.3$ can be ignored. Second, the effects of external forces (gravity and buoyancy) will also be neglected. Third, while the flow is assumed to be steady-state, the flow solvers will use a time-marching approach to solve the Navier-Stokes equations. Therefore, the equations will be written in their time-dependent formulation. Lastly, for the conservation of energy, only convection and conduction will be modelled, and thus, the effects of thermal radiation will be ignored.

With the assumptions outlined above, the conservation of mass, momentum and energy can be written for a 2D incompressible flow. Equation 2.7 is the continuity equation (divergence of velocity), equation 2.8a represents the conservation of momentum and equation 2.9 is the conservation of energy.

$$\frac{\partial u_i}{\partial x_i} = 0 \tag{2.7}$$

$$\frac{\partial u_i}{\partial t} + u_j \frac{\partial u_i}{\partial x_j} + \frac{1}{\rho}\frac{\partial p}{\partial x_i} - \frac{\partial}{\partial x_j}\left(\nu \frac{\partial u_i}{\partial x_j}\right) = 0 \tag{2.8a}$$

$$\frac{\partial T}{\partial t} + u_j \frac{\partial T}{\partial x_j} - \frac{\partial}{\partial x_j}\left(\alpha_c \frac{\partial T}{\partial x_j}\right) = 0 \tag{2.9}$$

2.2.2. FLUID PROPERTIES

The working fluid in this case is air. First, equation 2.8a makes use of the density, ρ and the kinematic viscosity, ν. The density can be defined as a function of pressure and temperature using the equation of state:

$$\rho = \frac{p}{RT} \tag{2.10}$$

The kinematic viscosity is a function of density and dynamic viscosity:

$$\nu = \frac{\mu}{\rho} \tag{2.11}$$

The dynamic viscosity can be defined as a function of temperature through Sutherland's formula, as outlined in [34]. For Sutherland's formula, a reference viscosity and temperature have to be defined, in this case: $\mu_0 = 1.716 \cdot 10^{-5} Pa \cdot s$ and $T_0 = 273.15K$. The Sutherland constant S_μ is $110.4K$. This results in the dynamic viscosity being defined as:

$$\mu = \mu_0 \left(\frac{T}{T_0} \right)^{\frac{3}{2}} \left(\frac{T + S_\mu}{T_0 + S_\mu} \right) \tag{2.12}$$

For the thermal properties, only the thermal diffusivity, α_c, has to be defined. This quantity can be calculated as

$$\alpha_c = \frac{k_c}{\rho c_p} \tag{2.13}$$

The thermal diffusivity is a function of density, thermal conductivity k_c, and specific heat c_p. The latter two quantities are considered to be constant and will be assigned the average values of $k = 0.026 \frac{W}{m \cdot K}$ and $c_p = 1006.9 \frac{J}{kg \cdot K}$. These two quantities exhibit only a slight variation over the simulated temperature range and, therefore, this simplification does not significantly impact the final results (pressure drop and heat transfer coefficient).

2.3. NUMERICAL MODELLING

The partial differential equations presented above were solved numerically using the Finite Volume Method (FVM). The values of the conserved quantities along the edges/boundaries are obtained through interpolation from the quantities estimated at center of the control volumes. The fluxes going through the boundary edges of the FVs are consequently evaluated as line integrals instead of surface integrals in 3D. The integrals on the boundaries of the control volume are also approximated by a sum of discrete values at one or multiple points along the boundary. The type of interpolation scheme used defines the order and type of the numerical method and the spatial discretization scheme. The discretization schemes used in each software (SU2/ANSYS-Fluent) are presented separately in the sections 2.3.1 and 2.3.2.

2.3.1. SU2

SU2 is an open-source tool developed to analyse multiphysics problems and solve optimization tasks on an unstructured grid. This software, based on a C++ object-oriented architecture, was mainly developed to solve RANS simulations for turbulent flows. SU2 is also capable of performing sensitivity analysis and adjoint-based optimizations by itself or in conjunction with other software packages (such as ParaBlade). For the purposes of this thesis, this software package will be used in the shape optimization process presented in the following chapters. The history and architecture of the SU2 software package have been extensively documented by Economon et al. [35] and Palacios et al. [36].

For the modelling of turbulence in the RANS solver, there are 2 available options in SU2: Spalart-Allmaras and SST. Both models have been extensively verified against experimental data for both subsonic and supersonic flows, as shown by Palacios et al. [36].

SECOND ORDER UPWIND SCHEME

The discretization scheme used in SU2 for all the following simulations is the second-order accurate MUSCL (Monotone Upstream-Centered Scheme for Conservation Laws) upwind scheme. The term Upwind indicates that the values of the quantities at the cell faces/edges, ϕ_e, are derived from the quantities in the cell centre ϕ upstream. The upstream direction is given by the direction of the normal velocity on the respective face/edge.

The second-order accuracy for the quantities on a cell's edge is achieved by using a Taylor series expansion from the cell-centered quantity. The quantity ϕ_e at the cell's edge is, therefore, a function of the quantity at the cell centre ϕ and its gradient, as shown in the following equation:

$$\phi_{e,SU} = \phi + \nabla\phi \cdot \vec{r} \tag{2.14}$$

The gradient $\nabla\phi$ is calculated according to the Green-Gauss method, and the vector $\vec{r}$ is the normal vector from the cell centroid upstream of the corresponding edge.

2.3.2. ANSYS-FLUENT

ANSYS-Fluent is commercial CFD software known for its accuracy in modelling complex physical phenomena such as fluid flow or heat transfer. This ANSYS package is one of the most commonly used fluid simulation tools in industry. It is well-equipped to simulate a wide range of flow regimes, from laminar to fully turbulent. Fluent copes well with both structured and unstructured meshes and has been widely validated with experimental data. The solver is described in the ANSYS-Fluent Theory guide [37].

Fluent offers a wide range of turbulence models that can be implemented in conjunction with the RANS equations. In addition to the eddy viscosity models such as $k-\epsilon$ and $k-\omega$, Fluent also offers Reynolds-Stress Models as an alternative. For the purposes of this thesis, only the $k-\epsilon$ models (standard, RNG and Realizable) are presented and used in the following simulations. In particular, the Realizable $k-\epsilon$ was shown to produce fairly accurate results for the simulation of airflows through BTHX.

THIRD-ORDER MUSCL SCHEME

The discretization scheme used in ANSYS-Fluent is a third-order accurate MUSCL scheme, which is derived by combining a central difference and an upwind scheme to compute the quantities at the cell's faces. Thus, the quantities at the cell boundary for this scheme are computed as a function of the quantities obtained through the central difference scheme $\phi_{e,CD}$, the quantities obtained through the upwind scheme $\phi_{e,SU}$ (computed using equation 2.14) and the value of θ is chosen to maintain the solution's monotonicity and prevent numerical oscillations.

$$\phi_{e,MUSCL} = \theta\phi_{e,CD} + (1-\theta)\,\phi_{e,SU} \tag{2.15}$$

The central difference term of equation 2.15 is given in equation 2.16 where the indices u and d represent the cells upstream and downstream of the respective edge.

$$\phi_{e,CD} = \frac{1}{2}\left(\phi_u + \phi_d\right) + \frac{1}{2}\left(\nabla\phi_u \cdot \vec{r}_u + \nabla\phi_d \cdot \vec{r}_d\right) \tag{2.16}$$

Unlike other third-order discretization schemes available in Fluent, such as QUICK, the MUSCL scheme is suitable for use with unstructured meshes. The results obtained in ANSYS-Fluent with both the MUSCL scheme and the second-order upwind scheme were within less than 1% of each other. The former discretization scheme was employed as it provides slightly better results when compared to the empirical correlation data.

2.3.3. PSEUDO TIME-STEPPING

As mentioned previously, the flow simulations are carried out as steady-state RANS simulations. However, both ANSYS-Fluent and SU2 make use of a time-marching approach to solve the flow problem. In this method, the steady-state equations are solved using a time-marching approach, where the solution is advanced in pseudo-time steps until it converges to a steady state. This technique can help stabilize the solution process and accelerate convergence, especially in cases with complex flow features. Instead of fixing the time step, a CFL number is prescribed. The local time step Δt is calculated from the CFL:

$$CFL = \frac{U\Delta t}{\Delta x} \tag{2.17}$$

where u is the local velocity and Δx is the grid spacing.

2.4. TURBULENCE MODELLING

The $Re \approx 1000$ of the flow problems in this thesis places them in a transition regime where the flow is no longer laminar but not yet fully turbulent. The flow at $Re \approx 1000$ is in the subcritical region described by Zukauskas [17]. For BTHX, the Reynolds number is based on the diameter or on the chord of the tube, and is computed as:

$$Re_D = \frac{U_m D}{\nu} \tag{2.18}$$

Here, U_m represents the velocity at the minimum cross-section, which for an in-line arrangement is just a function of the transverse pitch, as shown in equation 2.19.

$$U_m = \frac{U_\infty S_T}{D} \tag{2.19}$$

Turbulent flows are characterized by a fluctuating velocity field which has the effect of inducing fluctuations in the transported quantities as well. There are multiple ways of solving these fluctuating quantities through the use of RANS, LES and DNS. The latter two methods are too computationally intensive. LES tries to explicitly solve the large and energetic scales of the turbulent problem while modelling the smaller and more computationally intensive scales. DNS seeks to directly solve the Navier-Stokes equations without applying a scale filter or modelling turbulence. Another disadvantage of these methods is that they are implicitly time-variant and, therefore, would be computationally expensive to utilize in an optimization framework.

The Reynolds-averaged Navier-Stokes approach reduces the computational cost by averaging the turbulent quantities and modelling turbulent scales rather than solving them directly. RANS methods decompose the velocity terms of the Navier-Stokes equations into a mean and fluctuating quantity, as can be seen in equation 2.20:

$$U = \overline{U} + U' \tag{2.20}$$

where $\overline{U}$ is the mean velocity and U' is the fluctuation.

The velocity in equation 2.8a was substituted with the mean and fluctuating velocities $\overline{U}$ and U'. The momentum equation was therefore rewritten as equation 2.21. The right-hand side term represents the effect of turbulence and is known as the Reynolds stress tensor, see eq. 2.22. To close the RANS equations, this turbulent term needs to be modelled. Other than this term, all the conservation equations have the same form of the original Navier-Stokes equations, but the variables are substituted with average quantities.

$$\frac{\partial \overline{U}}{\partial t} + \nabla \cdot \left(\overline{UU}\right) + \frac{\nabla \overline{p}}{\rho} - \frac{\mu}{\rho} \nabla \cdot \nabla \overline{U} = -\nabla \cdot \overline{U'U'} \tag{2.21}$$

$$\tau_{ij} = -\overline{U_i' U_j'} \tag{2.22}$$

The term presented in equation 2.22, the Reynolds stress tensor, was modelled using the Boussinesq method, which relates the stress tensor to the mean velocity gradient. This method is more computationally efficient than the Reynolds Stress Transport model, which solves an additional transport equation for each individual term of the Reynolds stress tensor. In the Boussinesq approach, only one equation has to be solved in the SA model for the eddy viscosity. Eddy viscosity (ν_t) refers to the effective viscosity that accounts for the momentum transfer due to turbulence. It represents the enhanced diffusion of momentum in turbulent flows, similar to viscosity in laminar flows, but it is not a physical property of the fluid. Instead, it is modelled based on the characteristics of the turbulence and varies depending on the turbulence model used.

In the $k-\epsilon$ and $k-\omega$ models, two equations have to be solved for kinetic energy and for turbulent dissipation rate or specific dissipation rate, respectively. Turbulent kinetic energy (k) represents the energy per unit mass contained in the turbulent fluctuations of the flow, while the turbulent dissipation rate (ϵ) measures the rate at which this energy is converted into heat due to viscous effects. The specific dissipation rate (ω) is a normalized form of dissipation rate, providing an indication of the rate at which turbulence decays per unit of turbulent kinetic energy.

The Boussinesq approach for modelling the stress tensor is given in equation 2.23:

$$-\overline{U_i' U_j'} = 2\nu_t S_{ij} - \frac{2}{3}\delta_{ij} k \tag{2.23}$$

where ν_t is the eddy viscosity and k is the turbulent kinetic energy. The terms of this equation are explained in Annexe A.1.

2.4.1. SPALART-ALLMARAS

The Spalart-Allmaras (SA) model developed by Spalart et al. [38] is based on a simple transport equation that solves for a kinematic eddy viscosity. This model is quite popular in aerospace as it has been proven to work quite well for flows subjected to adverse pressure gradients. The main advantage of this model is its relative simplicity, and is especially suited to low Reynolds flows. The SA model can also be used together with a wall function near wall regions where grid refinement is insufficient. The main drawback of this model is its inability to cope well with flows of changing length scales, such as when a wall-bounded flow changes to a free shear flow, as stated by Spalart et al. [38].

The transport equation of the SA model solves for the variable $\tilde{\nu}$, which is a function of the eddy viscosity. This variable can be used to compute the turbulent eddy viscosity using equation 2.24. The transport variable $\tilde{\nu}$ can be determined by computing equation 2.25. The terms and constants used in equation 2.25 are defined in Annexe A.2. The important parameter that is used to assess the mixing occurring inside the flow is the eddy viscosity instead of the turbulent kinetic energy.

$$\nu_t = \tilde{\nu} f_{v1} \tag{2.24}$$

$$\frac{\partial \tilde{\nu}}{\partial t} + U_i \frac{\partial \tilde{\nu}}{\partial x_j} = C_{b1}\left(1 - f_{t2}\right)\tilde{S}\tilde{\nu} - \left[C_{w1} f_w - \frac{C_{b1}}{\kappa^2} f_{t2}\right]\left(\frac{\tilde{\nu}}{d}\right)^2 + \frac{1}{\sigma}\left[\frac{\partial}{\partial x_j}\left((\nu + \tilde{\nu})\frac{\partial \tilde{\nu}}{\partial x_j}\right) + C_{b2}\frac{\partial \tilde{\nu}}{\partial x_j}\frac{\partial \tilde{\nu}}{\partial x_j}\right] \tag{2.25}$$

Even though the model is quite robust, computationally efficient and performs well for attached flows, it struggles to predict flow reattachment. This could make SA unsuitable for the flow problem at hand, as flow separation and reattachment are likely to occur between consecutive tubes.

2.4.2. K-ϵ

The $k-\epsilon$, developed by Launder and Jones [39], is a semi-empirical model that solves two separate transport equations for turbulent kinetic energy (k) and turbulent dissipation rate (ϵ). This model offers a low computational cost compared to LES and RSM models while also providing reasonably accurate results. This type of model is especially good for external flows or for flows where modelling the free-stream region is important. According to Launder and Jones [39], the standard $k-\epsilon$ model is, however, unsuitable for flows where there are strong pressure gradients or where flow separation may occur. The model also assumes a fully turbulent flow, ignoring the effects of laminar viscosity present in the near-wall region. The two transport equations that characterize the model are given in eq. 2.26, for k and eq. 2.27 for ϵ, as presented by Chien [40].

$$\frac{\partial \rho k}{\partial t} + \frac{\partial \rho k U_i}{\partial x_i} = P - \rho\epsilon + \frac{\partial}{\partial x_j}\left[\left(\mu + \frac{\mu_t}{\sigma_k}\right)\frac{\partial k}{\partial x_j}\right] + \rho L_k \tag{2.26}$$

$$\frac{\partial \rho \epsilon}{\partial t} + \frac{\partial \rho \epsilon U_j}{x_j} = C_{\epsilon 1} f_1 \frac{\epsilon}{k} P - C_{\epsilon 2} f_2 \frac{\rho \epsilon^2}{k} + \frac{\partial}{\partial x_j}\left[\left(\mu + \frac{\mu_t}{\sigma_\epsilon}\right)\frac{\partial \epsilon}{\partial x_j}\right] + \rho L_\epsilon \tag{2.27}$$

Once these 2 equations have been solved, the two transport quantities can be used to compute the turbulent eddy viscosity in the following equation:

$$\mu_t = C_\mu \frac{\rho k^2}{\epsilon} \tag{2.28}$$

The constants used in equations 2.26, 2.27, and 2.28 are presented in Annexe A.3.1.

2.4.3. K-ϵ RNG

The $k-\epsilon$ RNG is a model derived from the instantaneous Navier-Stokes equations using the renormalization group theory described by S.A. Orszag et al. [41] and is an improvement of the standard model. The RNG model has improved accuracy for swirling flow and rapidly strained flows. Another important difference between the RNG and standard $k-\epsilon$ is that the former accounts for low Reynolds effects through the use of a different formulation for the effective viscosity. In this context total viscosity refers to the total viscosity that includes for both turbulent and near-wall effects. This feature of the RNG model allows it to provide better results for low Reynolds flows if the near-wall region is modelled properly.

The RNG model uses two transport equations similar to 2.26 and 2.27 for turbulent kinetic energy and dissipation rate with some added terms and different constants. The equations for this model are described in Annexe A.3.2 as described in the ANSYS-Fluent Theory Guide [37].

The RNG model features an additional term in the dissipation rate equation and the turbulent viscosity definition is modified to take into account the effects of swirl. The turbulent viscosity in RNG μ_t is a modification of the μ_{t0}, the viscosity without swirl effects, calculated according to equation 2.28. The viscosity with the swirl effects μ_t takes the form of a functional and can be written as follows:

$$\mu_t = \mu_{t0} f\left(\alpha_s, \Omega, \frac{k}{\epsilon}\right) \tag{2.29}$$

Here the constant Ω, the characteristic swirl, is computed by ANSYS-Fluent. The constant α_s is 0.07 for flows with mild swirl but this value can be modified by the user if necessary.

2.4.4. REALIZABLE K-ϵ

The Realizable k-ϵ model uses a different formulation for turbulent viscosity and also a different equation for the dissipation rate. The latter equation is derived from an equation for the transport of the vorticity fluctuation. This model is more complete in terms of satisfying the constraints of the Reynolds stress tensor than the two previously presented models. The Realizable model provides better results for boundary layer flows with strong pressure gradients, separation, and recirculation, making this model likely better at simulating flows through BTHX. Both the RNG and Realizable models have shown improvements over the standard $k-\epsilon$ model for modelling flows that feature vortices, rotation or strong streamline curvature. However, the Realizable model has also shown a tendency to outperform RNG in separated flows. The modification to the dissipation rate equation is presented in Annexe A.3.3, while the equation for turbulent kinetic energy remains unchanged, see eq. 2.26.

The different formulation of the turbulent intensity comes from a modification of the constant C_μ in equation 2.28. In the Realizable model, C_μ is no longer constant and is instead computed according to the following equation:

$$C_\mu = \frac{1}{A_0 + A_s k U^* / \epsilon} \tag{2.30}$$

The terms of this equation are described in A3.3. C_μ, in this case, is a function of the mean strain rate, the angular velocity of rotation, the rotation rate and the model's transport properties (k and ϵ).

2.4.5. K-ω SST

The SST (shear-stress transport) model combines the advantages of the standard $k-\omega$ in the near-wall region and $k-\epsilon$ in the far-field region. The two models are combined using a blending function, which is one in the near-wall region and zero in the free-stream region. Theoretically, this model should provide good results in flows with adverse pressure gradients and with separation. The ability of SST to directly model the boundary layer means that this model is suitable for low Reynolds flows without the use of wall functions.

$k-\omega$ is an empirically based, two-equation model that solves for two transport properties: turbulent kinetic energy (k) and the specific dissipation rate (ω). This model includes modifications for low Reynolds number flows and shear flow spreading. $k-\omega$ is generally well suited to the modelling of wall-bounded flows.

The two transport quantities k and ω are calculated by the following equations:

$$\frac{\partial k}{\partial t} + U_j \frac{\partial k}{\partial x_j} = P_k - \beta^* k\omega + \frac{\partial}{\partial x_j}\left[(\nu + \sigma_k \nu_t)\frac{\partial k}{\partial x_j}\right] \tag{2.31}$$

for the turbulent kinetic energy, and:

$$\frac{\partial \omega}{\partial t} + U_j \frac{\partial \omega}{\partial x_j} = \alpha S^2 - \beta \omega^2 + \frac{\partial}{\partial x_j}\left[(\nu + \sigma_\omega \nu_t)\frac{\partial k}{\partial x_j}\right] + 2(1-F_1)\sigma_{\omega 2}\frac{1}{\omega}\frac{\partial k}{\partial x_i}\frac{\partial \omega}{\partial x_i} \tag{2.32}$$

for the specific dissipation rate. The various terms and constants are presented in Annexe A.4. These equations are first presented in the work of Menter [42].

With respect to the standard k-ω model, the SST model also uses a different definition of the turbulent viscosity as shown in equation 2.33:

$$\nu_t = \frac{a_1 k}{max[a_1\omega, SF_2]} \tag{2.33}$$

2.5. CASE STUDY

2.5.1. FLOW DOMAIN

The case study chosen to assess the various turbulence models considers an in-line 7 row BTHX made up of cylindrical tubes. The considered airflow of Reynolds number range is between $Re \in [1074.34; 1184.38]$. The longitudinal and transverse pitch ratios are 2, i.e. $P_L = P_T = 2$. A similar flow domain layout is used in the next chapters for the assessment of the shape optimization methodology. The goal of this simulation study is to determine the most suitable grid density to be used in the optimization process and to compare the accuracy of the results obtained with different turbulence models.

A detailed representation of the domain geometry is given in Figure 2.11. This BHTX layout was chosen for a few reasons mainly having to do with computational efficiency and the availability of empirical correlations.

More in detail, the number of tubes was chosen in order to minimize the size of the flow domain. At the same time, according to Zukauskas [1], the minimum size of the tube bundle for which the correlations are still valid is with five tubes in the longitudinal and transverse directions. Moreover, only one tube row was simulated to reduce the computational cost, and the upper and lower boundaries were modelled as either symmetric or periodic boundaries.

The inlet and outlet boundaries were placed far from the first and last tubes. The outlet one is situated at a distance of 70 diameters from the centre of the last tube, while the inlet is situated 10 diameters away from the first tube centre. The choice of the inlet and outlet positions was inspired by the simulations carried out by Kasagi et al.[43], where the distances are equal to 10 and 40 diameters in length from the first and the last tube, respectively. The distance to the inlet is less important as the flow is laminar until the first tube is reached, and thus, the distance has been kept the same. However, the outlet distance could be more important as it is desirable for the flow to be fully uniform again when the outlet is reached. Kasagi et al.[43] carried out simulations in the laminar regime, while the present simulations will be carried out within the subcritical flow regime. Therefore, the distance to the outlet has been increased to minimize the effects of the boundary on the overall results.

As stated previously, only the air-side flow is modelled in the present work. The flow inside of the BTHX tubes is taken into account by imposing a constant temperature on the walls. This is equivalent to assuming that an uniform condensation process occurs inside the tubes.

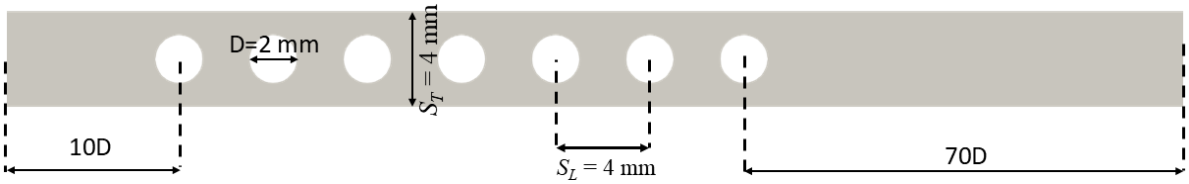

Figure 2.11: In-line 7 tube row geometry.

2.5.2. BOUNDARY CONDITIONS

The boundary conditions of the flow domain are displayed in Figure 2.12. The boundary condition prescribed at the inlet is the velocity, along with the other relevant quantities: temperature and turbulence parameters. At the outlet, a gauge pressure is applied. It is possible to use a gauge pressure as opposed to an absolute value because the flow is considered incompressible in this case. The tubes are modelled as smooth, isothermal, no-slip walls. The transverse boundaries (top and bottom of the domain) are initially modelled as symmetric boundaries. A discussion on the choice of boundary condition on the top and bottom sections of the domain can be found in Section 2.6.

Figure 2.12: Boundary conditions of the flow domain for the in-Line 7-tube row.

- Inlet velocity: 3.986 m/s
- Inlet Temperature: 273.15 K
- Inlet Turbulence intensity: 5%
- Inlet Turbulence length scale: 0.0004 m
- Wall Temperature: 374.19 K
- Outlet Pressure: 0 Pa
- Absolute Pressure: 100000 Pa

The actual boundary conditions and other parameters for the CFD model are given above. The density is computed across the flow field using equation 2.10. The quantities of interest resulting from the simulations are the outlet temperature and the inlet pressure. These two quantities are necessary in order to compute the average Nusselt number and the friction factor, respectively.

The turbulence parameters at the inlet are necessary to initialize the turbulent kinetic energy and the dissipation rate fields for the two-equation models. The turbulent length scale was chosen as 10% of the inlet length, while as an initial condition for the turbulence intensity a medium turbulence level of 5% is assumed. These two parameters are related to the two transport quantities through equations 2.34 and 2.35 where I and l are the turbulence intensity and length scale, respectively.

$$k = \frac{3}{2}(UI)^2 \tag{2.34}$$

$$\epsilon = C_\mu^{\frac{3}{2}} k^{\frac{3}{2}} l^{-1} \tag{2.35}$$

2.5.3. MESHING

The meshing was carried out using the ANSYS Meshing tool, which allows for the generation of 2D meshes. The 2D mesh was subsequently exported and converted into an SU2-compatible format as well. The mesh constructed in this case is made up of two regions. The largest region is the unstructured far-field made up of triangular elements, while the smaller region around the tube walls is a boundary layer made up of quadrilateral elements. This meshing method is easy to implement and allows for a quick generation of grids at different refinement levels. Having the inflation layers near the walls also offers the advantages of a structured grid and allows for the appropriate modelling of the boundary layer.

To carry out a grid convergence study, 4 grids were constructed at 4 different refinement levels. A close-up of the in-between tube region of these grids from 1 to 4, in order of refinement, is displayed in figures: 2.13 through 2.16. Here, both the structured and unstructured features of the mesh are clearly visualised. The number of elements is doubled between two successive grid refinements. The grids were constructed mainly taking into consideration the requirements for the low-Reynolds models (SA and SST). These are the models available in SU2 and, thus, the ones that are used in the optimization process. The high Reynolds models available in ANSYS-Fluent were mainly used for model validation as they provide results that are more closely aligned with the predictions of the empirical correlations.

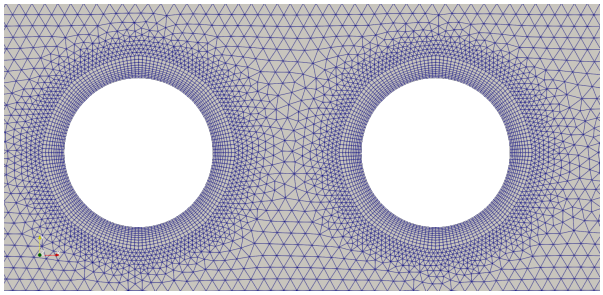

Figure 2.13: Close-up of the region in between the tubes - grid refinement level 1.

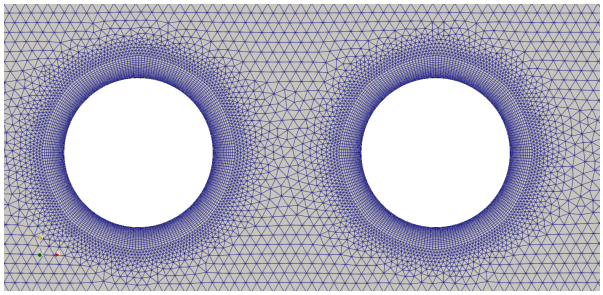

Figure 2.14: Close-up of the region in between the tubes - grid refinement level 2.

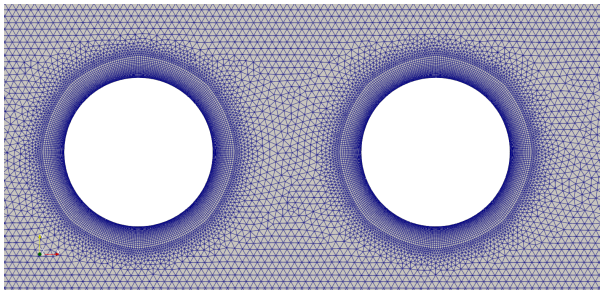

Figure 2.15: Close-up of the region in between the tubes - grid refinement level 3.

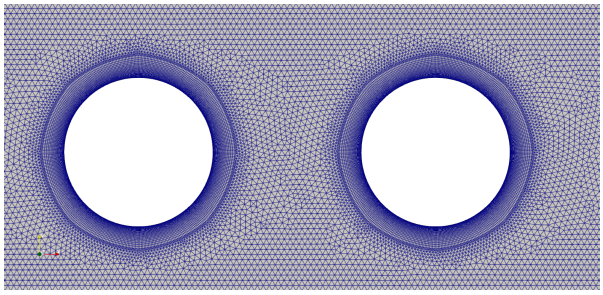

Figure 2.16: Close-up of the region in between the tubes - grid refinement level 4.

To construct these grids, several parameters were defined that describe the size and shape of the mesh elements. Each boundary edge (inlet, outlet, transverse boundaries and walls) was assigned a number of mesh elements. Additionally, a maximum element size was imposed on the whole domain surface. Lastly, the boundary layer was described using a total thickness, a growth ratio, and a number of mesh elements in the radial direction. These parameters are presented in table 2.1, and the growth ratio for the inflation layers is 1.1 for all refinement levels with a total thickness of $3e^{-4}$m. A closer view of the inflation region for the 4 grids is presented in figures: 2.17 through 2.20.

For each grid refinement and boundary layer, a range of y^+ values was also given in table 2.1. The y^+ value changes depending on the near wall treatment used by the various turbulence models. The lower bound of the range was obtained for the $k-\epsilon$ simulations which model the near wall region using a wall function. Whereas the upper bound was obtained for the SST and SA models which attempt to solve the near wall region.

The y^+ parameter is a dimensionless wall distance whose value indicates the relative importance of turbulent to viscous forces. Having a low value ($y^+ < 1$) shows that the flow is located in a highly viscous region, meaning that viscous forces become significantly more important than turbulent ones. For near-wall problems, low-Reynolds turbulence models integrate the wall effects into the model's equations. Thus, for these models, the boundary layer can be fully resolved without the use of a wall function. The y^+ parameter can be calculated as follows:

$$y^+ = \frac{y u_\tau}{\nu} \tag{2.36}$$

Where y is the absolute distance from the wall. u_τ is the friction velocity and it is a function of the shear stress, according to the following equation:

$$u_\tau = \sqrt{\frac{\tau_w}{\rho}} \tag{2.37}$$

Where τ_w is the wall shear stress which can be computed as:

$$\tau_w = \mu \frac{\partial u}{\partial y} \tag{2.38}$$

Where u is the flow velocity.

Refinement Level	Grid 1	Grid 2	Grid 3	Grid 4
Number of Elements	69178	112102	232366	367196
Number of Inflation Layers	10	20	30	40
Maximum Element size [m]	1.8e-4	1.5e-4	1e-4	8e-4
Range of Maximum y+	0.89-1.5	0.24-0.45	0.08-0.16	0.03-0.06
	Number of Divisons on Edge			
Inlet/Outlet	20	30	40	50
Top/Bottom	600	900	1200	1500
Tube Walls	150	200	250	400

Table 2.1: Parameters of the computational grids.

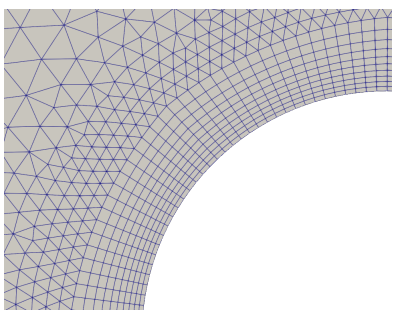

Figure 2.17: Inflation layer of grid refinement level 1.

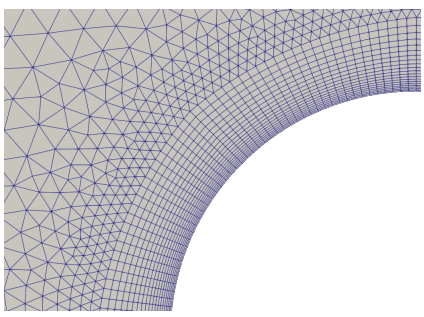

Figure 2.18: Inflation layer of grid refinement level 2.

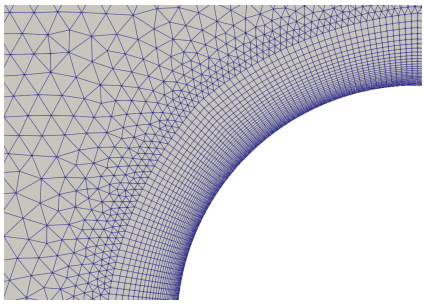

Figure 2.19: Inflation layer of grid refinement level 3.

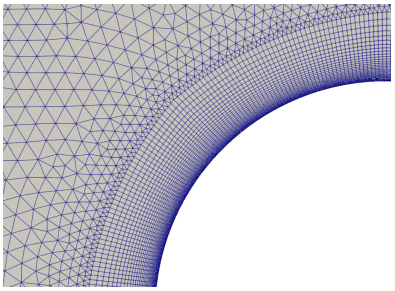

Figure 2.20: Inflation layer of grid refinement level 4.

The other possible approach for modelling wall-bounded flows is through the use of a wall function. A wall function is a semi-empirical approach consisting of a set of equations for momentum and energy that make the link between the variables of interest and corresponding parameters on the wall. This method is commonly used together with high-Reynolds turbulence models due to its computational efficiency. The implementation of a wall function means that the viscous near-wall region does not have to be directly resolved. The wall function may, however, be unsuitable for flows where low Reynolds number effects (viscous effects) are significant. The SST and SA models available in SU2 do not require a wall function to be implemented. Instead, these two models integrate their variables all the way to the wall. High Reynolds turbulence models, such as the $k-\epsilon$ models from ANSYS-Fluent, do require a wall function in their implementation.

The wall function used in all the following simulations with $k-\epsilon$ turbulence models is the standard wall function available in ANSYS-Fluent. Out of the 4 available options, the standard wall function was found to perform the best.

The standard wall function models the mean dimensionless velocity U^* in the near-wall region using a logarithm law, as shown in equation 2.39:

$$U^* = \frac{1}{\kappa} ln\left(Ey^*\right) \tag{2.39}$$

Where E=9.793 and $\kappa = 0.4187$ are empirical constants, and y^* is a dimensionless distance from the wall, computed using equation 2.40:

$$y^* = \frac{\rho C_\mu^{1/4} k^2 y}{\mu} \tag{2.40}$$

This dimensionless distance is a function of the local turbulent kinetic energy (k), the physical distance to the wall (y), fluid properties (ρ and μ) and a model constant (C_μ) whose value differs depending on the version of the $k-\epsilon$ model used. As shown in the previous section on turbulence modelling, the models can differ quite significantly in their definitions of model constants. This has the effect that the resulting wall region is modelled differently in the Realizable $k-\epsilon$ compared to the RNG or standard model.

The logarithm law, equation 2.39, is valid for flows where $y^* > 11.225$ in ANSYS-Fluent. When the dimensionless velocity is lower than this value ($y^* < 11.225$), the laminar stress-strain relationship will be applied: $U^* = y^*$. This implementation of the y^* was found to be inadequate for the standard $k-\epsilon$ and RNG models when applied to the 4 grids presented above. For these 2 models, the results obtained for the domains with denser grid refinement levels in the near wall region (Figures 2.19 and 2.20) significantly underestimate the pressure drop and heat transfer of the airflow through the tube bundle. This is not the case for the Realizable $k-\epsilon$ model, where the results were quite similar for all 4 near-wall grid refinement levels. Therefore, of the high-Reynolds models, only the Realizable $k-\epsilon$ can provide accurate results on highly refined grids. For this reason, Realizable $k-\epsilon$ is used and compared with the low-Reynolds models (SA and SST).

Other wall functions were used together with the $k-\epsilon$ models in ANSYS-Fluent. When compared to the Standard Wall Function, the Scalable wall function was found to underpredict the production of kinetic energy, whereas the Enhanced Wall Function was found to overpredict this parameter compared to the Standard Wall Function.

2.5.4. GRID INDEPENDENCE STUDY

The grid independence study was carried out on the four grids presented previously using three of the turbulence models described above. The simulations with the two low-Reynolds turbulence models, SA and SST,

were performed in SU2. The high Reynolds turbulence model Realizable $k-\epsilon$ simulations were performed in ANSYS-Fluent. The final results were compared based on the predicted dimensionless pressure drop and heat transfer. The pressure drop was expressed as an equivalent friction factor, while the heat transfer was characterized through the use of an average Nusselt number over the whole tube bundle.

The friction factor or pressure drop coefficient ξ is a function of the pressure drop, the number of tubes and the velocity at the minimum cross-section. This dimensionless quantity is double the value of the Euler number $\xi = 2Eu$. This formulation for ξ is also used by Zukauskas [17].

$$\xi = \frac{2\Delta p}{\rho U_m^2 n_R} \tag{2.41}$$

The Nusselt number over a tube bundle is a function of the heat transfer coefficient (h_c), a characteristic length (in this case, the tube diameter) and the thermal conductivity. The latter two parameters are constant in this case, but the average heat transfer coefficient depends on a variable called the logarithmic mean temperature difference ΔT_{LM} and the heat flux $\dot{q}$. The logarithmic mean temperature difference is a function of the wall, inlet and outlet temperatures as shown in equation 2.44. This formulation for the Nusselt number was adopted from the VDI Heat Transfer Atlas [22].

$$Nu = \frac{h_c D}{k_c} \tag{2.42}$$

$$h_c = \frac{\dot{q}}{\Delta T_{LM}} \tag{2.43}$$

$$\Delta T_{LM} = \frac{(T_w - T_{in}) - (T_w - T_{out})}{ln\left((T_w - T_{in}) / (T_w - T_{out})\right)} \tag{2.44}$$

Figures 2.21 and 2.22 illustrate how the output parameters change with increasing mesh refinement levels for the three turbulence models examined. Overall, each model shows similar trends. The low Reynolds flow models (SST and SA) used in SU2, and the Realizable $k-\epsilon$ model in ANSYS-Fluent show a small variation of the friction factor and the Nusselt number over the considered range of mesh refinement levels. The output results show a slight variation (either an increase or decrease) and then a tendency to plateau in the case of the denser meshes for both the ξ and the Nu.

To conclude, the results obtained for the grid independence study show that the RANS solver, regardless of the chosen turbulence model, provides consistent results even with a relatively coarse mesh, with the output parameters showing little change between the 4 meshes. This is observed despite the relatively large difference in the predicted Nu and pressure drop coefficient, such as in the case of the Realizable $k-\epsilon$ and SST models. The mesh density that is used for all the following simulations is that of grid 3, from Table 2.1, since it provides accurate results for all three turbulence models.

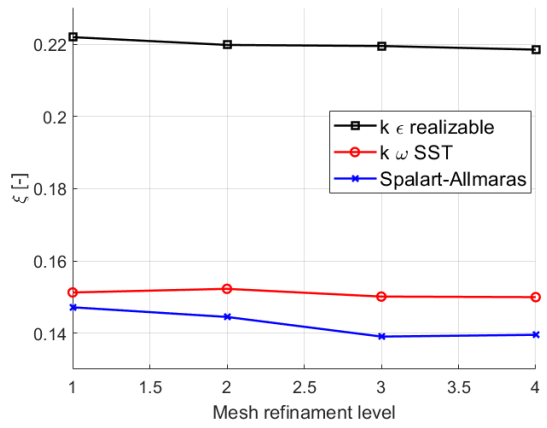

Figure 2.21: Pressure drop coefficient for the 4 gird refinement levels using different turbulence models.

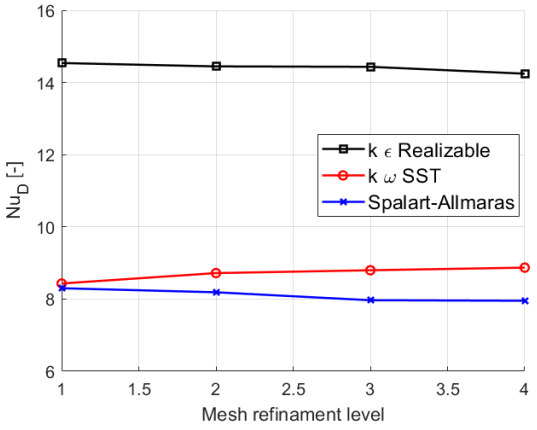

Figure 2.22: Average Nusselt number for the 4 gird refinement levels using different turbulence models.

2.5.5. SIMULATION CONVERGENCE

Before discussing the effects of the turbulence models on the simulation outputs, it is first necessary to assess the convergence of each simulation. The convergence of the steady-state simulation can be determined by evaluating the residuals of the model's equations. Generally, a steady-state RANS simulation can be considered to have converged if the residuals have decreased by six orders of magnitude.

For the current simulations, all the simulations with three turbulence models were able to converge to a steady state by exceeding the required six-order-of-magnitude reduction in residuals. Figure 2.23 shows the convergence history of the simulation using $k-\omega$ SST for grid 3. These residuals correspond to the equations of continuity, momentum, energy, and the 2 transport equations for k and ω. The simulation reached convergence after about 25000 iterations, with all residual terms dropping by about 10^{-6} from the initial values. Figure 2.24 shows the convergence history of the two variables of interest: pressure drop and outlet temperature. Both parameters reach convergence after about 15000 iterations.

Figure 2.25 shows the convergence history of the simulation using Realizable $k-\epsilon$ for grid 3. Again, the model reaches convergence, with its residual terms dropping by six orders of magnitude from the initial values. The main difference in this case is that convergence is reached somewhere after 4000 iterations. In Figure 2.26, the pressure drop and outlet temperature convergence is reached after around 800 iterations.

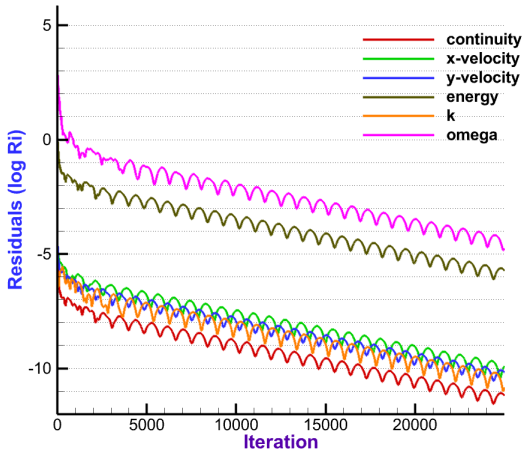

Figure 2.23: Convergence history of $k-\omega$ SST simulation for grid 3 in SU2.

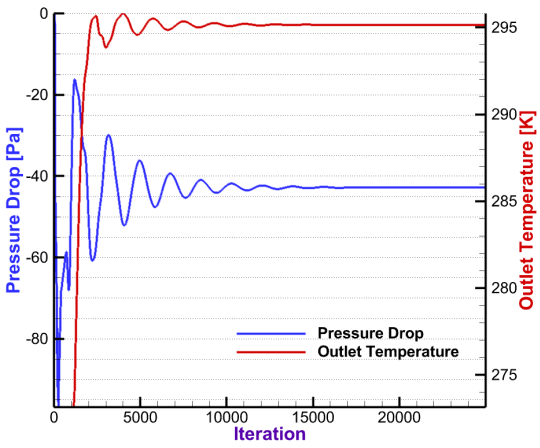

Figure 2.24: Outlet temperature and pressure drop history of $k-\omega$ SST simulation for grid 3 in SU2.

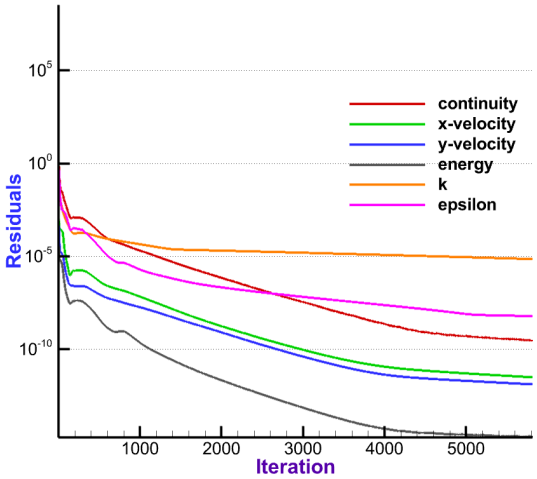

Figure 2.25: Convergence history of Realizable $k-\epsilon$ simulation for grid 3 in ANSYS-Fluent.

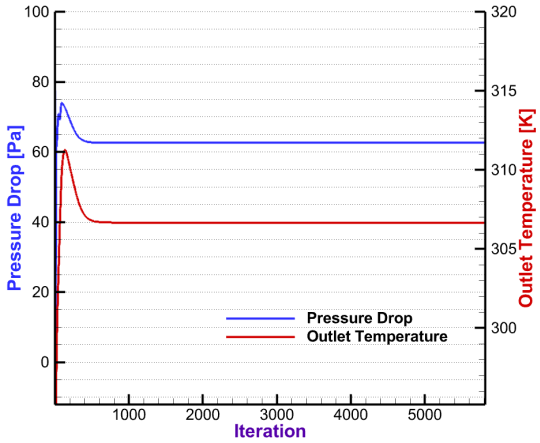

Figure 2.26: Outlet temperature and pressure drop history of Realizable $k-\epsilon$ simulation for grid 3 ANSYS-Fluent.

2.5.6. EFFECT OF TURBULENCE MODEL

To assess the accuracy of these models, the dimensional and non-dimensional output quantities obtained from the CFD simulations of the 7-tube layout are compared with the predictions of the empirical correlations for the same BTHX configuration. This comparison is given in Table 2.2. The empirical correlation results were obtained using the same Hexacode tool mentioned in Section 2.1.1.

Case	Δp [Pa]	Δp_{err} [%]	ξ	ξ_{err} [%]	ΔT [K]	ΔT_{err} [%]	Nu_D	$Nu_{D,err}$ [%]
Correlation Data	66.6	-	0.2314	-	36.139	-	16.864	-
Realizable $k-\epsilon$	62.596	6.012	0.2195	6.036	33.505	7.291	14.43	14.41
$k-\omega$ SST	42.804	35.729	0.1501	35.717	22	39.12545	8.79	47.83
SA	39.645	40.472	0.139	53.237	20.146	40.471	7.96	52.75

Table 2.2: Output parameters computed using different turbulence models on grid 3 compared to the empirical correlation predictions.

The data points in table 2.2 show that the Realizable $k-\epsilon$ model of ANSYS-Fluent provides the closest results to those found through the empirical correlations. The table contains information about the pressure drop Δp, and the temperature rise over the tube bundle ΔT for each turbulence model. The dimensionless parameters (friction factor and average Nusselt number) are also included. The two models provided by SU2, SA and SST, provide significantly lower outputs in terms of both ξ and Nu than the empirical correlations. The outputs of SA and SST are, however, similar to each other with SST being the more accurate of the two low-Reynolds models. The better performance displayed by the Realizable $k-\epsilon$ model was to be expected given the information found in literature. The same observation regarding the better performance of $k-\epsilon$ models was also made by other works such as West [5] and Blackall et al. [2].

As pointed out by Blackall et al. [2], the low-Reynolds models (SA and SST) predict an early separation when compared to models such as $k-\epsilon$, for flows with Re in the sub-critical regime. This was found to be the case for these simulations as well. Figures 2.27, 2.28 and 2.29 show the velocity contours near the top of tube 6 in the SA, SST and Realizable simulations, respectively. The flow reattachment (green) and separation (black) points are represented in a qualitative manner in the figures below. These figures are meant to indicate that the low-Reynolds models predict a delayed reattachment and a faster separation than the high-Reynolds turbulence model. This means that for models such as Spalart-Allmaras and SST, attached flow is present on a smaller section of the tube surface than for the Realizable model. The consequence is that for the Realizable $k-\epsilon$ model, higher velocities are present on a larger section of the tube walls, and thus, the friction drag is more significant. In turn, this contributes to an increase in the overall pressure drop predicted by the model.

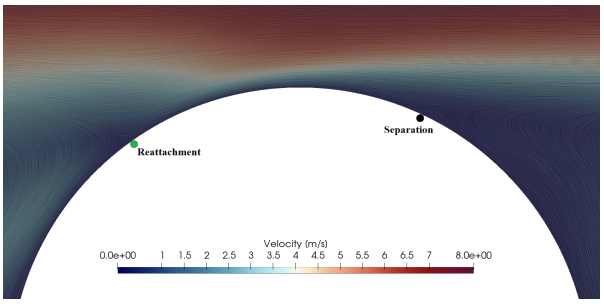

Figure 2.27: Flowfield over tube 6 for the SA simulation for grid 3.

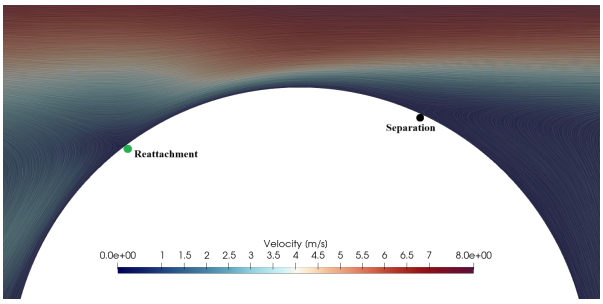

Figure 2.28: Flowfield over tube 6 for the $k-\omega$ SST simulation for grid 3.

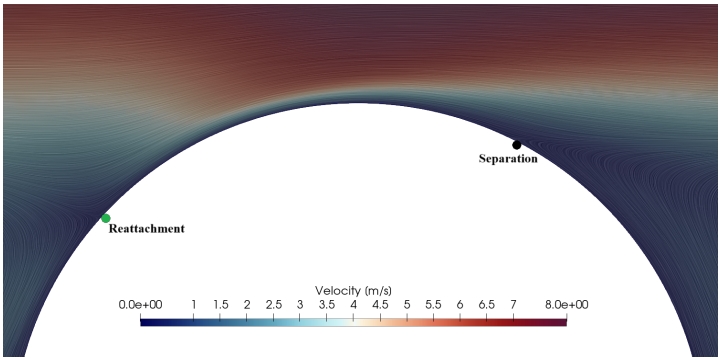

Figure 2.29: Flowfield over tube 6 for the Realizable $k-\epsilon$ simulation for grid 3.

Figure 2.30 displays a comparison between the contours for turbulent kinetic energy k obtained for the Realizable $k-\epsilon$ and the $k-\omega$ SST simulations. The first model (Realizable) predicts a larger production of turbulent kinetic energy around the tube walls than the second (SST). Thus, the turbulence inside the flow is much higher for the high Reynolds model than for SST. These higher levels of turbulence in the wake of a tube and around the next tube downstream from it indicate higher levels of mixing occurring inside the tube bundle. Increased mixing corresponds to increased heat transfer and friction. This explains higher outlet temperature and ΔT predicted by the Realizable $k-\epsilon$ model. As previously shown in Figure 2.28, for the SST model, most of the flow is already detached from the tube walls. Most of the fluid moves through the freestream region further away from the walls, meaning that there is little chance for mixing to occur and for heat to dissipate in the fluid in large quantities. This difference in the amount of turbulent kinetic energy and the different mixing levels occurring in the tube bundles for the two turbulence models explains the discrepancy in the Nusselt number.

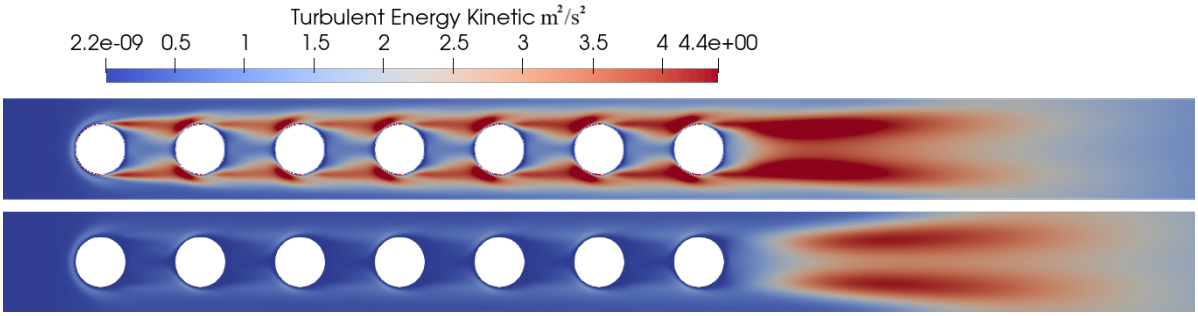

Figure 2.30: Comparison of the turbulent kinetic energy for the Realizable $k-\epsilon$ (top) and the $k-\omega$ SST (bottom) simulations.

A similar trend is observed for the eddy viscosity in Figure 2.31. The SA model uses only the eddy viscosity equation to characterize the turbulence levels in the flow, but the trend is similar to the one observed for turbulent kinetic energy. The Realizable $k-\epsilon$ model shows increased levels of eddy viscosity around the tube walls compared to the two low-Reynolds models. This again affects the predicted outlet temperature and pressure drop. One observation that should be made here is about the higher levels of eddy viscosity at the outlet for the first two models (Realizable and SST), likely due to a slight overestimation of the turbulence length scale at the inlet. However, this was found to not affect the final results in a significant way (less than 0.1% difference in ΔT depending on the chosen inlet turbulence length scale).

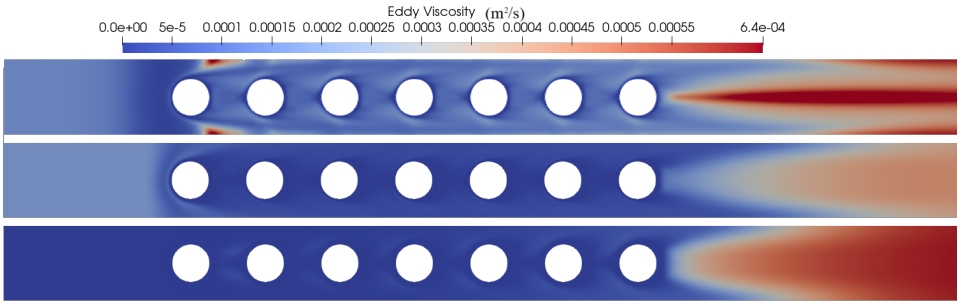

Figure 2.31: Comparison of the turbulent eddy viscosity for the Realizable $k-\epsilon$ (top), $k-\omega$ SST (middle) and the SA (bottom) simulations.

Differences between the high and low Reynolds turbulence models can also be seen in the velocity flow fields. According to West [5], the SST model is expected to produce slightly higher velocities in the free stream region. This behaviour can be seen in Figure 2.32, where the velocity profiles between tubes 5 and 6 are displayed. Spalart-Almaras and SST have nearly identical velocity profiles, while the Realizable $k-\epsilon$ shows a slightly lower velocity near the top and bottom boundaries. The low-Reynolds models produce higher velocities in the free-stream region due to the lower levels of turbulent kinetic energies computed by these models. The Realizable $k-\epsilon$ model presents lower velocities in the free-stream region because the flow undergoes significant mixing and therefore the stream-wise velocity profile is more uniform.

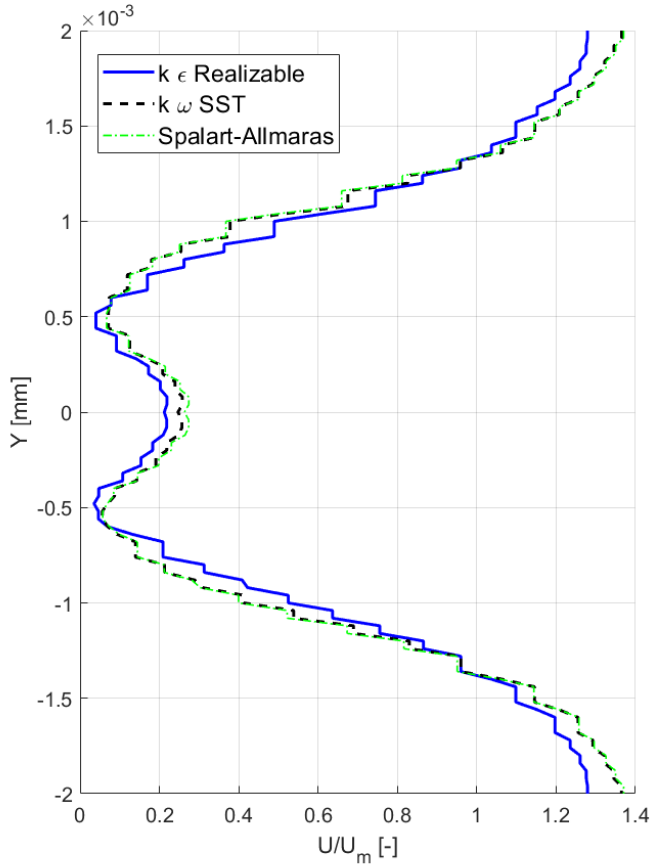

Figure 2.32: Stream-wise velocity profile between tubes 5 and 6 comparison between the Realizable $k-\epsilon$ and the $k-\omega$ SST.

Another illustration of the velocity flow fields for the three turbulence models is given in Figure 2.33. It is worth noting that due to the use of symmetric boundary conditions, the expected asymmetry described in literature by West [5] in the flow is absent. This can likely be addressed by implementing periodic boundary conditions. The main observation to be made in this figure is the expansion and compression occurring throughout the tube bank in the freestream area. This behaviour is more pronounced in the Realizable $k-\epsilon$ model with the velocity peaks being visible near the minimum cross sections. In the Spalart-Allmaras and SST model, there is a near-uniform increase in velocity in the freestream area. Otherwise, the wakes are similar to those described by pattern C in Figure 2.2 as expected, given the layout of the tube bank.

Overall, the results found for the CFD simulations with different turbulence models indicate that Realizable $k-\epsilon$ can be used as a high-fidelity solver for flows around $Re = 1000$. This model is used to provide more accurate results for the optimal designs obtained with low-fidelity solvers such as SST.

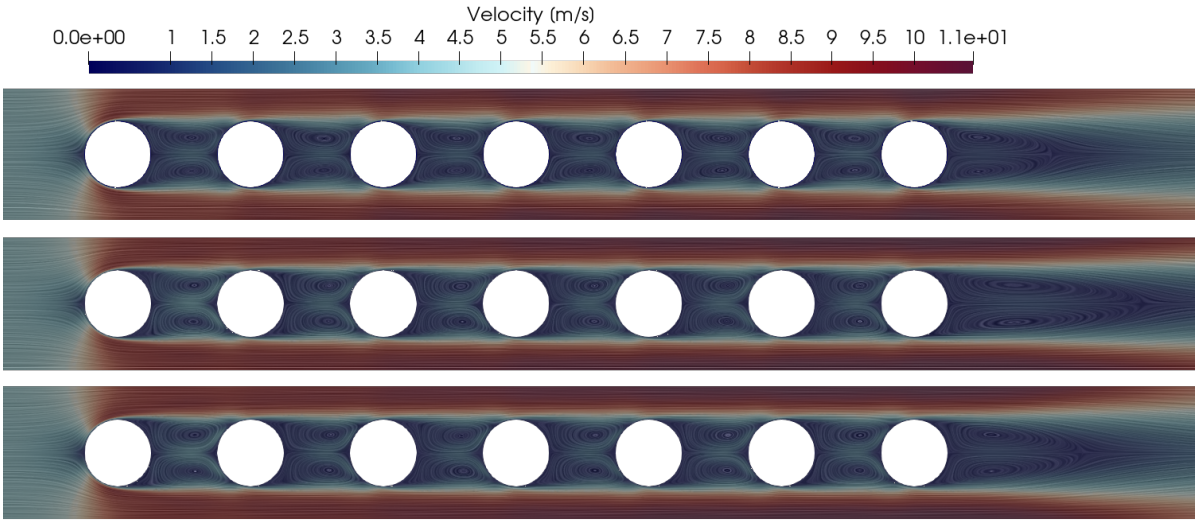

Figure 2.33: Comparison of the velocity flow fields for the Realizable $k-\epsilon$ (top), $k-\omega$ SST (middle) and the SA (bottom) simulations.

2.6. EFFECT OF BOUNDARY CONDITIONS ON RESULTS ACCURACY

2.6.1. PERIODIC AND SYMMETRIC BOUNDARY CONDITIONS

Figure 2.2 shows that the wake patterns for an in-line tube bundle of $P_L = P_T = 2$, in a subcritical flow regime, are located in the transition region between B and C. Consequently, it is possible for asymmetrical flow patterns to develop in the wakes of the tubes of this $P_L = P_T = 2$ array. However, because the previous simulations were computed with symmetric boundary conditions, the asymmetrical flow patterns similar to those identified by West [5] could not be modelled. Carrying out the same simulations with periodic boundary conditions on the transverse boundaries yields different results depending on the solver (SU2 or ANSYS-Fluent). For the Realizable $k-\epsilon$ model from ANSYS-Fluent, the symmetric flow patterns in the wake persist, and the outputted parameters are within 0.1% of the previous results.

For the SST model from SU2, the differences are more pronounced. As can be seen in Figure 2.34, switching to periodic boundary conditions does induce the asymmetric vortex structures in the wakes of the tubes. Another difference can be encountered in the flow parameters. The periodic boundary condition simulation produces a slight increase in the pressure drop of almost 3.5% while maintaining a constant outlet temperature compared to the symmetric boundary simulation. These results make the use of periodic boundary conditions preferable when modelling flows with the SST model. A similar trend was observed for the Spalart-Allmaras model, and the corresponding results and velocity contours are reported in Appendix B.

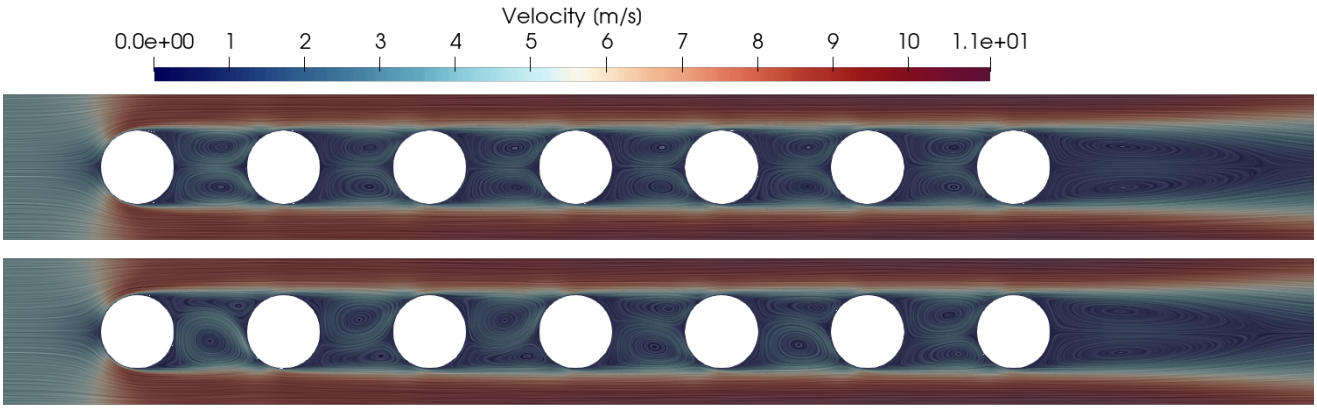

Figure 2.34: Comparison of the velocity profiles for the SST $k-\omega$ simulations with symmetric (top) and periodic (bottom) boundary conditions.

Case	Δ p[Pa]	Δ T [K]	Δp_{diff} [%]	ΔT_{diff} [%]
Symmetric Boundary	42.804	295.15	-	-
Periodic Boundary	44.299	295.741	3.492664	0.2

Table 2.3: Output quantities computed using periodic and symmetric boundary conditions for the 7 tube array using the SST $k-\omega$ model.

2.6.2. NUMBER OF TUBES

So far, all simulations have been carried out on the same domain with seven tubes. However, it is important to understand whether the conclusions derived about the accuracy of the turbulence models would be valid for cases with a larger number of tubes. It has already been demonstrated that the high-Reynolds models are preferable for the current flow conditions and that the low-Reynolds models produce less accurate results. To extend the validity of these conclusions, two other different cases were analyzed.

The first case is a 10-tube bundle where the flow has $Re_D \approx 1080$ and the relative pitches between the tubes are $P_L = P_T = 2$. The second case is a 15-tube bundle with $Re_D \approx 1050$ and the same relative tube pitches. The difference between the Re numbers of the two cases is due to differences in fluid properties and velocity at the inlet. Both cases were simulated with the Realizable $k-\epsilon$ and $k-\omega$ SST models, and the results were reported in the dimensionless form to account for the difference in flow parameters and fluid properties. These results can be seen in Figures 2.35 and 2.36, plotted against the results obtained from the empirical correlations.

The trends shown in these graphs confirm the conclusions regarding the accuracy of the turbulence models compared to the correlation data for the given flow conditions. The Realizable $k-\epsilon$ model actually computed results closer to those of the correlations, with the error for friction factor decreasing from 6% for 7 tubes to 3.9% for 15 tubes. The same is not true for the SST model, where the error of this parameter increases significantly from 32.7% to 44.9% when the number of tubes is increased. This can be partially explained by recalling the trends in Figures 2.27 through 2.29. The issue of the low-Reynolds models of predicting early flow separations and thus underestimating the friction factor becomes more significant as more tubes are added to the model. The high Reynolds model predicts a delayed flow separation and, therefore, outputs higher friction factors even for lower numbers of tubes.

Similar trends can be observed for heat transfer and the average Nusselt number. A more detailed overview of the results obtained for each simulation can be found in Annexe B, in Table B.2.

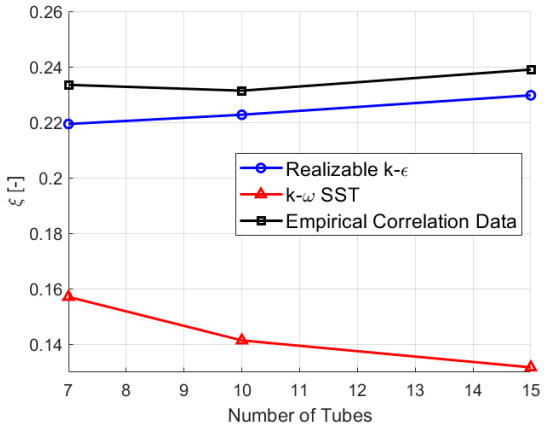

Figure 2.35: Friction factor for different numbers of tubes inside a BTHX with $P_L = P_T = 2$, for flows around $Re \approx 1000$.

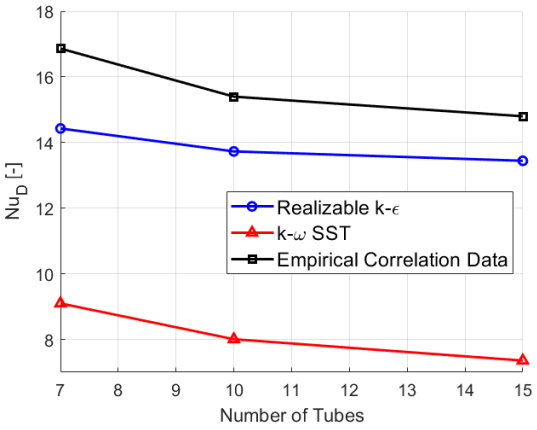

Figure 2.36: Average Nusselt number for different numbers of tubes inside a BTHX with $P_L = P_T = 2$, for flows around $Re \approx 1000$.

2.7. LOW REYNOLDS FLOW ANALYSIS

The previous case study on the 7-tube bundle has shown which turbulence models are most appropriate for modelling flows in the transition region of $Re \approx 1000$. However, this does not mean that the conclusions drawn apply to other flow conditions. As was shown from work by West [5] and Blackall et al. [2], $k-\epsilon$ based models can still be reliable for flows where the Reynolds number is higher. This does not hold true for flows where the Reynolds number is lower. By conducting three simulations based on the tube bundle presented by Kasagi et al. [7], it was shown that low-Reynolds-number models, such as SST, perform better in reproducing experimental results for flows of $Re < 250$. This study analyses a 21 round tube BTHX at a flow of $Re_D \approx 200$ calculated using the velocity at the minimum cross-section U_m (Kasagi et al. [7] reports $Re_D \approx 100$ based on the inflow velocity U_∞).

This case corresponds to a highly packed tube bank with a transverse pitch ratio of $P_T = 2.28$, a longitudinal pitch ratio of $P_L = 1.31$ and a tube diameter of D=0.5 mm. Kasagi et al. [7] report experimental measurements carried out on this tube bank in terms of pressure drop over the tube rows Δp and temperature rise ΔT. The grid for the following simulation was constructed using the same mesh density as grid 3 in Figure 2.15. The boundary conditions used are provided below:

- Inlet velocity: 2.77 m/s
- Inlet Temperature: 308.15 K
- Inlet Turbulence intensity: 1%
- Inlet Turbulence length scale: 0.000114 m
- Wall Temperature: 338 K
- Outlet Pressure: 0 Pa
- Absolute Pressure: 1 atm

The velocity contours for the simulations carried out on this tube array are displayed in Figure 2.37. The longitudinal tube spacing is too small for any distinguishable wake patterns to form after each tube. However, the wake pattern behind the last tube is significantly different depending on the chosen turbulence model. These resemble the results for the wake patterns found in the simulations of the 7-tube test case, with the $k-\epsilon$ models producing the shortest, while SST produces the longest wake. Another pattern that persists from the previous simulations is the higher estimation of kinetic turbulent energy by the Realizable $k-\epsilon$ model. However, in this case, since the flow is largely laminar, this additional turbulent kinetic energy leads to an overestimation of the pressure drop and heat transfer. This is shown in Table 2.4 where pressure drop and temperature rise over the tube bundle of the three turbulence models are compared with the available

experimental data. In this case, the low-Reynolds models produce accurate results within 2.5-3% accuracy for pressure drop and around 5.5% for temperature rise. The Realizable $k-\epsilon$ model significantly overestimates the quantities of interest with about 40% discrepancy for Δp and around 24% for ΔT.

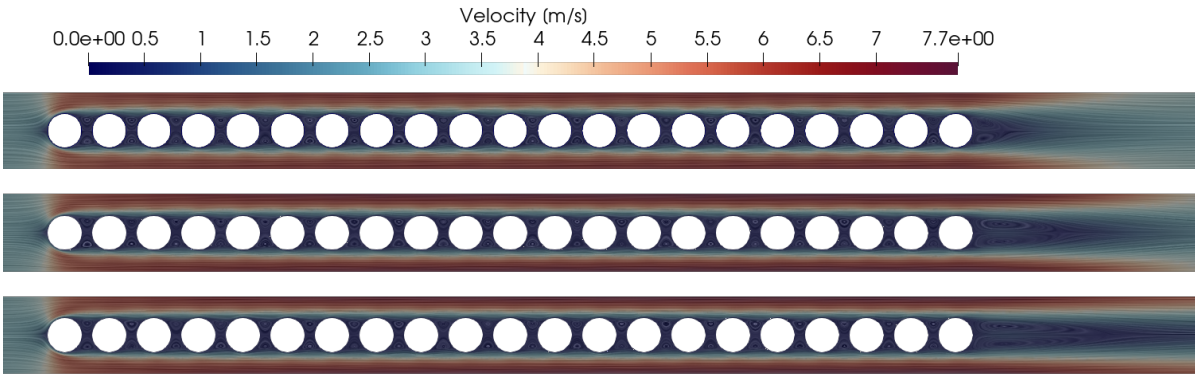

Figure 2.37: Comparison of the velocity profiles for the realizable $k-\epsilon$ (top), SA (middle) and $k-\omega$ SST (bottom) for the tube bundle described by Kasagi et al. [7].

Case	Realizable $k-\epsilon$	$k-\omega$ SST	SA	Experimental Data (Kasagi et al. [43])
Δp [Pa]	58.008	42.830	42.718	41.600
ΔT [K]	24.118	20.450	20.482	19.400
Δp_{err} [%]	39.442	2.957	2.688	-
ΔT_{err} [%]	24.320	5.412	5.577	-

Table 2.4: Output parameters computed with the Realizable $k-\epsilon$, SA and SST for the tube bundle described by Kasagi et al. [7] and compared to the experimental data.

2.8. MODELING GUIDELINES

This chapter has shown that the choice of turbulence models is crucial in accurately modelling the flow through an in-line BTHX using steady-state RANS. For the flow conditions of interest $Re_D \approx 1000$, the best choice was found to be a high-Reynolds model such as Realizable $k-\epsilon$, which performs well even with a standard wall function implemented. This model provides better estimations of both pressure drop and heat transfer inside a tube bank. Realizable $k-\epsilon$ also provides predictions for the flow separation and reattachment on the tube walls in agreement with the findings of Blackall et al. [2]. The optimization framework presented in the next chapter uses SU2 for CFD evaluations. Therefore, the CFD analysis within the optimization process needs to be carried out with the low-fidelity model SST, and the output of the optimization should be validated using the high-fidelity $k-\epsilon$ model. For the SST and Spalart-Allmaras models, the accuracy of the results also decreases with an increasing number of tubes, as seen in Figures 2.36 and 2.35. Therefore, the optimization process was carried out on the 7-tube test cases in order to minimize the error of the CFD computations.

Some aspects of the computational domain were also discussed in this chapter. The optimization process presented in the following chapter requires multiple CFD analyses of the flow to evaluate the objective function as well as a few adjoint evaluations. The computational cost of this process is significantly higher than that for the numerical analyses presented so far. For this reason, it is essential to be efficient in the design of the flow domain that will be employed in the optimization process. Grid 3 2.15 with a medium refinement level was chosen as a result of the grid independence study. The far field of this mesh was shortened in order to reduce the number of grid elements by almost 50 %. The grid density was, however, kept constant. This reduction decreases the number of elements in the domain from 234618 to 127403, thus significantly reducing the size of the computational domain to almost half for Grid 3. The flow field around the tubes was not affected by this shortening of the far-field, and the figures of merit (pressure drop and outlet temperature) suffer variations of under 0.5% from the original results presented in Table 2.2.

3

Shape Optimization Of Tubes for In-line Arrays

This chapter describes the framework for the optimization of BTHX tube geometry. The objective is to improve the pressure drop of in-line tube banks while maintaining heat transfer performance.

Section 3.1 provides some background to the shape optimization of BTHX tubes, mainly focusing on the works of Bacellar et al. [9] and Hilbert et al. [8]. The theoretical background for the adjoint method is provided in Section 3.1.2. The CAD parametrization procedure, using NURBS curves, is explained in Section 3.1.4. The capabilities of SU2 to perform adjoint-based optimizations are also reviewed in Section 3.1.3.

The optimization framework is presented in Section 3.2, and the main elements of this framework are discussed. This framework is then applied to the 7-tube in-line BTHX case study presented in Section 2.5. The choices of constraints and design variables for this optimization are presented in Section 3.1. Section 3.4 compares the outputs of two optimizations carried out using 2 different optimizers, SLSQP and SNOPT.

3.1. Shape Optimization

The most comprehensive literature survey on HX optimization was carried out by Tancabel et al. [44] and presents the most significant works published between 1996-2017 on this topic. The main takeaway from this study is that layout optimization is far more prevalent than shape optimization, and virtually no studies cover shape optimization for in-line BTHX. For this reason, the literature on the shape optimization of staggered BTHX is of great importance for this thesis.

Most of the works presented by Tancabel et al. [44] perform optimizations using gradient-free methods such as parametric studies or using multi-objective genetic algorithms. At the moment, not much literature has been published on the use of adjoint or other gradient-based methods in the optimization process of BTHX. Simanowitsch et al. [45] point out that while genetic algorithms provide larger design flexibility, the computational cost is ten to twenty times larger compared to gradient-based methods. This makes gradient-based methods such as the adjoint method preferable, especially when dealing with many design variables. Generally, the main difficulty of the adjoint method is the implementation of the gradient computation. Fortunately, SU2 provides an efficient way of computing the adjoint gradient through the use of algorithmic differentiation. Some background on adjoint-based optimizations with SU2 is presented later in this section.

3.1.1. Tube Shapes

The first study to consider the shape of the tubes as a possible way to improve the performance of BTHXs was Matos et al. [46]. This study primarily focuses on the layout of staggered BTHX. Matos et al.[46] have also shown that elliptical tubes perform better in terms of heat transfer than round tubes at a $Re_L \approx 500$. In this case, the Reynolds number is assessed using the length of the tube row. The performances of the BTHX were assessed with a 2D steady-state finite element (FEM) solver. Matos et al. [46] perform a parametric study where the variables were the transverse pitch and the ellipse eccentricity. Matos et al. [47] extend this work to finned tube HXs using 3D FEM simulations.

A similar study was undertaken by El Gharbi et al. [48]. Besides the elliptical and round tubes, this study also covers airfoil-shaped tubes. El Gharbi et al. [48] simulate, using $k-\epsilon$ RNG, 3 staggered arrays of identical

layouts composed of 5 tubes. Each layout featured a different tube shape: round, elliptical or airfoil. The results were reported in terms of Nusselt and Euler numbers at $5000 < Re < 25000$, and the empirical correlations of Zukauskas [1] were used to verify the round tube simulations. The results show that the elliptical and airfoil-shaped tubes for the given Re range showed a lower pressure drop than the circular tubes. However, the Nusselt number and the heat transfer coefficient were always larger for round tubes.

The work of Hilbert et al. [8] is one of the first studies covering only the shape optimizations of BTHX. The authors used a genetic algorithm to generate tube shapes within a determined design space without optimizing the layout of the BTHX. These designs were used to construct a Pareto front, as shown in Figure 3.1. The tube geometry was constructed using NURBS (non-uniform rational B-splines) curves where the tube's upper and lower surfaces were each described by 4 parameters. The objective function was evaluated using CFD simulations carried out with ANSYS-Fluent. The flow conditions were characterized by a $Re = 170$ based on the transverse spacing. The domain consisted of 4 tubes in a staggered array. The tube shapes were maintained identical to each other throughout the optimization process. Also, the upper and lower surfaces of the tubes were kept symmetrical. Figure 3.2 shows some of the resulting tube shapes.

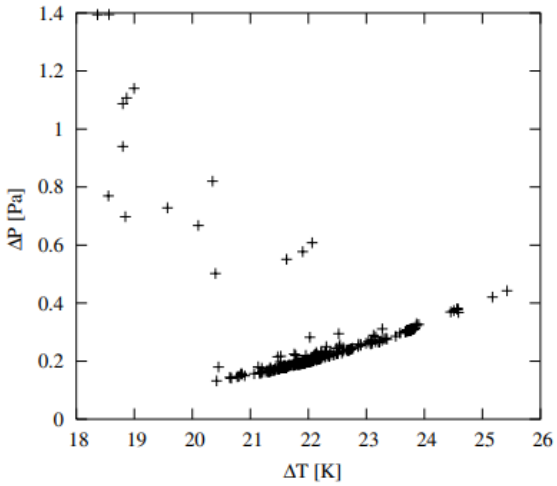

Figure 3.1: Pareto front obtained by Hilbert et al. [8] for the optimization of BTHX tube shapes using a genetic algorithm

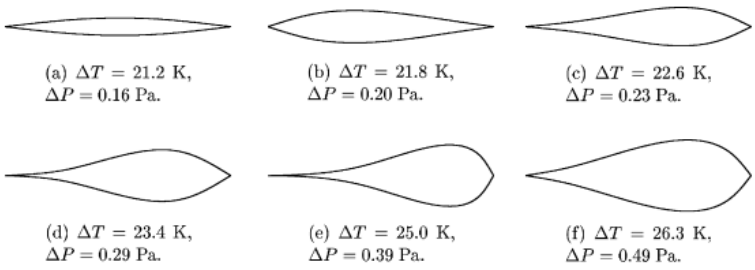

Figure 3.2: Examples of tube shapes obtained by Hilbert et al. [8]

One of the most comprehensive design optimizations for BTHX was carried out by Bacellar et al. [9] for staggered arrays. This study presents the first coupled shape and layout optimization in the literature, while also using CFD simulations to assess the objective function. The parameterization of the tube surface was done using NURBS curves as in the work carried out by Hilbert et al. [8]. Before starting the optimization process, Bacellar et al. [9] investigate the performances of 5 different tube shapes displayed in Figure 3.3. The blunt-shaped tubes (ellipse and round) are characterized by a greater heat transfer and larger friction factors, while the opposite is true for the airfoil-shaped tubes.

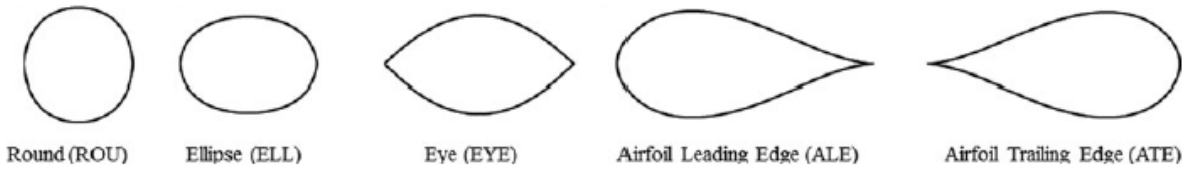

Figure 3.3: Tube shapes investigated by Bacellar et al. [9]

Bacellar et al. [9] also used a genetic algorithm for the optimization. The design variables are the coordinates of 4 points used to define the NURBS curves, the longitudinal and transverse pitches, the width and chord of the tubes, the number of tubes in the longitudinal and transverse directions and the inlet boundary conditions. These variables are displayed in Figure 3.4. The objective was to minimize the HX's overall pressure drop and volume while maintaining a heat transfer rate of 1kW. The final designs obtained after the optimizations are compared to a microchannel HX in Figure 3.5. This figure, 3.5, also displays the Pareto fronts obtained after 3 sets of optimizations based on 3 different sets of constraints. The NTHX-001 represents a tube shape for which Bacellar et al. [9] carried out an experimental investigation which is used to validate the CFD model.

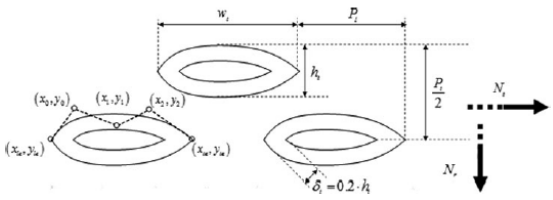

Figure 3.4: Design variables used by Bacellar et al. [9]

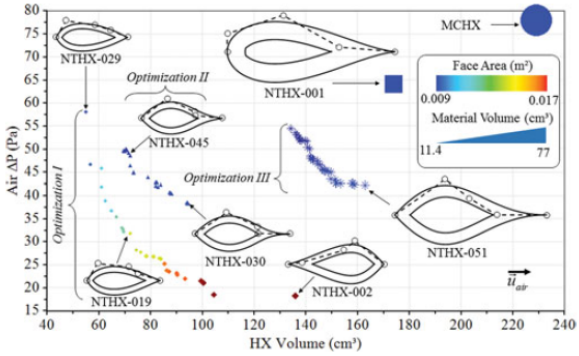

Figure 3.5: Pareto front obtained by Bacellar et al [9]

Tancabel et al. [49] expanded on the work of Bacellar et al. [9] by incorporating a FEM analysis for the tube walls, thus adding an additional material constraint on the optimization process. Tancabel et al. [49] perform 4 sets of optimizations: in two of them only the layout was optimized while in the other 2 shape and layout optimization were included. The optimal BTHX designs produced with shape optimization were found to be superior in terms of BTHX core volume compared to those where only the layout was optimized.

An example of an optimization on in-line BTHX is provided by Pai Raikar et al. [10]. The shape and layout optimization of a 4 elliptical in-line BTHX is presented in this study. This optimisation aims to minimize pressure drop while maintaining an almost constant heat transfer rate and a constant tube cross-sectional area. The optimization is gradient-based, and the gradient is computed using the adjoint method. The parametrization of the tube surfaces was also performed using NURBS curves. This method proves to be quite computationally efficient, achieving an optimal design within 9 design iterations. The improvements obtained in pressure drop were almost 30% with all the constraints being met. A comparison between flowfields of the baseline and optimized designs produced by Pai Raikar et al. [10] is shown in Figure 3.6.

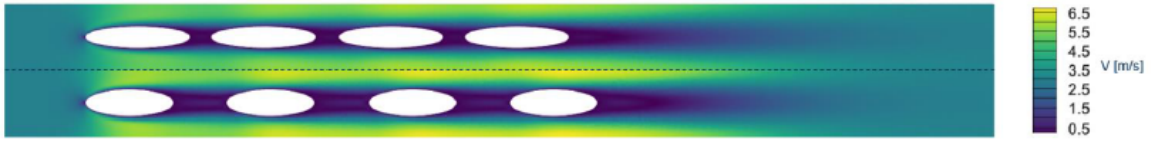

Figure 3.6: Comparison of the flow field for the optimized (top) and baseline (bottom) designs produced by Pai Raikar et al. [10].

3.1.2. ADJOINT METHOD

The adjoint method is a cost-effective way of computing the derivative of an objective function with respect to a large number of variables using the chain rule. The numerical cost of the adjoint method is independent of the number of variables. Unlike a finite difference method, which requires a function evaluation for every variable, the adjoint method only requires 2 evaluations to perform the sensitivity analysis of the objective function. The adjoint method is presented below taking inspiration from the work of Albring et al. [50].

A given objective function $J = J(\alpha, U(\alpha))$ can be defined in terms of design variables α and the state variables (flow field) $U(\alpha)$. The resulting derivative with respect to the design variables is:

$$\frac{dJ}{d\alpha} = \frac{\partial J}{\partial U}\frac{dU}{d\alpha} + \frac{\partial J}{\partial \alpha} \tag{3.1}$$

Where the first and third partial derivatives of this equation are trivial to compute, but the derivative of the state variables to the design variables, namely $\frac{dU}{d\alpha}$, is much more challenging to solve. To compute this derivative directly would be quite difficult. In order to solve this derivative, an equation that governs the state variables needs to be introduced:

$$R(U, \alpha) = 0 \tag{3.2}$$

And the differentiation of this state equation would yield:

$$\frac{\partial R}{\partial U}\frac{dU}{d\alpha} + \frac{\partial R}{\partial \alpha} = 0 \tag{3.3}$$

The derivative of the state variable $\frac{dU}{d\alpha}$ can be computed by rewriting equation 3.3 as:

$$\frac{dU}{d\alpha} = -\left[\frac{\partial R}{\partial U}\right]^{-1}\frac{\partial R}{\partial \alpha} \tag{3.4}$$

Equation 3.4 is substituted in 3.1 to obtain a formulation for $\frac{dJ}{d\alpha}$ independent of $\frac{dU}{d\alpha}$. The resulting expression is:

$$\frac{dJ}{d\alpha} = -\left[\frac{\partial J}{\partial U}\left(\frac{\partial R}{\partial U}\right)^{-1}\right]\frac{\partial R}{\partial \alpha} + \frac{\partial J}{\partial \alpha} \tag{3.5}$$

To write the adjoint equation, the adjoint variable λ has to be first computed as:

$$\lambda^T = -\frac{\partial J}{\partial U}\left(\frac{\partial R}{\partial U}\right)^{-1} \tag{3.6}$$

Then the adjoint equation for the objective function $J(\alpha, U(\alpha))$ is:

$$\frac{dJ}{d\alpha} = \lambda^T\frac{\partial R}{\partial \alpha} + \frac{\partial J}{\partial \alpha} \tag{3.7}$$

To determine the gradient of the objective function $J(\alpha, U(\alpha))$, it is sufficient to evaluate equation 3.7, which means solving one linear system of equations. The advantage of the adjoint method is that once the adjoint variable, λ, is solved, the gradient computation is very efficient, regardless of the number of design variables.

In the context of a CFD-based optimization, the term used above can be identified as:

- α - design variables: layout and/or surface parametrization
- $U(\alpha)$ - state variables: flow field (p, u, ρ, T)
- $R(U, \alpha)$ - state equation: Residuals of the discretized governing equations
- $J(U, \alpha)$ - objective function: Pressure Drop, Outlet Temperature, User Defined, etc.

There are two formulations of the adjoint problem: discrete and continuous. For the continuous adjoint method, the adjoint equations are derived from the continuous form of the governing flow equations. Then, the discretization takes place directly on the adjoint equations. In the second approach, the discrete adjoint equations are derived from the discrete flow equations. This ensures that the computed gradients are consistent with the discrete formulation of the objective function used in the numerical optimization process.

The discrete adjoint approach can obtain the exact gradient of the discrete objective function and is much easier to implement, according to Giles et al. [51]. The discrete adjoint method is integrated into the existing solver since it works within the same discretization framework as the flow solver. This allows for the reuse of the numerical methods and infrastructure already implemented for the direct problem, such as sparse matrix solvers and preconditioners. The approach used in this thesis is the discrete adjoint method.

3.1.3. SHAPE OPTIMIZATION IN SU2

The implementation of the discrete adjoint solver in SU2 is described in Albring et al. [50] where the adjoint equations are obtained through an Algorithmic Differentiation technique. This framework is then used to compute the surface sensitivity for the LM1021 airfoil profile (shape described by Morgenstern et al. [52]) with the minimization of the drag coefficient as the objective function.

For the purposes of this thesis, the study carried out by Economon [11] is much more significant since it presents an optimization study where heat transfer is considered. Economon [11] covers the implementation of a flow simulation and an adjoint-based shape design approach for incompressible flow problems with heat transfer and variable density in SU2. The test case presented by Economon [11] for the adjoint shape design is the optimization of a 2D heated cylinder, where the objective was to increase the heat transfer rate while constraining the maximum drag coefficient. The internal area was also constrained to maintain it equal to or larger than the initial design. The flow conditions for this case study were at $Re = 40$ based on a cylinder diameter of $1m$. The CFD setup is similar to the ones presented in chapter 2, where the cylinder was modelled as a no-slip and constant temperature boundary condition. The fluid property model is also the same considered in chapter 2 of this thesis, where the fluid is modelled as an ideal gas with variable density and viscosity.

As a result of the optimization process, Economon [11] obtains a 1.3% increase of heat transfer rate while also reducing the drag by 3.5%. A comparison between the baseline and optimized designs is given in Figure 3.7. This approach presented by Economon [11] is very similar to the one that will be presented in section 3.2 with the exception of the parametrization tools utilized. Economon [11] uses a built-in SU2 parametrization tool, which uses free-form deformation control points to characterize the surface of the cylinder. The free-form deformation control points are allowed to move freely in a given design space to produce new designs. As stated by Anand et al. [53], this method can produce more unconventional designs than the NURBS curves used in works such as those of Hilber et al. [8] or Bacellar et al. [9]. However, Anand et al. [53] also states that the FFD method is more prone to producing infeasible designs.

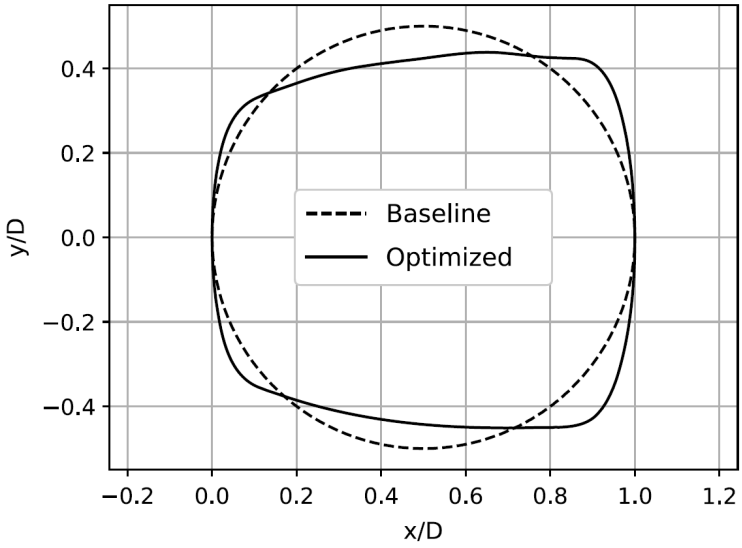

Figure 3.7: Comparison between the baseline and optimized geometry for a flow with heat transfer obtained by Economon [11].

The adjoint capabilities of SU2 have been used in other studies. For instance, Kucuk et al. [54] use the flow and adjoint solvers of SU2 to optimize the shape of an intake s-duct to minimise pressure losses. The parametrization, in this case, is also accomplished through the use of free-form deformation boxes.

Venkatesan-Crome et al. [55] use the SU2 adjoint solver to develop an optimization framework with a fully coupled FSI solver. Venkatesan-Crome et al. [55] apply this framework to the optimization of a NACA 0012 airfoil to increase its lift-to-drag ratio.

Overall, the capabilities of the adjoint solver of SU2 to optimize a design or to obtain the sensitivities of a shape with respect to an objective function are well established, as demonstrated by Economon et al. [11] and Albring et al. [50]. For this thesis, the SU2 adjoint solver was used to obtain the surface sensitivities. The optimization and surface deformation were executed outside SU2.

3.1.4. CAD PARAMETRIZATION

The surfaces of the tubes were parametrized using NURBS curves. This parametrization was achieved using the software tool ParaBlade described by Agromayor et al. [12]. A NURBS curve $C(u)$ is defined by the points P_n and the control polygon formed by these points. The position of the control points is determined based on the design variables used to define the surface (chord, thickness distribution, etc.). The curve $C(u)$ is tangent to the control polygon and can be obtained by interpolating its endpoints. The resulting curve C(u) is always situated inside the convex hull of the control polygon.

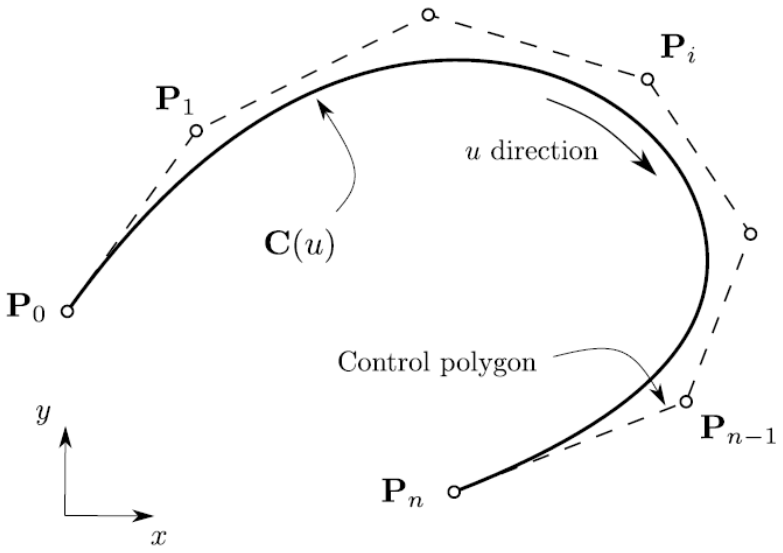

Figure 3.8: Definition of a NURBS curve C(u) from Agromayor et al. [12]

The parametric curve $C(u)$ can be computed using the basis functions $N_{i,p}$:

$$C(u) = \frac{\sum_{i=0}^{n} N_{i,p}(u) w_i P_i}{\sum_{i=0}^{n} N_{i,p}(u) w_i P_i} \tag{3.8}$$

Where $0 < u < 1$, P_i are the coordinates of the points, and w_i are the weights of n+1 control points. A more detailed description of the computation of C(u) was presented by Agromayor et al. [12], where the computation of the basis functions is explained in detail.

The NURBS curve parametrization has some significant advantages over the FFD approach. In this approach, the position of the control points P_i is determined by a set of geometrical characteristics such as chord, thickness distribution, and leading/trailing edge curvature. This means that the design space for NURBS is smaller than for FFD. However, as stated by Anand et al. [53], the optimal design obtained is always feasible if the appropriate geometric bounds are used. Another advantage of the NURBS curves approach is the ability to directly constrain the design variables and to have greater control over the design space.

The CAD parametrization tool ParaBlade was used to construct the blade surface starting from the baseline tube bundle geometry. ParaBlade uses a set of design parameters (thickness distribution, chord, etc.) and a set of interpolated coordinates to describe the tube surfaces in order to approximate the initial geometry as closely as possible. The parametrization of the surface is necessary in order to perform the surface deformation and for ParaBlade to calculate the surface sensitivities with respect to the design variables.

3.2. OPTIMIZATION FRAMEWORK

3.2.1. DESIGN CHAIN

The main steps of the optimization process are presented in the extended design structure matrix (XDSM) in Figure 3.9. The principal components of the optimization loop are the surface deformation tool, the mesh deformation algorithm, the flow solver and adjoint solver. The initialization involves only the surface and mesh parametrization. The optimization loop is implemented in the ParaBlade Python library.

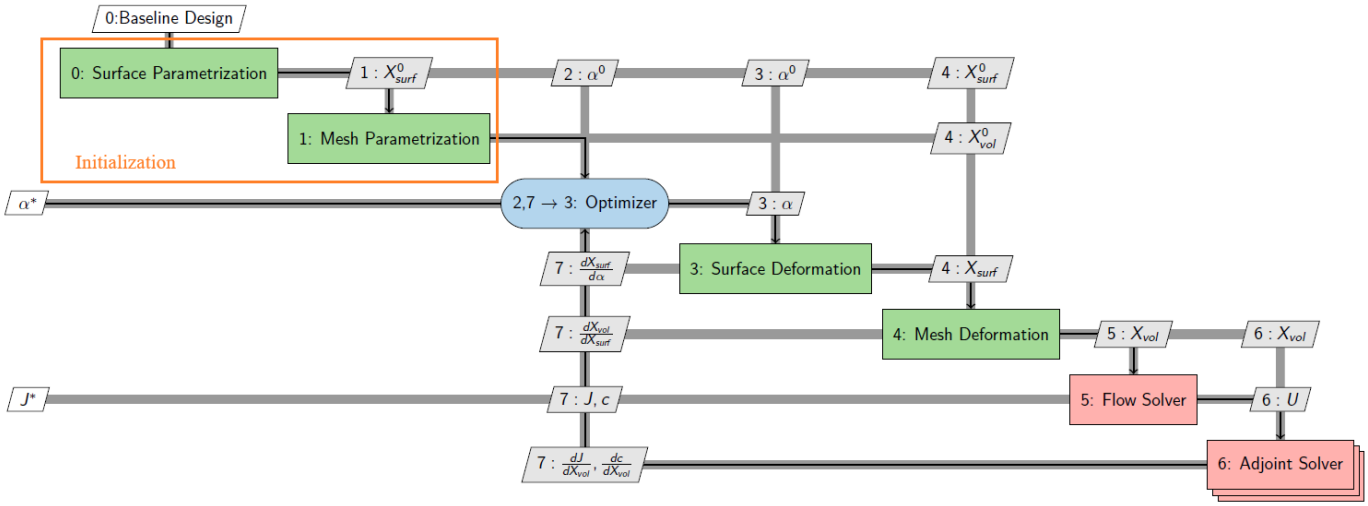

Figure 3.9: XDSM of the optimization framework

The initialization step involves taking the surfaces of the flow domain and parametrizing them using NURBS curves in ParaBlade. This constitutes the pre-processing part of the optimization process. The steps, inputs and outputs of the optimization loop are explained below:

- 0,1:inputs- α^0; X^0_{surf}; X^0_{vol} - design variables, surface and mesh respectivly of the baseline design.
- 2:Optimizer - either the SLSQP (from the SciPy library) or SNOPT (from the pyoptsparse library) can be used as optimization algorithms. This is where the new design vector is computed for each iteration.
- 3:Surface Deformation - ParaBlade deforms the tube surface and computes the surface sensitivity with respect to the design variables: $\frac{dX_{surf}}{d\alpha}$.
- 4:Mesh Deformation - SU2 _DEF performs the mesh deformation and computes the mesh sensitivity with respect to the surface deformation $\frac{dX_{vol}}{dX_{surf}}$.
- 5:Flow Solver - the RANS solver of SU2 (SU2 _CFD) .
- 6:Adjoint Solver - the discrete adjoint solver of SU2 (SU2 _CFD _AD)using reverse Algorithmic Differentiation to compute the derivatives of equation 3.7. Computes the sensitivities of the objective function and constraints with respect to the mesh coordinates: $\frac{dJ}{dX_{vol}}$ and $\frac{dc}{dX_{vol}}$.
- outputs: J^*; α^* - final evaluation of the objective function and the optimal design vector.

With the sequence of steps outlined in Figure 3.9, the sensitivity of the objective function with respect to the design variables can be written as the following matrix product:

$$\frac{\partial J}{\partial \alpha} = \frac{\partial J}{\partial X_{vol}} \cdot \frac{\partial X_{vol}}{\partial X_{surf}} \cdot \frac{\partial X_{surf}}{\partial \alpha} \tag{3.9}$$

Where the first 2 terms on the right-hand side of the equation represent the node/mesh sensitivity of the objective function, and the last term represents the CAD sensitivity computed by ParaBlade. The design chain starting from the design vector α and ending in the objective function J is displayed in Figure 3.10.

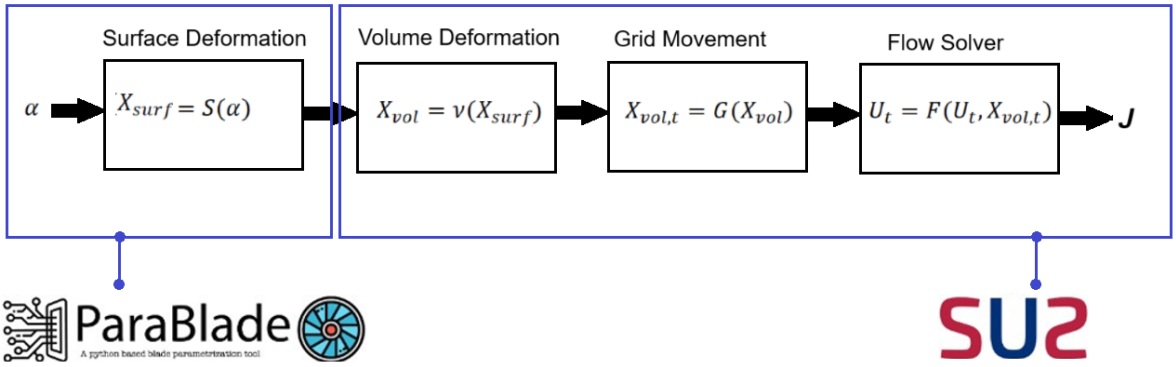

Figure 3.10: Design chain of the optimization process

3.2.2. OPTIMIZATION ALGORITHMS

The optimization algorithms available in the optimization framework are based on sequential quadratic programming (SQP). This type of iterative Quasi-Newton method is used to find a function's zeros or the minima/maxima. SQP methods solve constrained optimization problems with smooth non-linear objectives and constraint functions. This is accomplished by converting the constrained optimization problem into a set of quadratic programming subproblems. SQP can handle both inequality and equality constraints. SQP algorithms are suitable for use when the functions are smooth but may have some issues with discontinuous functions. A formulation of the SQP algorithm and its implementation is given by Kraft [56]. For a given function to minimize $f(x)$, the quadratic subproblems can be written as:

$$\min_x \frac{1}{2} d^T B d + \nabla f(x)^T d \tag{3.10}$$

where d is the search direction, and B is the Hessian matrix.

The equality and inequality constraints, $g(x)$ and $h(x)$, of this problem are written as:

$$g_j(x) + \nabla g_j(x)^T d = 0 \quad j = 1, ..., m_e \tag{3.11}$$

$$h_j(x) + \nabla h_j(x)^T d \geq 0 \quad j = m_e + 1, ..., m \tag{3.12}$$

where $1, ..., m_e$ are the equality constraints and $m_e + 1, ..., m$ are the inequality constraints.

The SLSQP (Sequential Least Squares Quadratic Programming) algorithm is presented by Schittkowski [57]. SLSQP replaces the quadratic subproblems with linear least squares problems. This can be accomplished by approximating the Hessian matrix B from equation 3.10 using an LDL decomposition. The resulting optimization least square problem has the form of:

$$\min_x \| D^{1/2} L^T d + D^{-1/2} L^{-1} \nabla f(x) \| \tag{3.13}$$

where L is a lower triangular matrix, and D is a diagonal matrix.

Schittkowski [57] finds some advantages of the least-square formulation over the standard SQP. The least-square approach is faster than standard SQP software and requires fewer gradient evaluations to converge. Schittkowski [57] also notes that some implementations of the least-square formulation are less sensitive to the starting point of the optimization than the standard SQP formulation. The SLSQP package used in the optimization framework is available in the SciPy library of Python.

SNOPT (Sparse Nonlinear Optimizer) is an implementation of the SQP algorithm, which uses a limited-memory quasi-Newton approximation for the B matrix. SNOPT implements the Hessian B and the Jacobian of constraints as sparse matrices. This algorithm is presented in the work of Gill et al. [58] and is available as part of the pyoptsparse Python library. SLSQP and SNOPT are the two available optimization algorithms in ParaBlade.

3.3. SHAPE OPTIMIZATION OF ROUND TUBES

This section presents the setup for an optimization test case using the optimization framework presented in Section 3.2. The test case is a cylindrical 7-tube array presented in Section 2.5. The flow conditions are the same as those presented in Section 2.5.2, and the mesh density is the same as for Grid 3 in Section 2.5.3.

Two optimizations are carried out on this flow domain using the SLSQP and SNOPT optimization algorithms. The optimal designs obtained by the two methods are presented in Section 3.4.

3.3.1. OBJECTIVE FUNCTION

The objective of the optimization is to minimize the airside pressure drop Δp while constraining the heat transfer rate ($\dot{Q}$) from the isothermal tube walls to the fluid. During the optimization process the tube shapes are changed by modifying the design surfaces, i.e. the thickness distribution. The tube's cross-section area (A) is constrained to remain constant or higher than the baseline tube cross section. Therefore, the optimization problem is formulated as:

$$\min_{\alpha} \quad \Delta p(\alpha), \tag{3.14}$$

$$s.t. \quad \dot{Q} \geq \dot{Q}_0, \tag{3.15}$$

$$A \geq A_0, \tag{3.16}$$

where $\dot{Q}_0$ and A_0 are the heat transfer rate and the cross-section, respectively, of the baseline tube design. The constraint on heat transfer rate is not directly imposed. Instead, the outlet temperature is constrained. The heat transfer rate through the tube bank can be computed as:

$$\dot{Q} = \dot{m} c_p \Delta T \tag{3.17}$$

where $\dot{m}$ is the mass flow rate, ΔT is the temperature change across the tube row and c_p is the specific heat transfer. Other than the ΔT, all other terms remain constant regardless of the final shape of the tubes. The mass flow rate and the inlet temperatures are determined by the pre-selected boundary conditions, and c_p is a constant fluid property. Therefore, the outlet temperature is constrained during the optimization process to keep ΔT constant. Equation 3.15 can be re-written as:

$$\Delta T \geq \Delta T_0 \tag{3.18}$$

where ΔT_0 is the temperature rise over the tube row for the baseline design.

Since this optimization is an iterative process, a relaxation factor must be applied to the sensitivity of the objective function to control the convergence and avoid stability issues of the optimization process. Through preliminary tests, a relaxation factor of $RF = 10^{-4}$ was found to perform best. Having a higher value of the relaxation factor, $RF = 10^{-2}$, was found to result in a faster convergence rate, but the final design was suboptimal with respect to that obtained with $RF = 10^{-4}$. A lower value of the relaxation factor, $RF = 10^{-6}$, leads to a slow convergence rate, which could lead to the maximum allowed run-time before an optimum is found.

3.3.2. DESIGN VARIABLES AND GEOMETRIC CONSTRAINTS

The design variables of this shape optimization are the thickness distribution along the tube chord. The thickness distribution of the round tube is displayed in Figure 3.11 starting from T_1^u and ending at T_7^l on the upper surface of the tube, and from T_1^l to T_7^l for the lower surface. This thickness distribution is interpolated to obtain 9 control points that define the control polygon of the parametrized tube, as displayed in Figure 3.12. In total, the round tube is parametrized using 2 NURBS curves, one for the upper and one for the lower surface. Since the design variables are only the thickness distributions on the upper and lower sides of the tube, the chord of the tube is maintained constant. This means that the leading edge (L.E.) and trailing edge (T.E.) positions are fixed. The positions of the control points $[P_i^l; P_i^u]$ changed during the optimization according to the changes in the thickness distribution $[T_i^l; T_i^u]$.

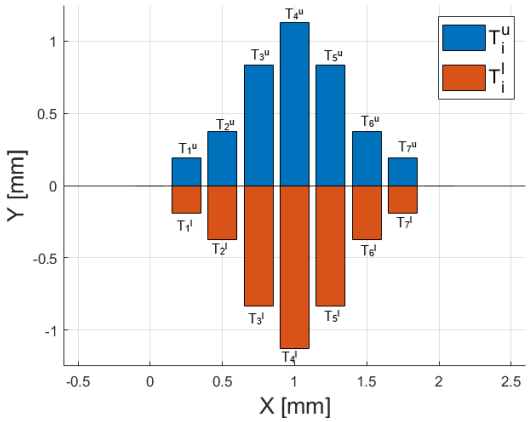

Figure 3.11: Thickness distribution parametrization for a round tube

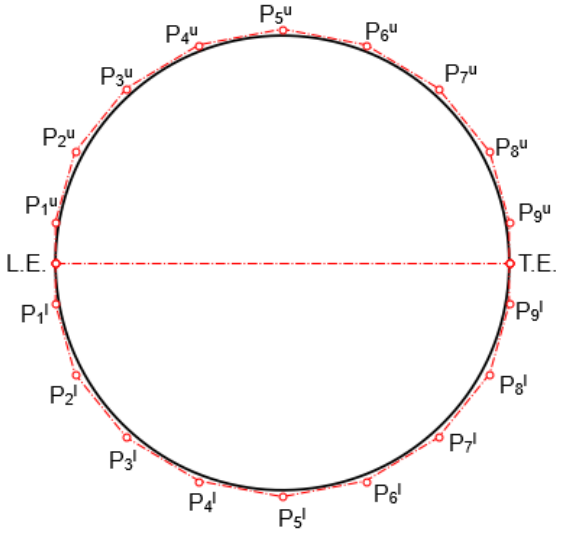

Figure 3.12: Position of the control points and control polygon that define the tube surface

After selecting the design variables that define the tube's surface, some additional geometric constraints were added. First, the 7 tubes are kept identical to each other. Without this constraint, the optimizer would produce a distinct shape for each tube. Second, the geometric constraint from equation 3.16 needs to be defined. This constraint is placed to keep the cross-sectional area of the tube above $A_0 = 3.14159 \cdot 10^{-6} m^2$, which is the cross-sectional area of the baseline, $A_0 = 3.14159 \cdot 10^{-6} m^2$. As an alternative, the hydraulic diameter of the tubes should be kept constant and calculated according to eq. 3.19:

$$D_h = \frac{4A}{P} \tag{3.19}$$

where P is the perimeter. However, the objective function is to minimize the pressure drop. This means the optimizer is unlikely to increase the perimeter of the tube significantly. A larger tube perimeter, in this case, would mean an additional wetted area for the tube and, therefore, more friction losses. An increase in the tube perimeter is also associated with a slight increase in cross-sectional area. This means that the hydraulic diameter would be largely constant just by applying the cross-sectional area constraint. This ensures, to a first approximation, that the flow conditions inside the tubes are unaffected by the optimization, thus guaranteeing that the heat transfer resistance does not increase on that side of the HEX.

The last geometric constraint concerns maintaining the tubes symmetrical. This means the thickness distribution on the upper side is mirrored on the lower side:

$$T_i^l = T_i^u \tag{3.20}$$

:

Figure 3.13 shows the design space for the thickness distributions T_i^l and T_i^u. The thickness parameters are allowed to move inside the design space described by the blue and red dashed lines for the SLSQP and SNOPT optimizations, respectively. The design bounds of the design variables are:

$$10^{-5} m \leq T_i^l; T_i^u \leq 1.7 \cdot 10^{-3} m \quad \text{for SLSQP} \tag{3.21}$$

$$10^{-5} m \leq T_i^l; T_i^u \leq 1.5 \cdot 10^{-3} m \quad \text{for SNOPT} \tag{3.22}$$

The design space for the SNOPT optimizations is smaller than that for the SLSQP optimization. Unfortunately, using the same wider design bounds for SNOPT would result in design surfaces with highly deformed meshes. These meshes, in turn, cause the CFD simulations to diverge and prematurely stop the optimization before an optimum can be reached.

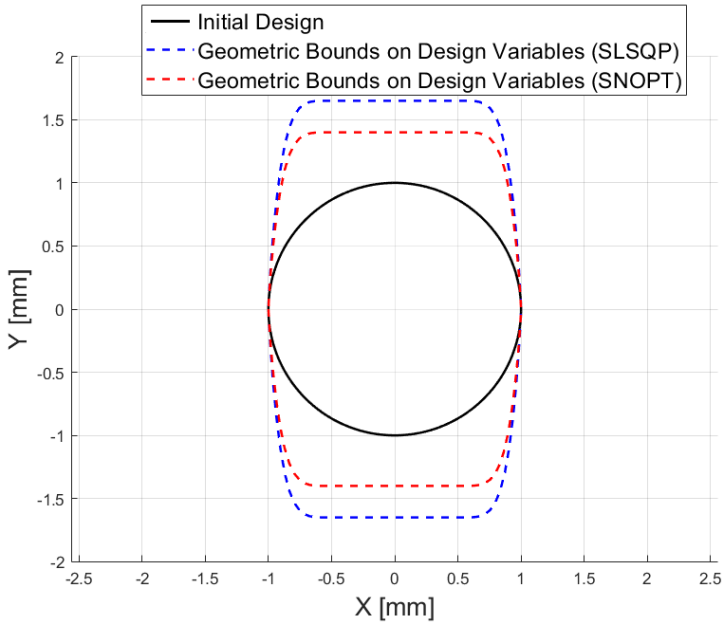

Figure 3.13: Geometric bounds of the design space for the SLSQP and SNOPT optimizations.

3.3.3. GRADIENT VERIFICATION

The gradient verification process involves comparing the gradients of the objective function with respect to the design variables computed with the adjoint method to those computed with the finite difference method. The finite difference method works by perturbing each design variable and running a CFD computation to assess the objective function. This means that for 98 design variables, the finite difference method would need 98 CFD computations to assess the necessary gradients corresponding to all variables. This is obviously much more computationally expensive than the adjoint method, which only requires 2 computations to assess the gradients. This illustrates quite well the advantage of the adjoint method in the context of shape optimizations with large design vectors.

Only the gradients of the design variables on the lower side of the first tube, $[T_1^l;...;T_7^l]$, were computed using the finite difference method. This was done due to the high computational cost of the finite difference method. Computing a CFD evaluation for all 98 design variables would have taken too much time. The results are displayed in Figure 3.14, where the finite difference gradients for the pressure drop are compared to the gradient obtained using the adjoint method. Ideally, all the points in the Figure 3.14 would lie near the diagonal line $x = y$. However, there is significant disagreement between finite difference and the adjoint gradient computations. The finite difference step selected to compute the finite difference gradients is $\Delta h = 5\%$ of the initial values of the design variables. The accuracy of the finite difference gradients is highly dependent on the value of Δh. For lower values of Δh, such as 1%, the gradients for the design variables near the L.E. and T.E. compute values closer to those computed with the adjoint methods. In contrast, the gradients of the design variables near the middle of the tube give better results for higher values such as $\Delta h = 10\%$. A comparison for the finite difference gradients computed with $\Delta h = [1\%; 5\%; 10\%]$ can be found in annexe B.4. Regardless, there are still some differences in the computation of the gradients using the adjoint and finite difference methods.

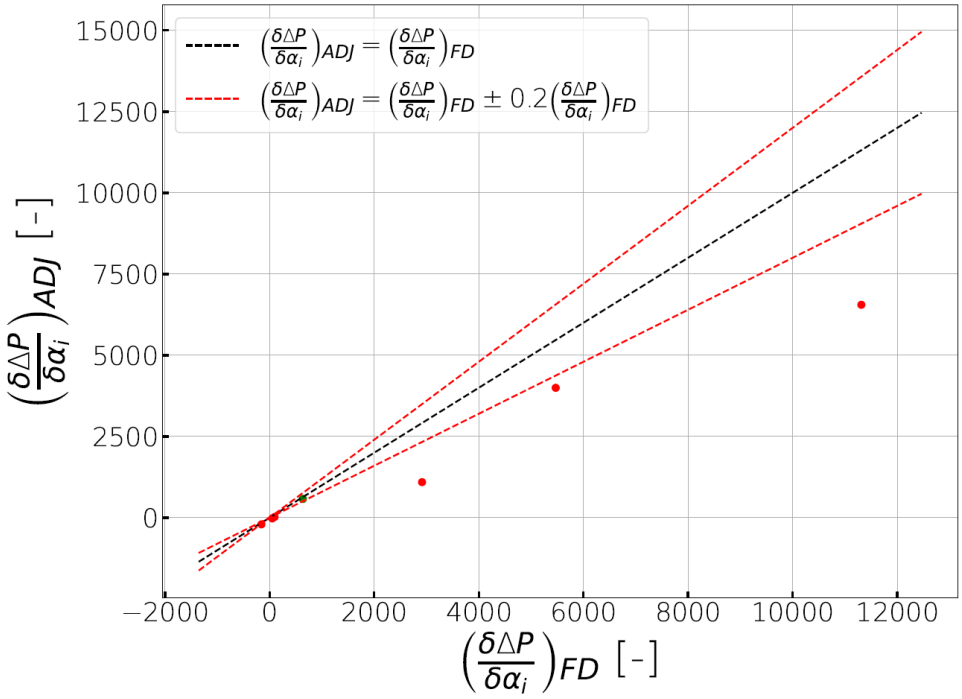

Figure 3.14: Finite difference gradients for pressure drop as a function of the design variables as a function of the adjoint gradient.

3.3.4. OPTIMIZATION SET-UP

The optimization setup for the SLSQP and SNOPT optimizations of the 7 cylindrical tube domain is summarized below:

- 7 identical tubes each defined by 2 design surfaces.
- design surfaces parameterized using NURBS curves
- 98 design variables for the thickness distribution: $\alpha = [T_i^l; T_i^u] \quad i = 1...49$
- Symmetric tube geometry
- Design space for SLSQP: $10^{-5}m \leq T_i^l; T_i^u \leq 1.7 \cdot 10^{-3}m$
- Design space for SNOPT: $10^{-5}m \leq T_i^l; T_i^u \leq 1.5 \cdot 10^{-3}m$
- Area constraint: $A \geq 3.14159mm^2$
- Temperature constraint: $\Delta T \geq 22.5$ K
- Baseline Pressure Drop: $\Delta p_0 = 44.8$ Pa
- Objective function: $\min_\alpha \Delta p$
- Objective function relaxation factor: $RF = 10^{-4}$
- Turbulence model for CFD computations: $k-\omega$ SST
- Discrete Adjoint Method

The temperature constraint presented here is the ΔT computed using the $k-\omega$ SST model since this is the best turbulence model available in SU2. This means that the ΔT computed by the Realizable $k-\epsilon$ model could be lower for the final design than that of the baseline. The temperature constraint is, however, considered satisfied for the Realizable $k-\epsilon$ if $\Delta T \geq 0.95 \cdot \Delta T_0$, where $\Delta T_0 = 33.49$.

3.3.5. POST-PROCESSING

Throughout the optimization process, the mesh (X_{vol}) of the computational domain needs to be modified to accommodate the changes in the surface of the tubes. If the optimized design differs greatly from the baseline design, the resulting mesh can be highly distorted, especially in the region of the inflation layers close to the tube walls. Figure 3.15 shows what a deformed mesh produced could look like (for a comparison with the mesh of the baseline design, see Figure 2.19). This mesh corresponds to a tube geometry produced by the optimization process using the SLSQP algorithm. This mesh clearly shows regions in the inflation layer where grid elements are no longer orthogonal, especially near the corners of the tube. The mesh density in the unstructured region is also no longer uniform. This type of mesh is inadequate for properly computing the flow field near the tube walls. This means that this mesh can induce errors when calculating the pressure drop and the outlet temperature. Although the computations on the mesh in Figure 3.15 show a good convergence history, displayed in Figure 3.17, there can still be some errors in the outputs of the CFD simulation due to the poor quality of the mesh.

Therefore, for the reasons outlined above, it is necessary to re-mesh the surfaces obtained from the optimization process and re-compute the flow field to increase the accuracy of the results. Figure 3.16 displays the same surface obtained from the optimization of round tubes but with a recomputed mesh using the same parameters of Grid 3 described in Section 2.5.3. The overall difference in results obtained for the two grids is given in table 3.1. The difference in ΔT computed with the two meshes is 1.86%, and the difference in pressure drop is 4.01%. Both results presented in table 3.1 are computed using $k-\omega$ SST. The difference in ΔP is quite significant and shows why re-meshing and then repeating the CFD simulation is important for the estimation of the actual optimized design performance. In the following sections, all the reported optimization outputs are given for the re-generated mesh.

Once the optimal geometry obtained from the optimization process has been re-meshed, the high-fidelity solver can be used to re-compute the flowfield. In chapter 2, it was shown that Realizable $k-\epsilon$ provides more accurate results than $k-\omega$ SST.

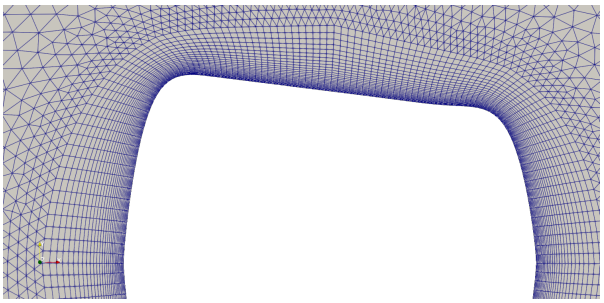

Figure 3.15: Mesh produced by the optimizer for the optimized tube design

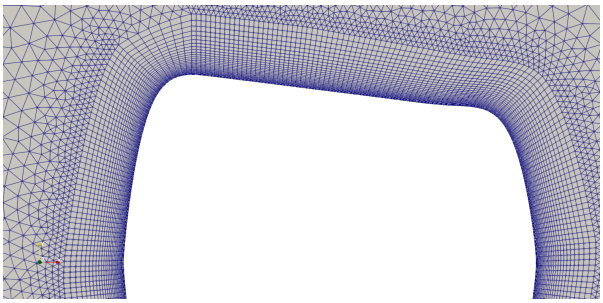

Figure 3.16: Regenerated mesh for the optimized tube design

Grid	Δp [Pa]	ΔT [K]	Δp_{diff}[%]	ΔT_{diff}[%]
Grid 3.15	37.63	22.51	-	-
Grid 3.16	39.14	22.93	4.01	1.86

Table 3.1: Difference in the overall results computed with $k-\omega$ SST for the (SLSQP) optimized design of round tubes using grids in Figures 3.15 and 3.16.

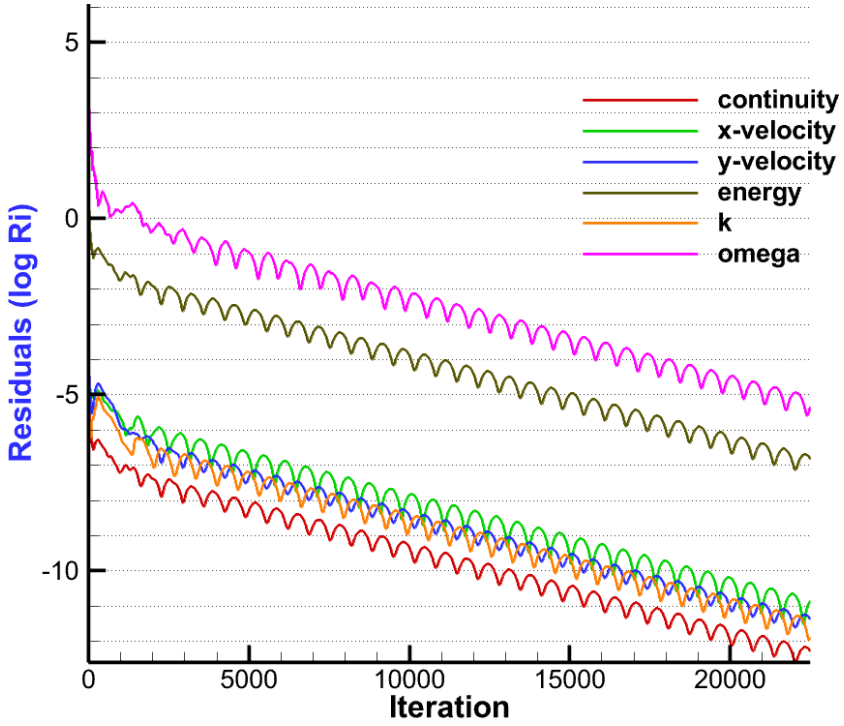

Figure 3.17: Convergence History of the $k-\omega$ SST simulation for the grid presented in Figure 3.15

3.4. RESULTS

The results of the two optimizations are presented in table 3.2, where the overall performances of the optimal tube designs are reported and compared to the baseline design. Table 3.2 presents the results obtained with the Realizable $k-\epsilon$ model after the optimal geometries have been re-meshed.

The resulting designs show that SLSQP performs better in minimizing the pressure drop than SNOPT. The former achieves a 22.3% reduction in Δp, whereas the latter can only achieve a 7.9% reduction. SLSQP also performs better in terms of computational efficiency, needing only 51 objective function evaluations to find an optimal shape, whereas SNOPT needs at least 60 evaluations. The better performance of SLSQP can, in part, be attributed to the use of wider design bounds than for SNOPT. This was necessary for the reasons outlined in Section 3.3.2.

The main issue of the SLSQP final design is the reduction in temperature rise over the tube bank. The SLSQP optimization results in a design with a reduction of ΔT by 4.8%, whereas the SNOPT final design only shows a 1.73% reduction when Realizable $k-\epsilon$ is used to compute the flow fields. The results obtained for the SLSQP tube design with the SST model satisfy the temperature constraint within 0.4% of initial ΔT. Therefore, this reduction in ΔT is due to the turbulence model used in the optimization process and the one used during the post-processing stage.

Figure 3.18 shows a comparison of the flowfields of the baseline and the two optimized designs assessed with the Realizable $k-\epsilon$ model. Even from this image, it is clear that the SLSQP optimization changes the baseline shape much more significantly than the SNOPT optimization. The tube shape towards the trailing edge is more streamlined in the SLSQP final design, thus explaining the reduction in pressure drop across the tube row. Figure 3.19 shows the flowfields computed with the SST model.

Tube Design	Δp [Pa]	ΔT [K]	Change in Δp [%]	Change in ΔT [%]	CFD Evaluations
Baseline	62.55	33.49	-	-	1
Optimal Design-SNOPT	57.6	32.91	-7.91	-1.73	60
Optimal Design-SLSQP	48.59	31.88	-22.31	-4.8	51

Table 3.2: Overall performance of the optimized tube shapes compared to the baseline tube design obtained with the realizable $k-\epsilon$ model for the re-meshed surface.

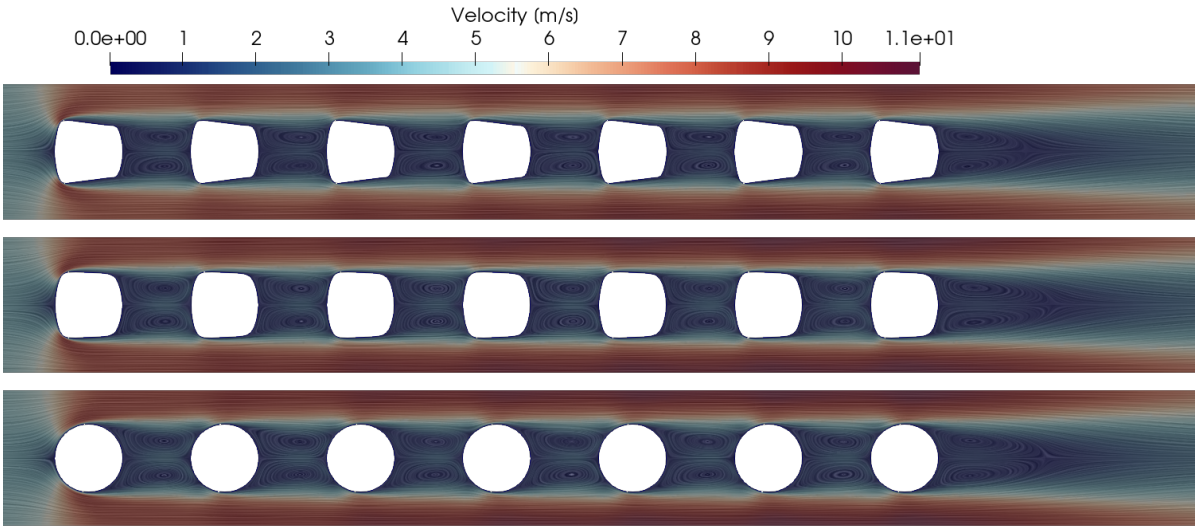

Figure 3.18: Flowfields of the optimized designs using SLSQP (top) and SNOPT (middle) compared to the baseline tube design (bottom) obtained with the Realizable $k-\epsilon$ model

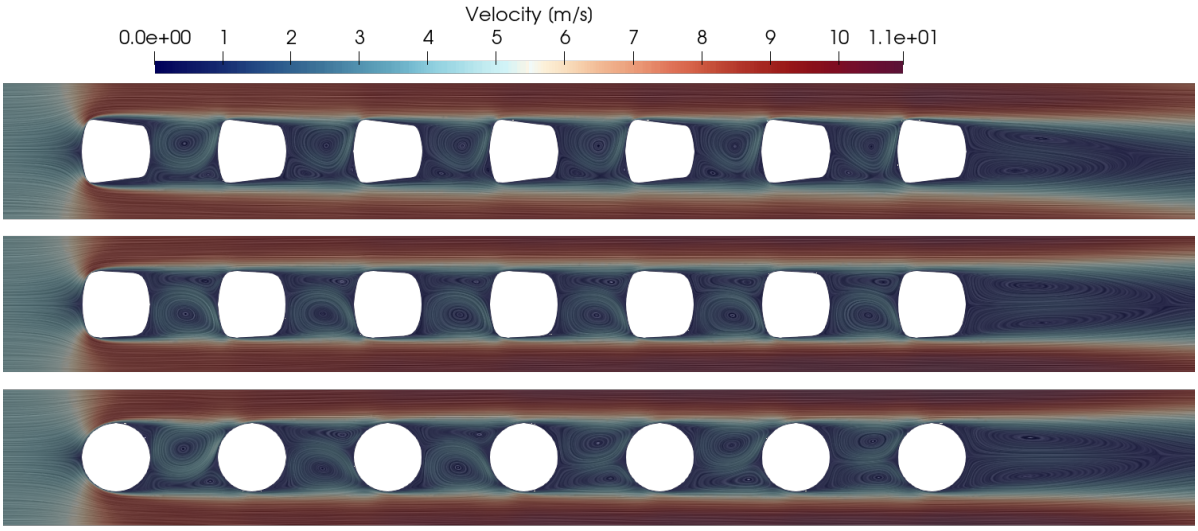

Figure 3.19: Flowfields of the optimized designs using SLSQP (top) and SNOPT (middle) compared to the baseline tube design (bottom) obtained with the $k-\omega$ SST model

3.4.1. OPTIMIZATION RESULTS WITH SLSQP

The final shape of the SLSQP optimization is compared to the baseline design in Figure 3.20. The chord length was intentionally kept constant to maintain the characteristic length constant. This ensures that the Re and flow conditions remain the same for both tube shapes. The resulting optimized shape has a small curvature at the leading edge and trailing edge (blunt L.E and T.E), which makes the front and back sides of the tube almost vertical surfaces. The tube has a trapezoidal shape with round corners and tapered sides from the leading to the trailing edge. The optimized tube has a slightly larger cross-section area than the baseline design. The optimized shape has an area larger by 1.5% than the baseline tube.

The reduction in pressure drop is accomplished by delaying the reattachment of the flow on the downstream tubes and also by moving the high velocity flow region away from the tube walls. The delayed reattachment of the flow is caused by the almost vertical frontal tube surface, and this contributes to the reduction of skin friction drag on the tube walls. Due to the tapered sides of the tubes, the freestream velocity flow region is located further away from the tube walls, thus further decreasing the skin friction drag of the tube. Furthermore, the flow separation is also delayed. This contributes to the reduction of the form drag. All of

these factors contribute to a reduction in the total drag and thus to a reduction of the overall pressure drop of the tube bank. Figure 3.21 present the flowfield around the 6th Tube of the optimized array computed with the Realizable model. This figure displays the increasing velocity boundary layer thickness and clearly shows that most of the freestream velocity region is situated far away from the tube walls.

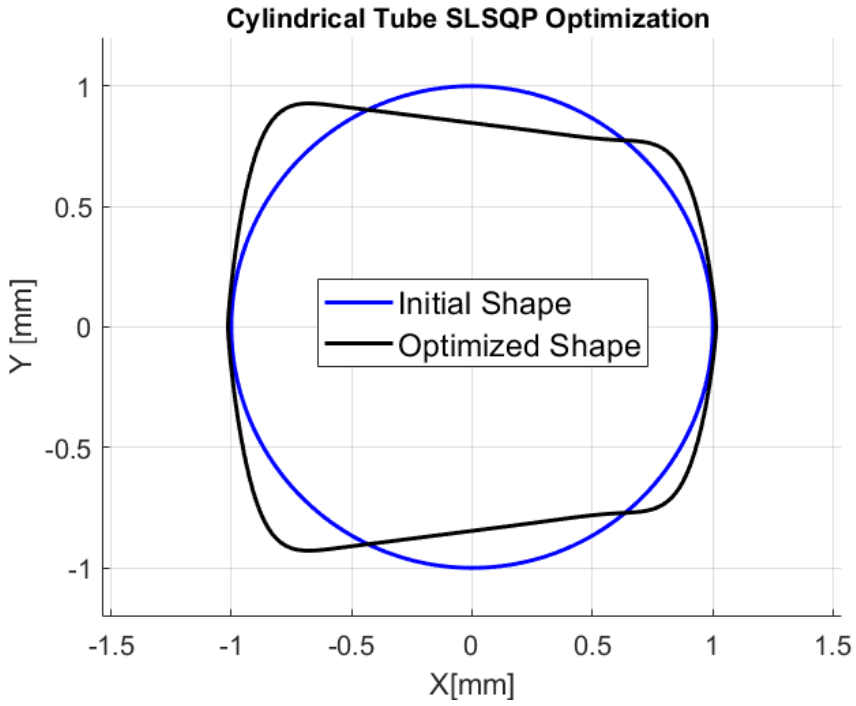

Figure 3.20: Comparison between the initial and optimized shapes for the cylindrical tube case for the SLSQP optimization

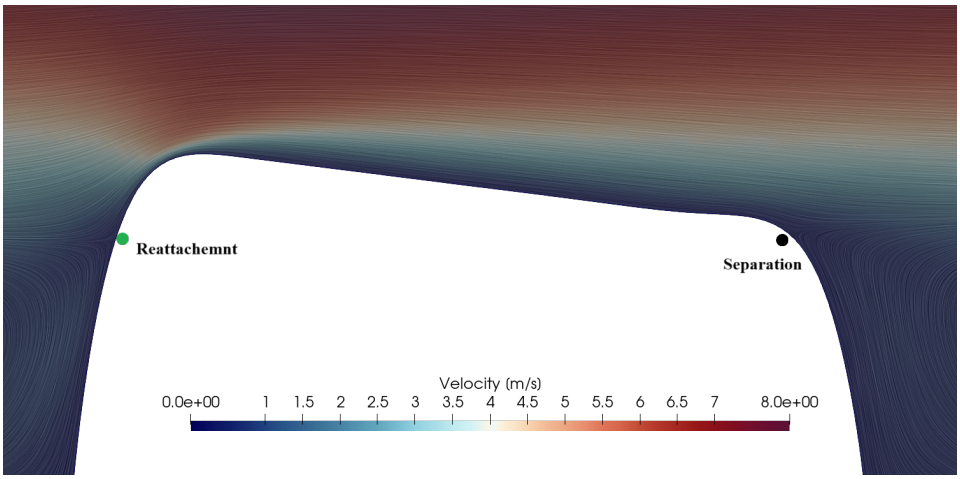

Figure 3.21: Flowfield near the 6th tube of the SLSQP optimized design computed with Realizable $k-\epsilon$

3.4.2. OPTIMIZATION RESULTS WITH SNOPT

The final shape of the SNOPT optimization is compared to the baseline design in Figure 3.22. The same observations made for Figure 3.20 apply in this case. The main difference between the optimal geometries lies in the top and bottom surface of the tubes. The optimal design found by SNOPT has a less tapered shape than that identified through the SLSQP algorithm. The SNOPT design also has a larger cross-section area than the baseline design. This is 9% larger than the baseline.

In this case, since the tube taper is milder, the freestream velocity flow is much closer to the tube surface than in the SLSQP tube design. As can be seen from Figure 3.23, the boundary layer is less thick than for the SLSQP design and thus the losses due to skin friction are higher. The pressure drop is still lower for the SNOPT design than for the round tube, for the same reasons outlined in section 3.4.1, but to a lesser degree than for the previous design.

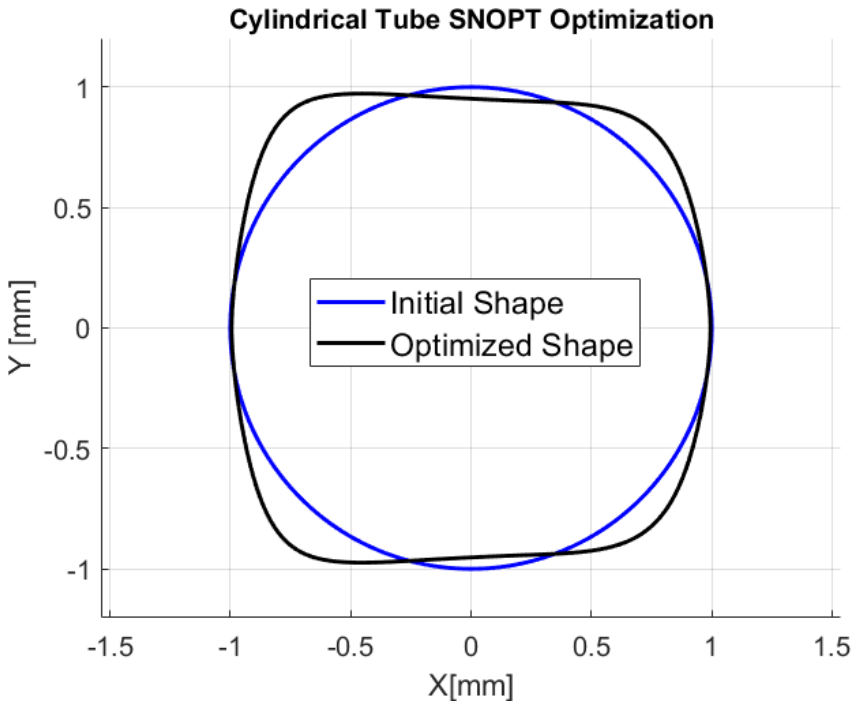

Figure 3.22: Comparison between the initial and optimized shapes for the cylindrical tube case for the SNOPT optimization

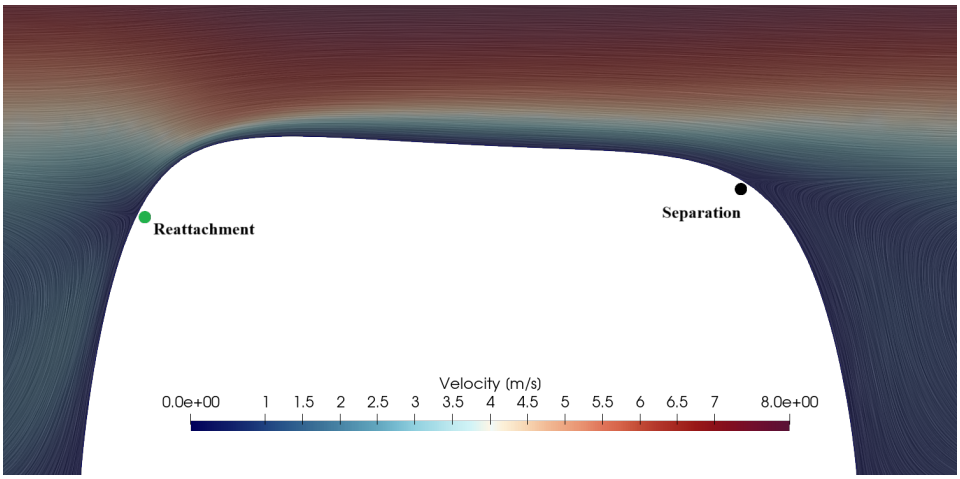

Figure 3.23: Flowfield near the 6th tube of the SNOPT optimized design computed with Realizable $k-\epsilon$

3.4.3. TURBULENCE MODEL COMPARISON

Since no experimental or correlation data for the optimized design is available, it is difficult to assess which turbulence model computes the overall results for the final tube shapes more accurately. Chapter 2 showed that Realizable $k-\epsilon$ demonstrates a better accuracy for round tubes when compared to the empirical correlations. Bacellar et al. [9] and El Gharbi et al. [48] use $k-\epsilon$ based models to simulate flows over non-cylindrical

tubes. However, without experimental data, it is impossible to state which turbulence model is better. For this reason, simulations with higher fidelity models are needed.

The results presented in Table 3.2 report only the performance of the tube bank computed with the Realizable $k-\epsilon$ model. However, the final designs shown in Figures 3.20 and 3.22 were obtained by an optimization framework that uses $k-\omega$ SST as a turbulence model.

Tables 3.3 and 3.4 compare the baseline and the optimized design's overall performance computed with the SST and Realizable turbulence models. Table 3.3 shows the SLSQP optimized design results, whereas Table 3.4 shows the same for the SNOPT optimized design. Both tables show a similar trend in the results. The improvement in pressure drop estimated by the simulation with the Realizable model is larger than that obtained with the SST model. Also, for both optimal designs, the simulation with the SST model predicts an increase in ΔT while a reduction is obtained when the Realizable model is applied.

As shown in Figures 3.21 and 3.24, the flowfields predicted with the two turbulence models for the SLSQP optimized designs are relatively similar to each other. The location of the flow reattachment predicted by SST and Realizable is similar for the optimized tube. The same is true for the flow separation point, whereas, in the case of the baseline design, this location would differ significantly depending on the turbulence model. As stated earlier, the highly tapered surface of the tube favours the thickening of the boundary layer and delaying flow separation, and this is able to be modelled by both SST and Realizable $k-\epsilon$. This leads to both models making predictions for the overall pressure drop much closer to each other. For the baseline round tube, the value computed for ΔP with the SST model was 28.4% lower than that computed with Realizable $k-\epsilon$. For the SLSQP optimized design, the value computed for ΔP with the SST model was 19.4% lower than that computed with Realizable $k-\epsilon$. The same conclusion applies to the SNOPT design but to a lesser extent due to the milder side taper, which means that the region of freestream velocity flow is closer to the tubes compared to the SLSQP design. Therefore, more of the tube surfaces is surrounded by high velocity flows which results in higher friction drag and a higher pressure drop.

The decrease in the outlet temperature predicted by the simulation with the Realizable $k-\epsilon$ model for the optimized designs is due to the reduced mixing in the airflow. For the optimized designs, more fluid flows in the free-stream region where the temperature is lower. Because the increasing velocity boundary layer thickness over the tube surface, and the freestream velocity region is further away from the wall, less fluid is directed where temperatures are higher. This leads to less heat being transferred to the fluid and less mixing occurring in the tube wake. This reduction in mixing compared to the baseline design is correlated to a reduction in the turbulent kinetic energy for the optimized designs, which can be seen in Figure 3.26. This is not detected with the SST model, as most of the mixing occurs, according to the simulation with this model, only after the last tube of the BTHX. The CFD simulations with the $k-\omega$ SST model, therefore, predicts a similar temperature increase for the optimized and baseline designs. This is particularly true for the simulation with the deformed mesh. In this case, the outlet temperature is within 0.4% of that of the baseline.

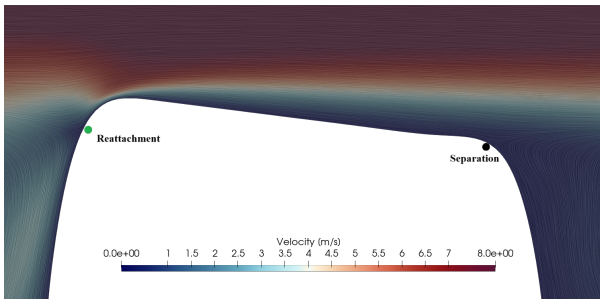

Figure 3.24: Flowfield near the 6th tube of the SLSQP optimized design computed with the CFD model adopting $k-\omega$ SST

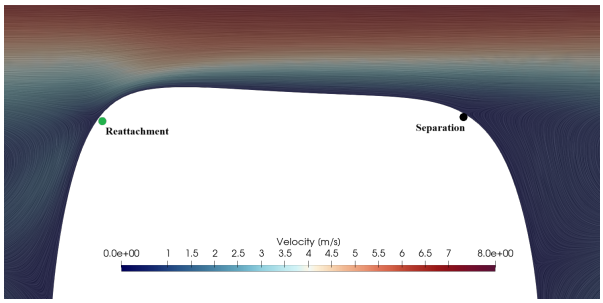

Figure 3.25: Flowfield near the 6th Tube of the SNOPT optimized design computed with the CFD model adopting $k-\omega$ SST

Test Case-Turbulence Model	Δp [Pa]	ΔT [K]	Change in Δp [%]	Change in ΔT [%]
Baseline-SST	44.8	22.65	-	-
Optimal Design-SST	39.14	22.93	-12.63	1.23
Baseline-Realizable $k-\epsilon$	62.55	33.49	-	-
Optimal Design-Realizable $k-\epsilon$	48.59	31.88	-22.33	-4.8

Table 3.3: Comparison of the overall performances obtained for the SLSQP optimized design. The results reported for the optimal design were obtained after re-meshing.

Tube Design-Turbulence Model	Δp [Pa]	ΔT [K]	Change in Δp [%]	Change in ΔT [%]
Baseline-SST	44.8	22.65	-	-
Optimal Design-SST	43.15	23.15	-3.68	2.2
Baseline-Realizable $k-\epsilon$	62.55	33.49	-	-
Optimal Design-Realizable $k-\epsilon$	57.6	32.91	-7.91	-1.73

Table 3.4: Comparison of the overall performances obtained for the SNOPT optimized design. The results reported for the optimal design were obtained after re-meshing.

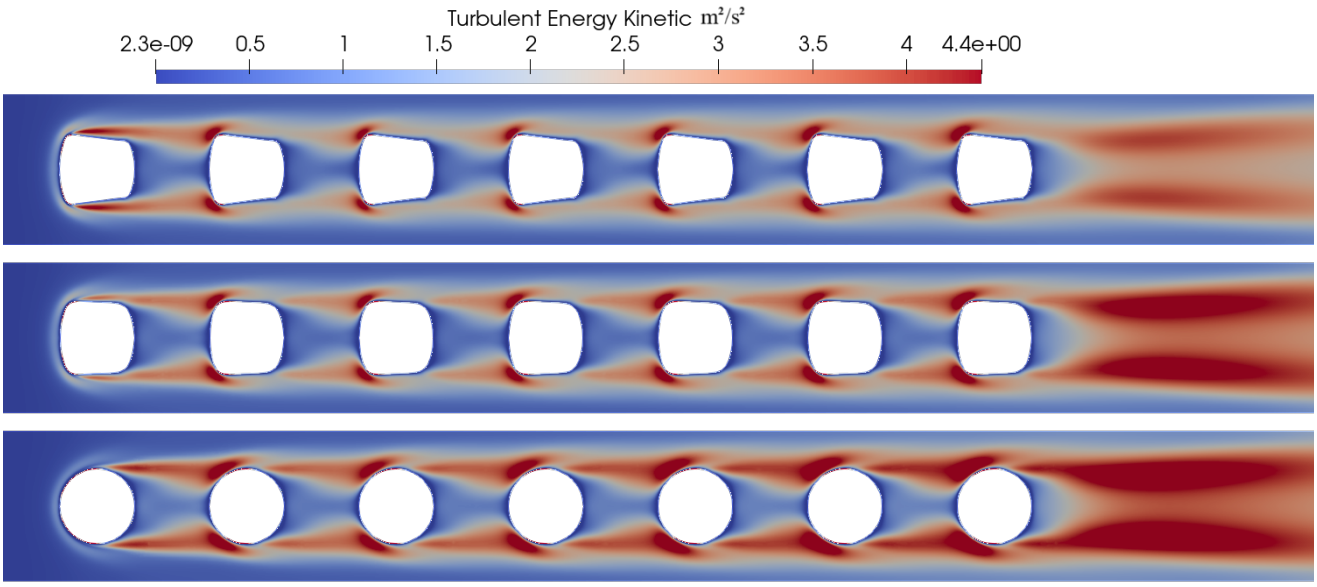

Figure 3.26: Turbulent kinetic energy contours for SLSQP design (top), SNOPT design (middle) and the baseline (top).

3.5. SUMMARY

This chapter presented the results obtained by applying the optimization framework presented in Section 3.2 to the design of round tube bundles. The results show that the SLSQP algorithm can provide better tube designs than SNOPT in terms of pressure drop minimization. However, SNOPT performed better in satisfying the temperature constraint imposed in the optimization. The difference in performance between the two optimizers can be partly attributed to the different design bounds. Using wider design bounds for SNOPT could not be adopted due to convergence issues.

Two main challenges were identified in the optimization study. First, the mesh of the final design produced by the optimization process can display some highly skewed grid elements and a non-uniform mesh density. This can lead to some errors in the computation of the flowfield and the overall performance, as shown in table 3.1. For this reason, it is necessary to re-mesh the resulting optimized surfaces. Second, the CFD evaluations in the optimization framework are performed with SU2, where only Spalart-Allmaras and SST are available as turbulence models. While the latter is the more accurate of the two, it is still less accurate than a turbulence model such as Realizable $k-\epsilon$ when it comes to the simulation of flows through BTHX

with round tubes at $Re \approx 1000$. Thus, the optimal geometry was reassessed with a simulation in Fluent with Realizable $k-\epsilon$ for a better understanding of the performance.

4

Numerical Modelling and Shape Optimization of Elliptical Tube Banks

This chapter covers the numerical modelling and optimization of tube banks with elliptical tubes. Two elliptical tube bank cases are presented in Section 4.2. The hydraulic diameter of the elliptical tubes, and the mass flow rate through the BTHX array is the same as that of the test case analyzed in the previous chapter. The difference between the two elliptical tube cases is that in the first one the relative pitches are the same as the round tube array, namely $P_T = P_L = 2$, while the second one considers absolute pitches $S_T = S_L$ of $4mm$. The CFD model is described in Section 4.3, and the predicted pressure drop and heat transfer are compared to those of the round tube array. Finally, Section 4.4 covers the shape optimization of the elliptical tubes using the same framework presented in Chapter 3.

4.1. Non-Cylindrical Tube Banks

Compared to cylindrical tubes, the availability of experimental or numerical studies for non-cylindrical tubes is limited. Merker et al. [13] is one of the few experimental works on non-cylindrical tubes which presents empirical correlations for pressure drop. This study derives empirical correlations for a staggered array of oval tubes comprising six tubes in the transverse direction and 8 tubes in the longitudinal direction. This array is presented in Figure 4.1. The resulting empirical correlations for pressure drop over a wide range of $Re \in [2 \cdot 10^3; 10^5]$ and at different pitch ratios are plotted in Figure 4.2. The main takeaway from the work of Merker et al. [13] is that pressure drop increases with a decreasing transverse pitch ratio in a staggered oval tube array.

Regarding numerical studies, the most comprehensive study was carried out by Bacellar et al. [9] that was already presented in chapter 3. Besides the optimizations, numerical simulations were carried out in this study on a wide variety of shapes presented in Figure 3.3. The main conclusion of Bacellar et al. [9] regarding the performance of various tube shapes is that the blunt symmetrical tubes (round and elliptic) have better thermal performance but perform worse in terms of friction.

Mangrulkar et al. [33] assessed the performances of both round and elliptical tubes using numerical and experimental methods. This study analyses the performance of 4x4 in-line tube arrays for round and elliptical tubes of different aspect ratios at a range of flow conditions of $Re \in [5 \cdot 10^3; 2.1 \cdot 10^4]$. Mangrulkar et al. [33] find that elliptical tubes perform better than round tubes in reducing the friction factor. Also, a smaller tube aspect ratio results in a further reduction in the friction factor. When it comes to the heat transfer and the Nusselt number, Mangrulkar et al. [33] determined that the performance of the round and elliptical tubes depends on the flow conditions. For $Re \leq 10000$, there is no significant difference in the average Nusselt number of the different tube shapes. For flow conditions at higher Re, round tubes display a larger Nusselt number than the elliptical ones. In this regard, elliptical tubes with higher aspect ratios also result in higher average Nusselt numbers. Mangrulkar et al. [33] together with the findings of Matos et al. [46] indicate that different tube shapes provide better heat transfer characteristics at different Reynolds numbers. Matos et al. [46] show that

for flows found in the laminar range, elliptical tubes provide better heat transfer characteristics. In contrast, Mangrulkar et al. [33] indicate that at large Re, round tubes perform better with respect to heat transfer.

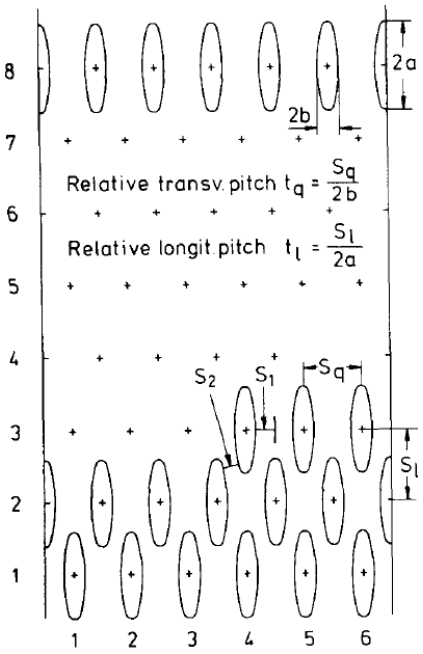

Figure 4.1: Staggered oval-tube array used by Merker et al. [13]

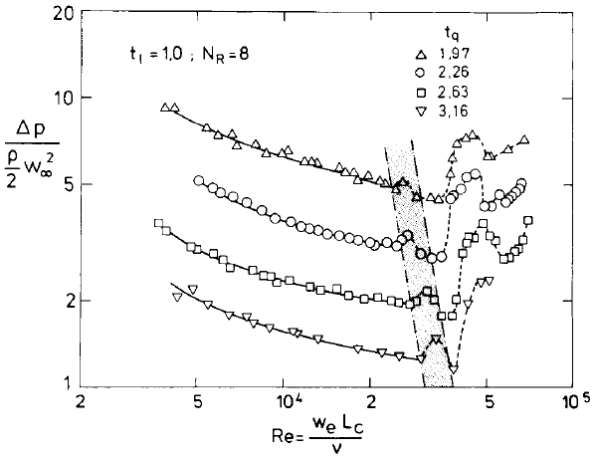

Figure 4.2: Experimental data for pressure drop for the staggered oval-tube array used by Merker et al. [13]

4.2. FLOW DOMAIN FOR ELLIPTICAL TUBE BANKS

The better performance of elliptical tubes regarding friction factor and pressure drop has been reported by other studies, such as Mohanty et al. [59]. Therefore, improvements in pressure drop can be accomplished by substituting round tubes with elliptical tubes and carrying out shape optimizations on a different initial tube shape. To show this, two elliptical tube cases were constructed starting from the 7 in-line round tube cases presented in chapter 2. The elliptical tube has the same hydraulic diameter as the initial round tube. In one elliptical tube arrangement the same relative pitch ratio of $P_L = P_T = 2$ is preserved (Case A), while the other one preserves the absolute pitch ratio of $S_L = S_T = 4mm$ (Case B). Due to the changes in the tube's chord, the flow conditions differ from the initial $Re \approx 1000$, but the mass flow rate is maintained in both cases as for the initial round tube case. The geometries of the 2 elliptical cases are presented and compared to the initial round tube case in Figure 4.3.

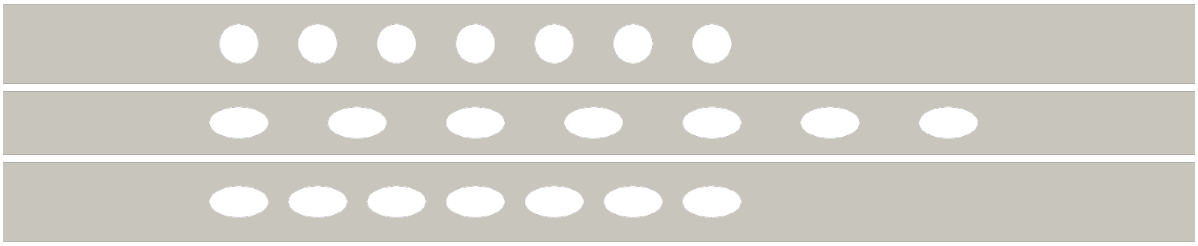

Figure 4.3: 7 in-line tube arrays: round tubes (top), elliptical tubes $P_L = P_T = 2$ (middle) and elliptical tube $P_L = 1.33$ $P_T = 2.5$ (bottom).

4.2.1. ELLIPTICAL TUBE SHAPE

The elliptical tube is meant to replace round tubes of $D = 2mm$. To not affect the flow inside the tubes, the elliptical ones must have the same hydraulic diameter of the baseline tube bundle. The definition of the hydraulic diameter reads:

$$D_H = \frac{4A}{P} \tag{4.1}$$

where A is the cross-section area, and P is the perimeter. The perimeter of the ellipse can be computed as:

$$P \approx \pi \left[3(a+b) - \sqrt{(3a+b)(a+3b)} \right] \tag{4.2}$$

Equation 4.2 is an approximation of the ellipse perimeter, where a is the semi-major axis and b is the semi-minor axis. The chosen elliptical tube has a semi-major axis of $a = 1.5mm$ and a semi-minor axis of $b = 0.8mm$. For these dimensions, the resulting hydraulic diameter is:

$$D_H = \frac{4\pi ab}{\pi \left[3(a+b) - \sqrt{(3a+b)(a+3b)} \right]} = 2.039mm \tag{4.3}$$

which is within less than 2% of the hydraulic diameter of the round tubes. A comparison of the elliptical and round tube geometry is given in Figure 4.4.

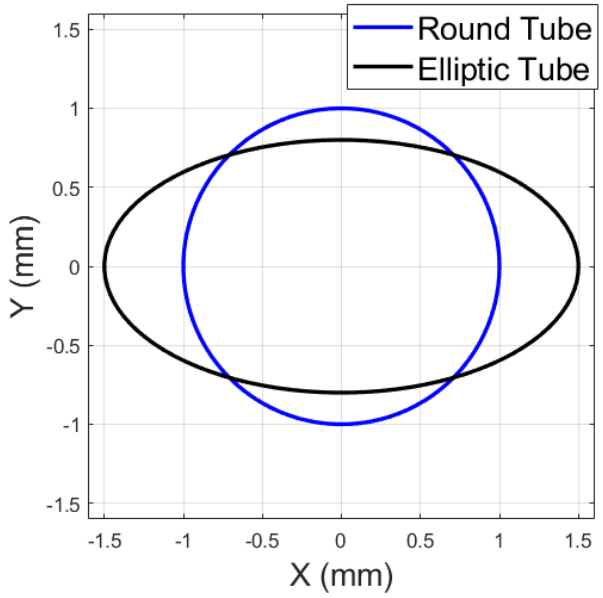

Figure 4.4: Comparison of the round and elliptical tube shapes

4.2.2. FLOW DOMAIN FOR ELLIPTICAL TUBES BANKS - $P_L = P_T = 2$ (CASE A)

In Case A the relative pitches between the elliptical tubes are the same as in the baseline tube bundle design, namely $P_L = P_T = 2$. The relative pitches for an elliptical tube array are computed according to equations 4.4 and 4.5 for the longitudinal and transverse pitch, respectively.

$$P_L = \frac{S_L}{2a} \tag{4.4}$$

$$P_T = \frac{S_T}{2b} \tag{4.5}$$

Using the above equations and the previously defined semi-major and semi-minor axis, the absolute pitches are $S_T = 3.2mm$ and $S_L = 6mm$. The mass flow rate going through the tube bank is identical to that of the baseline case. The inlet velocity has to be increased to $U_\infty = 4.9m/s$ to compensate for the decrease in S_T.

The velocity at the minimum cross-section U_m and the Reynolds number Re_D are computed differently than for the round tube case. Instead of using the tube diameter to compute Re_D, the tube chord is used. Therefore, the Reynolds number is computed as Re_c:

$$Re_c = \frac{U_m 2a}{\nu} \tag{4.6}$$

where the chord is double the semi-major axis a. The velocity at the minimum cross-section is computed using the maximum tube thickness as:

$$U_m = \frac{U_\infty S_T}{2b} \tag{4.7}$$

where $2b$ is double the semi-minor axis. For Case A equations 4.7 and 4.6 give $U_m = 9.9 m/s$ and $Re_c = 2222$.

The geometry of the 7 elliptical tube array with the relative pitches of $P_L = P_T = 2$ is displayed in Figure 4.5. Except for the inlet velocity, all the other boundary conditions are identical to those described in Section 2.5.2.

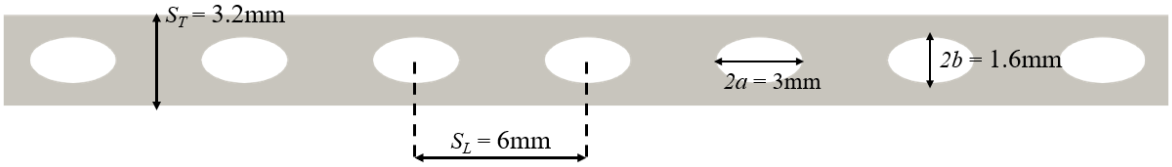

Figure 4.5: Geometry of Case A

4.2.3. FLOW DOMAIN FOR ELLIPTICAL TUBES BANKS - $P_L = 1.33$ $P_T = 2.5$ (CASE B)

In Case B the pitch between the tubes $S_L = S_T = 4mm$ are the same as the bundle with round tubes. It follows that for this test case the relative pitches are $P_L = 1.33$ and $P_T = 2.5$ according to equations 4.4 and 4.5. Since the transverse pitch S_T is not modified, the inlet velocity is maintained constant at $U_\infty = 3.986 m/s$. The Reynolds number based on the chord of the tube is the same as in Case A, namely $Re_c = 2222$.

The geometry of the 7 elliptical tube array with the relative pitches of $S_L = S_T = 4mm$ is displayed in Figure 4.6. For this case, all the boundary conditions are identical to those described in Section 2.5.2.

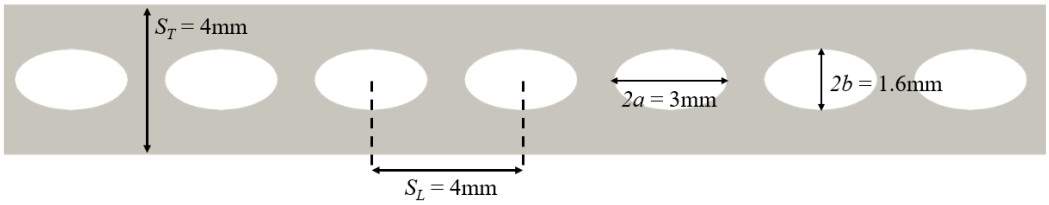

Figure 4.6: Geometry of Case B

4.3. NUMERICAL SIMULATIONS

4.3.1. CASE A

The flow through the elliptical tube rows was computed using both the SST and Realizable $k-\epsilon$ models. The corresponding flowfields are presented in Figure 4.7. Similar to the simulations presented in section 2.5.6, the SST model predicts a longer wake for the last tube than the Realizable $k-\epsilon$ model.

The simulations converged to a steady-state solution for both turbulence models. Table 4.1 reports the values of the main performance indicators. The performance varies significantly depending on the chosen turbulence model. In the case of SST ξ is 16% lower than in the simulations with the Realizable $k-\epsilon$ model. The difference in the Nusselt number is also significant, and is about 30% lower.

Due to the lack of experimental data for this type of tube array, it is difficult to assess which model is more accurate. However, both models show a similar trend in performance with respect to the test case with the round tubes. The elliptical tube bank shows an increased friction factor and Nusselt number compared to the round tube bank. Since both tube banks have the same relative pitches $P_L = P_T = 2$, this increase is likely due to two factors. First, the Reynolds number in the elliptical tube case is double that of the round tube case. This difference in Re comes down mainly to the difference in the tube's chord, since the mass flow rate

through the tube banks is the same for the two cases. Second, the surface of the elliptical tube is 20% larger than that of the round tube. The increase in the tube's surface has a direct effect on ΔT and Δp. This is shown in Table 4.2, where the difference between the performance of the elliptical tubes and the round tubes is given for the two turbulence models.

For the simulation with the SST model, the Δp is up to 160% larger for the elliptical tubes, whereas ΔT is around 60% larger than in the case of round tubes. In the case of the Realizable $k-\epsilon$ model, the computed Δp and ΔT are around 120% and 45% larger for the elliptical tube case than the baseline design with round tubes. This is likely due to the larger distance between the tubes, which implies that there is more space for mixing to occur in the wakes of the tubes. As a consequence of the increase in turbulent mixing, the heat transfer also increases for the elliptical tube bundles. At the same time, the streamwise velocity between the tubes becomes more uniform, which promotes earlier flow reattachment on the downstream tubes. As a result, a larger portion of the tube walls experiences attached flow. This increase in attached flow leads to higher friction drag on the tube surfaces, ultimately causing a greater pressure drop across the tube bundle.

A view of the flow field around the tube walls can be found in Annexe B.6.

Another disadvantage of this layout is the increase in the volume of the BTHX that tends to be 20% larger than in the case of round tubes. As Bacellar et al. [9] indicate, BTHX volume is an important parameter, especially for applications requiring compactness.

Turbulence Model	Δp [Pa]	ΔT [K]	ξ [-]	Nu [-]
$k-\omega$ SST	116.041	36.497	0.2616	13.357
Realizable $k-\epsilon$	139.395	48.516	0.3143	19.499

Table 4.1: Overall performance obtained for Case A with $k-\omega$ SST and Realizable $k-\epsilon$ as turbulence models.

Turbulence Model	Δp_{diff} [%]	ΔT_{diff} [%]	ξ_{diff} [%]	Nu_{diff} [%]
$k-\omega$ SST	159.02	61.134	65.772	51.956
Realizable $k-\epsilon$	122.689	44.802	43.198	35.13

Table 4.2: Difference in performance between the tube bundle of Case A and the one with round tubes according to the simulation results with $k-\omega$ SST and Realizable $k-\epsilon$ model.

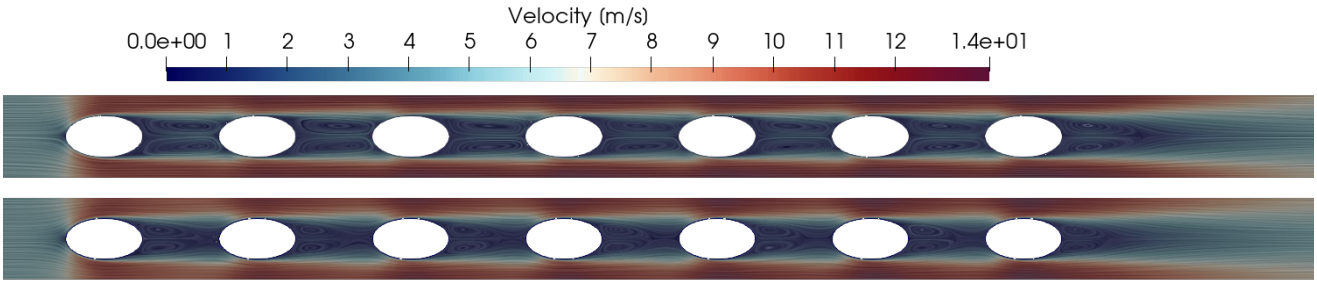

Figure 4.7: Comparison of the velocity fields for the SST (top), Realizable $k-\epsilon$ (bottom) simulations for Case A

4.3.2. CASE B

In this test case, the distance between the tubes is $4mm$ in both the transversal and longitudinal direction. The flow fields were again computed using the SST and Realizable $k-\epsilon$ models, and the resulting velocity contours are presented in Figure 4.8. As before, the results of the SST model exhibit a longer wake after the last tube than the solution computed with the High-Reynolds model.

Table 4.3 shows that this BTHX layout results in lower Δp and ΔT for both turbulence models than the baseline design with round tubes. The difference in the performance parameters is given in Table 4.4. According to both simulations, Δp is half of that of the bundle with round tubes. However, this comes at a cost of ΔT, which reduces by around 10% and 16% for the simulations with Realizable and SST models, respectively. Since the spacing between tubes is lower in this case, the wakes of the tubes can not fully develop

before they reach the downstream tube. This means that most of the fluid flows in the gap between the tube arrays, away from the tube surfaces. This, together with the decreased levels of turbulent mixing in the tube wakes, explains the trends in Δp and ΔT.

These results show that replacing round tubes with elliptical ones is a viable solution if the design target is to considerably reduce Δp. The reduction in ΔT could also be mitigated by slightly increasing the longitudinal pitch P_L at the cost of small increases in pressure drop. This highlights the importance of optimizing the tube pitches for BTHX.

Turbulence Model	Δp [Pa]	ΔT [K]	ξ [-]	Nu [-]
$k-\omega$ SST	22.843	18.826	0.0515	6.145
Realizable $k-\epsilon$	31.778	29.978	0.07165	10.49

Table 4.3: Overall performance obtained for Case B with $k-\omega$ SST and Realizable $k-\epsilon$ as turbulence models.

Turbulence Model	Δp_{diff} [%]	ΔT_{diff} [%]	ξ_{diff} [%]	Nu_{diff} [%]
$k-\omega$ SST	-49.011	-16.883	-67.372	-30.091
Realizable $k-\epsilon$	-49.233	-10.526	-67.357	-27.304

Table 4.4: Difference in performance between the tube bundle of Case B and the one with round tubes according to the simulation results with $k-\omega$ SST and Realizable $k-\epsilon$ model.

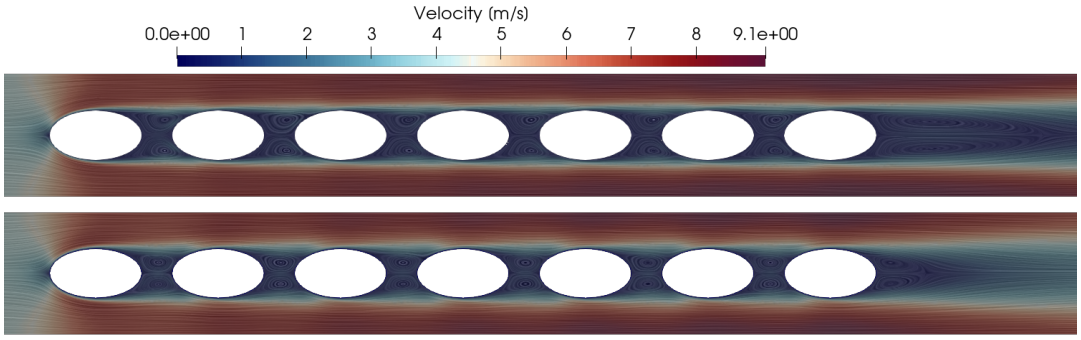

Figure 4.8: Comparison of the velocity fields for the SST (top), Realizable $k-\epsilon$ (bottom) simulations for Case B

4.4. SHAPE OPTIMIZATION OF ELLIPTICAL TUBES

The two tube arrays presented in Section 4.3 were optimized with the shape optimization procedure described in Chapter 3. Each tube array was optimized using the SLSQP optimization algorithm. Other than different constraints, chosen to better match the new tube shape, the optimization framework is the same as that used for the shape optimization of the round tubes. The results presented in the following section were obtained after remeshing the geometry resulting from the optimization procedure.

4.4.1. SHAPE OPTIMIZATION OF ELLIPTICAL TUBES (CASE A)

Due to the lower value of $S_T = 3.2mm$ used in this case, the thickness variables were constrained in a smaller design space: $10^{-5}m \geq T_i^l; T_i^u \geq 1.2 \cdot 10^{-3}m$. The temperature constraint was set at $\Delta T \geq 36.4K$. The cross-section area constraint was $A \geq 3.7mm^2$. The resulting shape of the optimized tube is presented in Figure 4.9, where it is plotted against the initial elliptical tube shape. The resulting tube tends towards a rectangular shape with round corners. The L.E. and T.E. of the tube, as for the previous optimizations, have a blunt shape with a small curvature. The comparisons of the flowfields of the optimized tube bank and the initial elliptical tube bank are given in Figure 4.10 and 4.11 for the Realizable $k-\epsilon$ and SST models respectively.

The overall performance of the optimized elliptical tube is given in table 4.5. Here, the simulation with SST model, which is the turbulence model used during the optimization process, gives an improvement in Δp of 13.5% with a reduction in ΔT of only 0.86%. The Realizable $k-\epsilon$ model, gives a much lower reduction

of Δp, of only 1.65%. This discrepancy is likely due to the differences in the velocity fields computed by the two turbulence models for the optimized tube. The High-Reynolds model predicts a delayed flow separation compared to the SST model, and thus results in greater friction drag and pressure drop computed by the Realizable model. This difference in Δp shows one of the main shortcomings of using inaccurate turbulence models. A view of the flow field around the optimized tubes can be found in Annexe B.6.

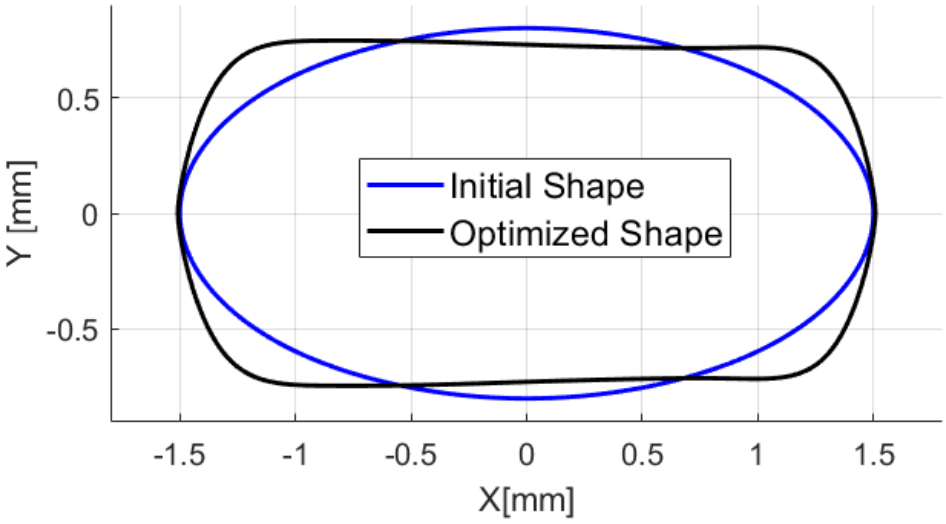

Figure 4.9: Comparison between the initial and optimized shapes for Case A

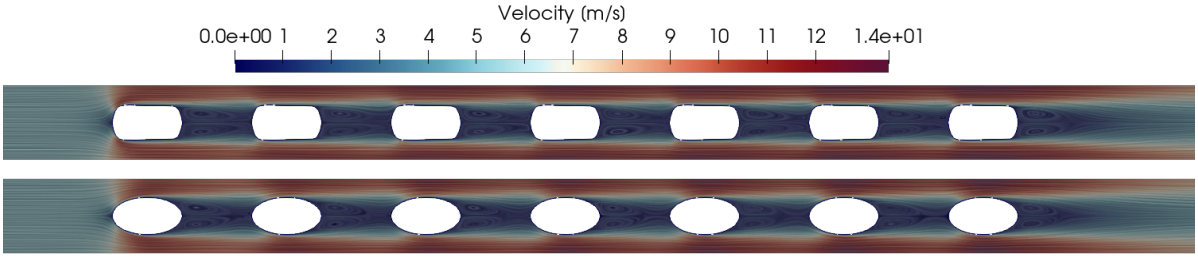

Figure 4.10: Flowfields of the optimized design (top) compared to the baseline elliptical tube design obtained with the Realizable $k-\epsilon$ model

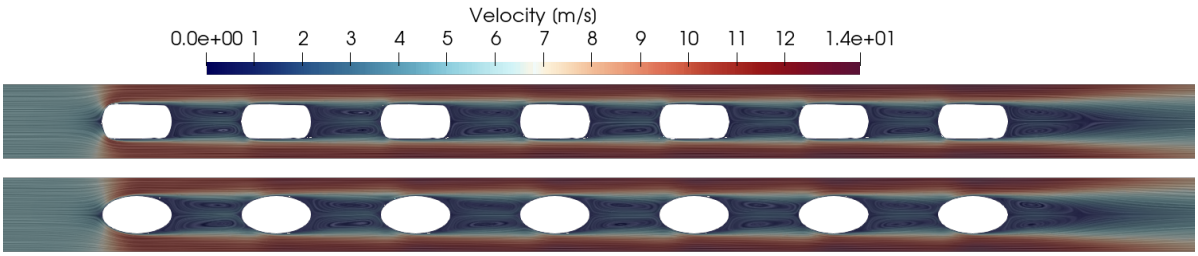

Figure 4.11: Flowfields of the optimized design (top) compared to the baseline elliptical tube design obtained with the $k-\omega$ SST model

4.4.2. SHAPE OPTIMIZATION OF ELLIPTICAL TUBES (CASE B)

The design space for the thickness variables of this tube array is $10^{-5}m \geq T_i^l; T_i^u \geq 1.5 \cdot 10^{-3}m$. The area constraint is $A \geq 3.7mm^2$, and the temperature constraint is $\Delta T \geq 18.8K$. The resulting shape of the optimization

Tube Design-Turbulence Model	Δp [Pa]	ΔT [K]	Change in Δp [%]	Change in ΔT [%]
Elliptical Tubes - SST	116.041	36.497	-	-
Optimized Elliptical Tube-SST	100.296	36.18	-13.568	-0.86
Elliptical Tube-Realizable $k-\epsilon$	139.395	48.516	-	-
Optimized Elliptical Tube-Realizable $k-\epsilon$	137.083	48.64	-1.6585	0.267

Table 4.5: Comparison of the overall performance obtained for the optimized design of Case A with $k-\omega$ SST and Realizable $k-\epsilon$.

process is plotted in Figure 4.12. This time, the optimized tube approaches an oval shape. The L.E. and T.E. are similar to the original shape with a slightly lower curvature. The flowfields computed using the two turbulence models (Realizable $k-\epsilon$ and SST) are displayed in Figures 4.13 and 4.14.

The performance of the optimized elliptical tube array is given in table 4.6. In this case, the simulation with SST model shows a reduction in Δp of 6.22% while the ΔT also increases by 1.1%. The results with Realizable $k-\epsilon$, conversely, features a larger reduction of pressure drop of 10.126%, but the ΔT also decreases by 3.819%. The reduction in ΔT predicted by different turbulence models is an important limitation for the obtained optimal designs. A possible solution could be the use of stricter constraints for the outlet temperature.

In absolute terms, these reductions in Δp are quite small, especially when compared to the reduction obtained by just replacing the round tubes with elliptical tubes. Altogether, the shape optimization process does not yield a significant improvement in Δp for the test cases at hand. The identified optimal shape may be of practical interest for larger tube arrays where a 10% improvement in pressure drop would be much more significant in absolute terms. The optimized elliptical tube results in a slight decrease in heat transfer compared to the original design. This reduction adds to the loss in heat transfer that occurs when round tubes are replaced with elliptical ones. An alternative approach could involve optimizing elliptical tubes using the outlet temperature as the objective function. This would allow for a design that improves both heat transfer and pressure drop performance, surpassing the performance of the round tubes in both aspects.

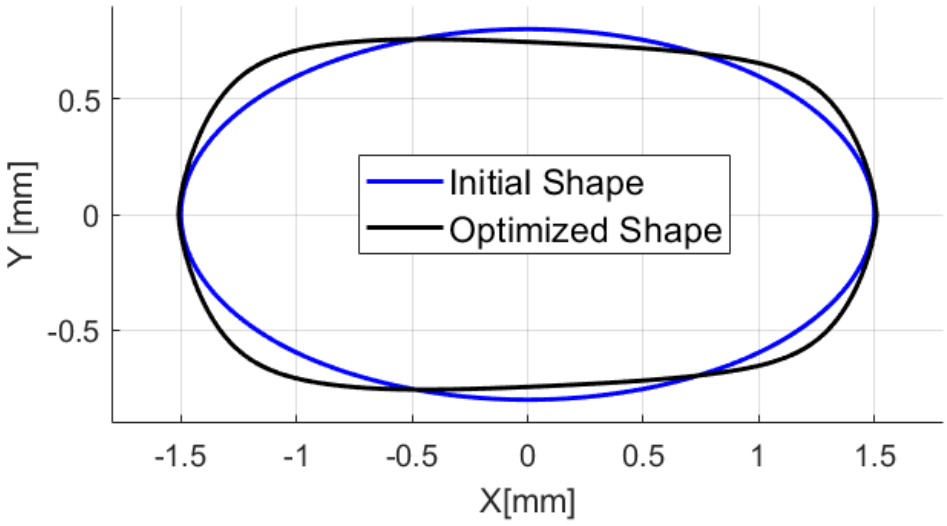

Figure 4.12: Comparison between the initial and optimized shapes for Case B

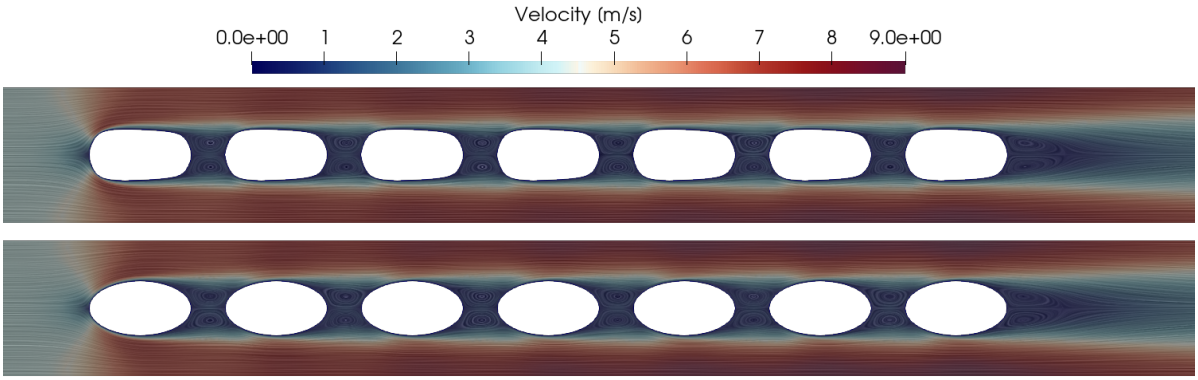

Figure 4.13: Flowfields of the optimized designs (top) compared to the baseline elliptical tube design obtained with the Realizable $k-\epsilon$ model

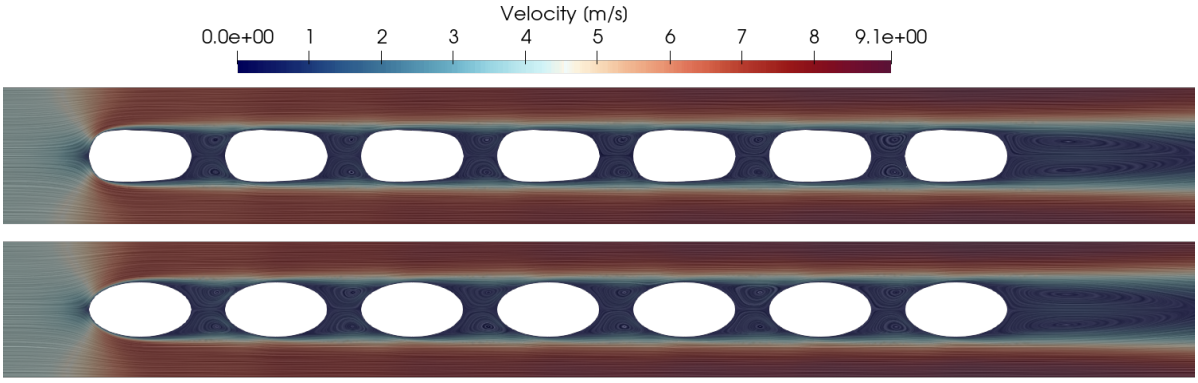

Figure 4.14: Flowfields of the optimized designs (top) compared to the baseline elliptical tube design obtained with the $k-\omega$ SST model

Tube Design-Turbulence Model	Δp [Pa]	ΔT [K]	Change in Δp [%]	Change in ΔT [%]
Elliptical Tube - SST	22.843	18.826	-	-
Optimized Elliptical Tube-SST	21.422	19.031	-6.22	1.088
Elliptical Tubes-Realizable $k-\epsilon$	31.778	29.978	-	-
Optimized Elliptical Tube-Realizable $k-\epsilon$	28.56	28.833	-10.126	-3.819

Table 4.6: Performance for the optimized design of case B estimated with the $k-\omega$ SST and Realizable $k-\epsilon$ models.

4.5. SUMMARY

In this chapter, the use of elliptical tubes in BTHX was studied and compared to the case of round tubes. For this purpose, two elliptical tube cases were constructed starting from the round tube case described in Chapter 2. The first case preserves the same relative pitch ratio $P_L = P_T = 2$ (Case A), while the second one preserves the absolute pitch $S_L = S_T = 4mm$ (Case B). The mass flow rate through the elliptical bundles was maintained the same as for the initial round tube case. The elliptical tubes had the same hydraulic diameter as the round tubes to preserve the flow conditions inside of the tubes of the BTHX. The flow simulations show that Case A features significantly higher pressure drop and heat transfer rates than the round tube array. On the other hand, Case B exhibits significantly lower Δp and a slightly lower ΔT. This indicates that it would be possible to improve the Δp of a BTHX by replacing round tubes with elliptical ones if the appropriate tube spacing is determined to compensate for the reduction in heat transfer.

The shape optimization of elliptical tubes was also studied. The same optimization framework described in Chapter 3 was applied with slightly modified constraints and design bounds. The performances computed for the optimized tube shapes were found to depend greatly on the turbulence model used. However, regardless of the turbulence model, the shape optimization yielded minor improvements in Δp, significantly lower than those obtained for the optimization of round tubes. This is likely because the elliptical shape is already close to the optimal one, leaving less margin for improvement. The shape obtained through the optimization of Case B resembled an oval, indicating that this shape could potentially be better for the given flow conditions.

5

CONCLUSIONS AND RECOMMENDATIONS

This chapter presents the conclusions and recommendations of the study. The conclusions regarding the numerical modelling of flows through tube banks and the shape optimization of BTHX tubes are reviewed in Section 5.1. Section 5.2 provides a set of recommendations for future work on the shape optimization of BTHX tubes based on the findings outlined in this report.

5.1. CONCLUSIONS

This thesis aimed to implement a shape optimization framework based the adjoint method for inline BTHX. To this end, the modelling of flow and heat transfer through tube banks was studied in Chapter 2 and the adjoint optimization framework was presented in Chapter 3. The considered test case is an array of 7 round tubes with an air-side flow characterized by $Re_D \approx 1000$. However, Chapter 4 also covers the numerical modelling and shape optimization of non-cylindrical tubes.

As a result of the numerical analysis carried out, several important conclusions were drawn. Regarding the CFD simulations carried out for the in-line BTHX case study presented in Chapter 2, it was shown that the choice of turbulence model is decisive in accurately modelling the flow through tube banks. For the given flow conditions of $Re \approx 1000$, it was found that the most suitable turbulence model among those tested is Realizable $k-\epsilon$, which is a high-Reynolds model. This model performed better in matching the pressure drop and heat transfer rate predicted by the empirical correlations. The low-Reynolds models used, such as $k-\omega$ SST or SA, tend to underestimate the ΔP and ΔT for the flow conditions of $Re \approx 1000$. This is critical for performing shape optimization as the CFD solver used for this purpose, namely SU2, offers only low Reynolds turbulence models. Of the two low-Reynolds models, the SST model predicted results closer to the empirical correlations and, therefore, was chosen as the turbulence model to be used in the shape optimization framework.

For the 7-round tube in-line case presented in Chapter 2, the simulations with the SST model predicted a Δp and ΔT 35.7% and 39.1% lower than the ones predicted by the empirical correlations. In contrast, the results predicted with the Realizable $k-\epsilon$ model show only a 6% difference for Δp and 7.3% for ΔT compared to values predicted for the same empirical correlations.

The performance of the BTHX computed with the two turbulence models of SU2 (SST and SA) differs significantly from that estimated through the empirical correlations. This indicates that the CFD simulations may not predict the correct trend between the objective function and the design variables during shape optimization. For this reason, the high fidelity Realizable $k-\epsilon$ model should be used to verify the performance of the optimized design.

Section 2.6 presents the effects of boundary conditions on the results of the CFD simulations. This section showed that the choice of the boundary conditions for the top and bottom borders of the flow domain is only important for the SST model. For SST, the Δp predicted by the simulations with periodic boundary conditions was 3.49% higher than that computed with symmetric boundary conditions. Also, the flow field computed with periodic boundary conditions more closely resembles those described by the studies found in the literature (West [5], and Blackall et al. [2]). For Realizable $k-\epsilon$, the difference between the results of the simulations with periodic and symmetric boundary conditions was negligible. In both cases, the asymmetric vortex patterns in the wakes of the tubes were not present.

It should be noted that the accuracy of the turbulence models greatly depends on the flow conditions. Section 2.7 showed that for lower Reynolds numbers, $Re \approx 200$, the use of the SST and SA models leads to more accurate results for Δp and ΔT than the simulation with the Realizable $k-\epsilon$. This was shown by simulating the in-line BTHX presented by Kasagi et al. [43], for which experimental data are available. In this case, the Realizable $k-\epsilon$ was found to overpredict the Δp by 39.4% and the ΔT by 24.3%. The SST model was fairly close to the results obtained by Kasagi et al. [43], with Δp at 2.9% and the ΔT at 5.4% of the results. Therefore, before starting the shape optimization process, assessing which model is the most accurate is important.

Regarding the shape optimization of round tubes, Chapter 3 shows that even with the limitations related to the accurate prediction of the objective function, the optimization framework can still produce improved designs. The objective of minimizing pressure drop was achieved using both optimization algorithms (SLSQP and SNOPT). Of the two optimization algorithms, SLSQP performed better in terms of minimizing the pressure drop across the tube bank. The reduction in Δp estimated using the High-Reynolds model was around 22.3% and 7.9% for the SLSQP and SNOPT designs, respectively. The two resulting tubes have a similar shape, resembling a trapezoid with round corners. The SLSQP design has a higher taper than the one obtained with SNOPT, which causes the region of high-velocity flow to move further away from the tube walls. This partially explains the difference in Δp reductions obtained for the two designs.

The main issue of the optimization process is the constraint on the overall heat duty. This constraint is met in the optimization with the SST model. However, when the flow fields are recomputed with Realizable $k-\epsilon$, the ΔT is lower by up to 5% for the SLSQP design and 2% for the SNOPT design when compared to the baseline design. This clearly illustrates the issue of using a turbulent model of limited accuracy for the test case of interest.

In Chapter 4, the use of elliptical tubes in place of round tubes as initial geometry in the optimization process was investigated. Two test cases were analyzed. In the first one, the tube bundle has the same pitch ratio of the bundle with round tubes ($P_L = P_T = 2$ or Case A), whereas in the second one the absolute pitches ($S_L = S_T = 4mm$ or Case B) were chosen equal to those of the initial test case. The mass flow rate through both the elliptical tube banks was the same as for the initial round tube case. The CFD analysis of the two elliptical tube banks yielded interesting results. Case A presented a significantly larger pressure drop, while the heat transfer rate also increased considerably. Case B presented a decrease in both pressure drop and heat transfer rate. This different trend in the results occurs despite the tubes having the same geometry in both case A and B, as well as the same hydraulic diameter of the original round tubes. For the simulations carried out with the Realizable $k-\epsilon$ model, the reduction in pressure drop for Case B was nearly 50% or almost double that obtained from the shape optimization of the round tubes. However, the heat transfer rate also decreases by around 10%. This indicates that substituting round tubes for elliptical ones is a viable alternative to shape optimization.

The shape optimization of elliptical tubes did not yield major improvements. This is likely due to the fact that the tube shape is already close to the optimum one. The resulting tube designs tend towards a more oval shape. The performance of the optimized tube shapes was found to be highly dependent on the turbulence model used. Without experimental data, it is difficult to assess which turbulence model is more accurate for these optimized tube shapes. However, for the optimized design of Case B, Realizable $k-\epsilon$ shows some promising results in terms of pressure drop reduction. Unfortunately, this also comes at the expense of further reductions in the heat transfer rate.

In conclusion, this thesis addresses the challenges involved in the numerical modelling and shape optimisation of in-line BTHX. In particular, the simulations focus on the flow established outside the tubes at $Re \approx 1000$. The choice of turbulence model was shown to be critical for accurately modelling the flow, with the Realizable $k-\epsilon$ model being the only one capable of closely reproducing results consistent with empirical correlations. However, this model failed to capture the flow asymmetry in the wake of the tubes, which has been extensively described in the literature. For different flow conditions at lower Reynolds numbers ($Re \leq 250$), the SST and SA models were found to provide better agreement with experimental data. Turbulence modelling plays a crucial role in the optimisation process, as errors in the computation of the pressure drop and of the heat transfer can propagate into the design iterations. The Realizable $k-\epsilon$ model was used to verify the performance of the optimised tube designs. Another factor influencing the numerical modelling and optimisation process is the initial shape of the tube. Closely spaced elliptical tube arrays were found to be more efficient in minimising the pressure drop compared to cylindrical arrays, while widely spaced elliptical tube arrays produced significantly higher pressure drops, along with increased heat transfer. Overall, these findings highlight the importance of accurate numerical modelling in the design and optimisation of BTHXs and point to potential pathways for improving heat exchanger performance through both shape optimisation

and the adoption of alternative tube geometries.

5.2. RECOMMENDATIONS

The primary challenge encountered during the optimization process was accurately predicting the performance of the BTHX. The low-Reynolds models available in SU2 were unable to accurately model the flow through the BTHX at $Re \approx 1000$.

This issue could be addressed by incorporating a high-Reynolds model in the optimization framework. Currently, SU2 provides only two turbulence models (SST and SA), neither of which is suitable for the flow conditions of $Re \approx 1000$ in in-line BTHX. Therefore, to improve the optimization framework, a high-Reynolds model (Realizable $k-\epsilon$ or RNG) should be implemented in SU2. Alternatively, the optimization framework could be adapted to utilize other CFD software that already includes high-Reynolds models. In this thesis, the ANSYS-Fluent software package was used, but other open-source alternatives, such as OpenFOAM, might also serve as viable substitutes for SU2. The applicability of a discrete adjoint framework implemented in OpenFOAM for incompressible flows with heat transfer was demonstrated in works such as that of Towara et al. [60]. ANSYS-Fluent also offers an adjoint solver whose capabilities are outlined in the ANSYS-Fluent Tutorial Guide [61].

It is also important to consider the impact of the number of tubes on the accuracy of numerical results compared to empirical correlations. Section 2.6 shows that increasing the number of tubes in an array reduces the accuracy of the SST simulations, whereas the Realizable $k-\epsilon$ results remain unaffected. Consequently, if shape optimization is performed using the framework outlined in Chapter 3, it is preferable for the tube array to contain between 5 to 10 tubes. This ensures that the errors caused by the CFD simulations with low Reynolds models are reduced.

There are also alternative methods for improving the performance of the BHTX without the use of shape optimization. As demonstrated in Chapter 4, using more streamlined shapes, such as ellipses, is a viable approach to reducing the pressure drop in in-line BTHX. The optimization of Case B also suggests that oval shapes may be advantageous under the given flow conditions. However, the main drawback of this approach is that streamlined shapes tend to perform slightly worse in terms of heat transfer compared to round tubes with the same absolute pitch.

The two elliptical tube cases further illustrate that changing the relative pitch has a significant impact on the performance of the BTHX. Therefore, the reduction in heat transfer rate observed with the second test case could be mitigated through a layout optimization process similar to that proposed by Pai Raikar et al. [10].

A

TURBULENCE MODELS-TERMS AND MODEL CONSTANTS

A.1. BOUSSINESQ METHOD

The other constituent terms of the Boussinesq method are the Strain rate S_{ij} tensor:

$$S_{ij} = \frac{1}{2}\left(\frac{\partial U_i}{\partial x_j} + \frac{\partial U_j}{\partial x_i}\right) - \frac{1}{3}\delta_{ij}\frac{\overline{U_k}}{\partial x_k} \tag{A.1}$$

δ_{ij} is the Kronecker delta:

$$\delta_{ij} = \begin{cases} 1 & \text{if } i = j \\ 0 & \text{if } i \neq j \end{cases} \tag{A.2}$$

A.2. SPALART-ALLMARAS

f_{v1} is the viscous damping function:

$$f_{v1} = \frac{\chi^3}{\chi^3 + C_{v1}^3} \tag{A.3}$$

and the χ term is:

$$\chi = \frac{\tilde{\nu}}{\nu} \tag{A.4}$$

The $\tilde{S}$ term is related to the turbulent production.

$$\tilde{S} = \sqrt{2S_{ij}S_{ij}} + \frac{\tilde{\nu}}{\kappa^2 d^2} f_{v2} \tag{A.5}$$

Where d is the distance from the walls and the $\sqrt{2S_{ij}S_{ij}}$ is the magnitude of vorticity.

$$f_{v2} = 1 - \frac{\chi}{1 + \chi f_{v1}} \tag{A.6}$$

$$S_{ij} = \frac{1}{2}\left(\frac{\partial u_i}{\partial x_j} + \frac{\partial u_j}{\partial x_i}\right) \tag{A.7}$$

$$f_w = g\left[\frac{1 + C_{w3}^6}{g^6 + C_{w3}^6}\right]^{\frac{1}{6}} \tag{A.8}$$

$$g = r + C_{w1}\left(r^6 - r\right) \tag{A.9}$$

$$r = \frac{\tilde{\nu}}{\tilde{S}\kappa^2 d^2} \tag{A.10}$$

$$f_{t2} = C_{t3} e^{-C_{t4}\chi^2} \tag{A.11}$$

$$C_{w1} = \frac{C_{b1}}{\kappa^2} + \frac{1 + C_{b2}}{\sigma} \tag{A.12}$$

The constants of the Spalart-Allmaras model are: $C_{b1} = 0.1355$; $C_{b2} = 0.622$; $\kappa = 0.41$; $C_{w2} = 0.3$; $C_{w3} = 2$; $C_{v1} = 7.1$; $C_{t3} = 1.2$; $C_{t4} = 0.5$ and $\sigma = 2/3$.

A.3. $k-\epsilon$

A.3.1. $k-\epsilon$ STANDARD

P represents the rate of gain of turbulent kinetic energy, and for compressible flow, it can be written as seen in equation A.13.

$$P = \tau_{ij} \frac{\partial U_i}{\partial x_j} = 2\nu_t S_{ij} S_{ij} \tag{A.13}$$

$$f_2 = 1 - \frac{0.4}{1.8} e^{Re_T^2/36} \tag{A.14}$$

$$Re_T = \frac{\rho k^2}{\mu \epsilon} \tag{A.15}$$

$$L_k = -2\frac{\mu k}{\rho d^2} \tag{A.16}$$

$$L_\epsilon = -2\frac{\mu \epsilon}{\rho d^2} e^{-d^2/2} \tag{A.17}$$

d^+ is a function of the distance to the wall and depends on the properties of the nearest wall. In equation A.19, U is the parallel velocity to the wall and n is the normal to the wall. d is the distance to the wall. L_k and L_ϵ are user-defined source terms.

$$d^+ = \frac{d\rho\sqrt{\tau_w / rho_e}}{\mu} \tag{A.18}$$

$$\tau_w = \mu_w \left(\frac{\partial U}{\partial n}\right)_w \tag{A.19}$$

The model constants are: $\sigma_k = 1$; $\sigma_\epsilon = 1.3$; $C_\mu = 0.09$; $C_{\epsilon 1} = 1.35$; $C_{\epsilon 2} = 1.8$ and $f_1 = 1$.

A.3.2. $k-\epsilon$ RNG

Equation A.20 is the dissipation rate equation for the RNG model. The additional term $C^*_{\epsilon 2}$ is given in equation A.21

$$\frac{\partial \rho\epsilon}{\partial t} + \frac{\partial \rho\epsilon U_j}{x_j} = C_{\epsilon 1}\frac{\epsilon}{k}P - C^*_{\epsilon 2}\frac{\rho\epsilon^2}{k} + \frac{\partial}{\partial x_j}\left[\left(\mu + \frac{\mu_t}{\sigma_\epsilon}\right)\frac{\partial \epsilon}{\partial x_j}\right] \tag{A.20}$$

$$C^*_{\epsilon 2} = C_{\epsilon 2} + \frac{C_\mu \eta^3 \left(1 - \eta/\eta_0\right)}{1 + \beta\eta^3} \tag{A.21}$$

$$\eta = \sqrt{2S_{ij}S_{ij}}\frac{k}{\epsilon} \tag{A.22}$$

The model constants are: $\sigma_k = 0.7194$; $\sigma_\epsilon = 0.7194$; $C_\mu = 0.0845$; $C_{\epsilon 1} = 1.42$; $C_{\epsilon 2} = 1.68$; $\eta_0 = 4.38$ and $\beta = 0.012$.

A.3.3. REALIZABLE $k-\epsilon$

Equation A.23 is the dissipation rate equation for the Realizable k-ϵ model.

$$\frac{\partial \rho \epsilon}{\partial t} + \frac{\partial \rho \epsilon U_j}{x_j} = \frac{\partial}{\partial x_j}\left[\left(\mu + \frac{\mu_t}{\sigma_\epsilon}\right)\frac{\partial \epsilon}{\partial x_j}\right] + \rho C_1 \sqrt{2 S_{ij} S_{ij}}\epsilon - \rho C_2 \frac{\epsilon^2}{k + \sqrt{\nu\epsilon}} + L_\epsilon \tag{A.23}$$

$$C_1 = max\left[0.43, \frac{\eta}{\eta + 5}\right] \tag{A.24}$$

Other than the constant C_1 defined in equation A.24 the other model constants are: $C_{1\epsilon} = 1.44$; $C_2 = 1.9$; $\sigma_k = 1$ and $\sigma_\epsilon = 1.2$.

The terms used for computing C_μ in equation 2.30 are:

$$U^* = \sqrt{S_{ij} S_{ij} + \tilde{\Omega}_{ij} \tilde{\Omega}_{ij}} \tag{A.25}$$

Where:

$$\tilde{\Omega}_{ij} = \overline{\Omega_{ij}} - 3\epsilon_{ijk}\omega_k \tag{A.26}$$

$\overline{\Omega_{ij}}$ is the mean rate of rotation tensor in a rotating frame of reference with the angular velocity ω_w.

The other constants are: $A_0 = 4.04$; $A_s = \sqrt{6} cos\phi$ and:

$$\phi = \frac{1}{3} cos^{-1}\left(\sqrt{6}\frac{S_{ij} S_{jk} S_{ki}}{\tilde{S}^3}\right) \tag{A.27}$$

A.4. K-ω SST

The model constants are: $\alpha_1 = \frac{5}{9}$; $\alpha_2 = 0.44$; $\beta_1 = \frac{3}{40}$; $\beta_2 = 0.0828$; $\beta^* = 0.09$; $\sigma_{k1} = 0.85$; $\sigma_{k2} = 1$; $\sigma_{\omega 1} = 0.5$ and $\sigma_{\omega 1} = 0.856$

$$F_2 = tanh\left[\left[max\left(\frac{2\sqrt{k}}{\beta^* \omega y}, \frac{500\nu}{y^2 \omega}\right)\right]^2\right] \tag{A.28}$$

$$F_1 = tanh\left[\left[min\left(max\left(\frac{\sqrt{k}}{\beta^* \omega y}, \frac{500\nu}{y^2 \omega}\right), \frac{4\sigma_{\omega 2} k}{CD_{k\omega} y^2}\right)\right]^4\right] \tag{A.29}$$

In equations A.28 y is the distance to the next wall.

$$P_k = min\left(\tau_{ij}\frac{\partial U_i}{\partial x_J}, 10\beta^* k\omega\right) \tag{A.30}$$

$$CD_{k\omega} = max\left(2\rho\sigma_{\omega 2}\frac{1}{\omega}\frac{\partial k}{\partial x_i}\frac{\partial \omega}{\partial x_i}, 10^{-10}\right) \tag{A.31}$$

$$\phi = \phi_1 F_1 + \phi_2 (1 - F_1) \tag{A.32}$$

B

Additional Figures and Results

B.1. Symmetric vs Periodic Boundary Conditions - Spalart-Almaras

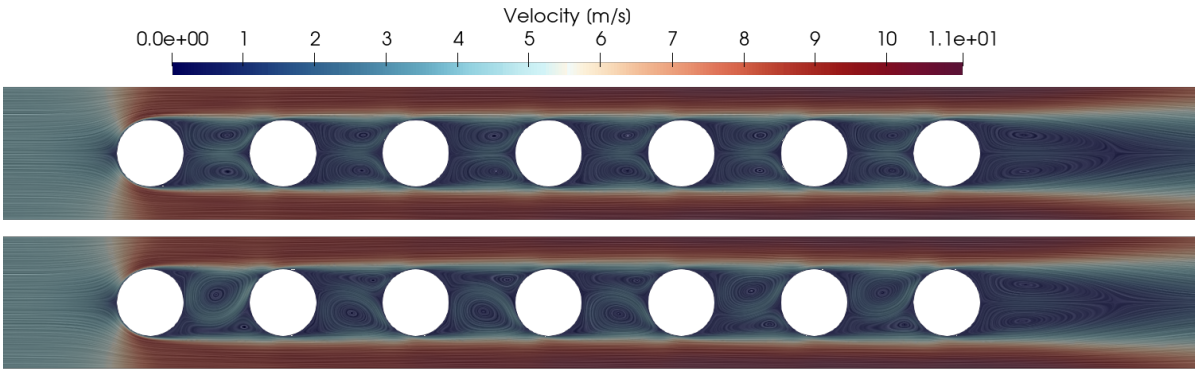

Figure B.1: Comparison of the velocity profiles for the Spalart-Allmaras simulations with symmetric (top) and periodic (bottom) boundary conditions.

Case	Δ P[Pa]	Δ T [K]	Diff Δ P [%]	Diff Δ T [%]
Symmetric Boundary	39.645	293.296	-	-
Periodic Boundary	40.58	293.5	2.3	0.06

Table B.1: Output parameters computed using periodic and symmetric boundary conditions for the 7 tube array using the Spalart-Allmaras model.

B.2. STREAMWISE VELOCITY PROFILES

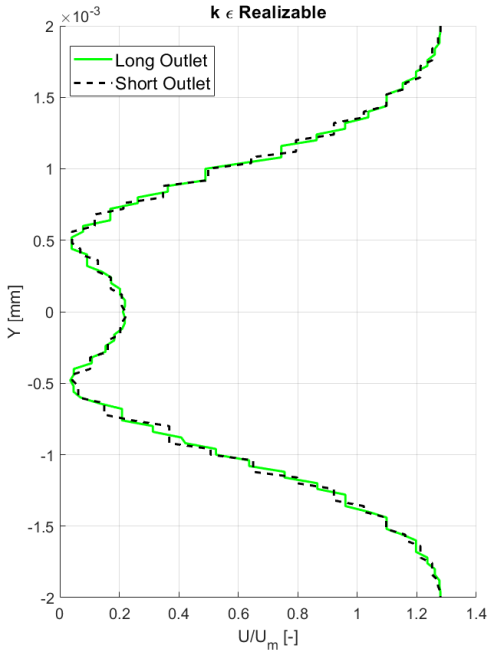

Figure B.2: Streamwise velocity profile between tubes 5 and 6 comparison between the long and short outlet simulations for the Realizable $k-\epsilon$ model.

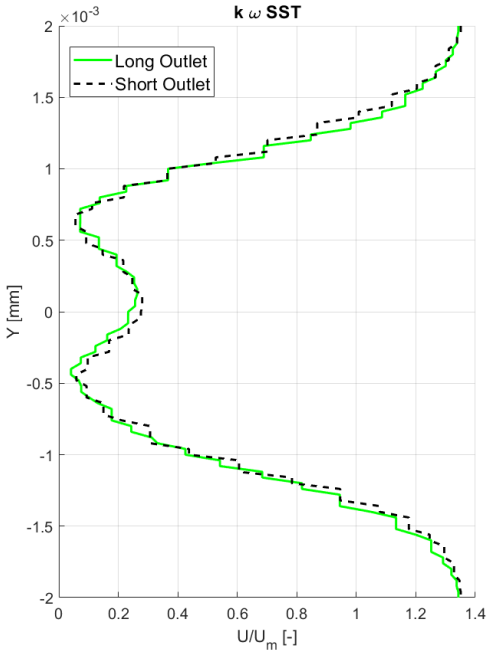

Figure B.3: Streamwise velocity profile between tubes 5 and 6 comparison between the long and short outlet simulations for the $k-\omega$ SST model.

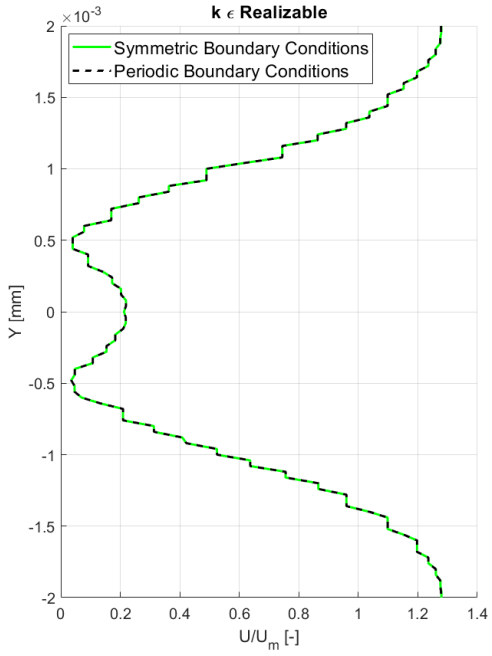

Figure B.4: Streamwise velocity profile between tubes 5 and 6 comparison between the symmetric and periodic boundary conditions for the Realizable $k-\epsilon$ model.

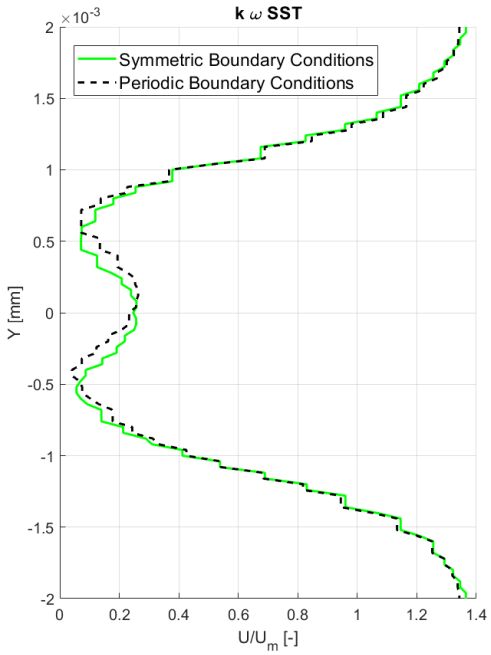

Figure B.5: Streamwise velocity profile between tubes 5 and 6 comparison between the symmetric and periodic boundary conditions for the $k-\omega$ SST model

B.3. ARRAYS WITH DIFFERENT NUMBERS OF TUBES - RESULTS

Case	Realizable			sst			Spalart-Allmaras			Empirical Corr. Data		
Nr. Tubes	7	10	15	7	10	15	7	10	15	7	10	15
ξ [-]	0.219	0.223	0.230	0.157	0.141	0.132	0.145	0.133	0.128	0.234	0.231	0.239
Nu [-]	14.428	13.730	13.444	9.098	8.007	7.355	8.147	7.476	7.137	16.864	15.399	14.800
Error(ξ) [%]	6.036	3.743	3.871	32.700	38.866	44.871	37.880	42.338	46.477	-	-	-
Error(Nu) [%]	14.442	10.841	9.165	46.052	48.005	50.302	51.690	51.450	51.776	-	-	-

Table B.2: Output parameters computed for arrays of different numbers of tubes at a flow condition around Re=1000, compared with empirical correlations.

B.4. GRADIENT VALIDATION

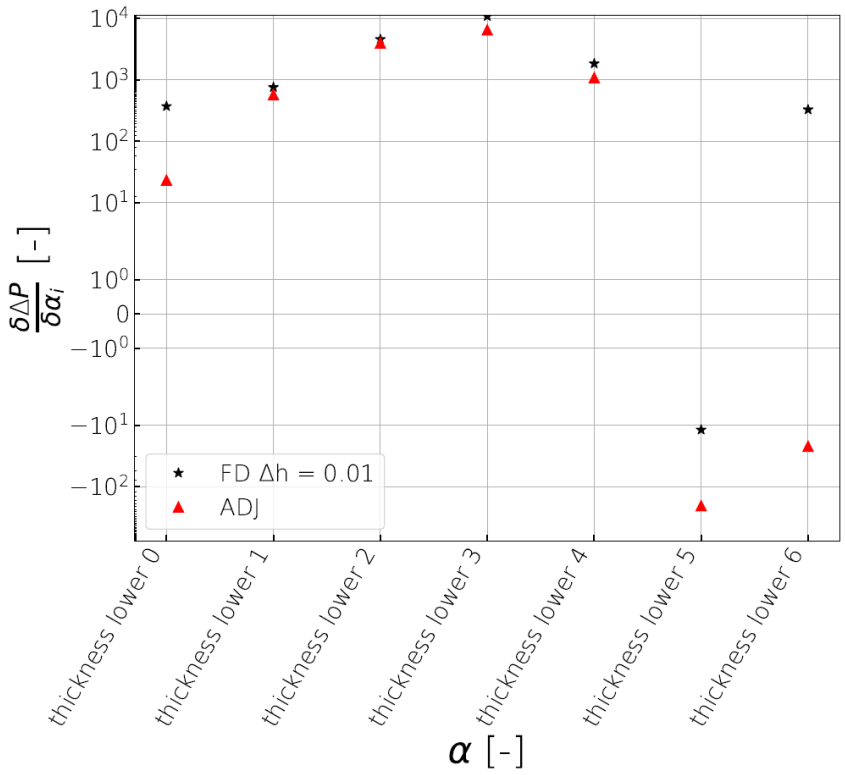

Figure B.6: Comparison between the gradients computed for the thickness variables on the Lower surface of the 1st tube using a step of $\Delta h = 1\%$.

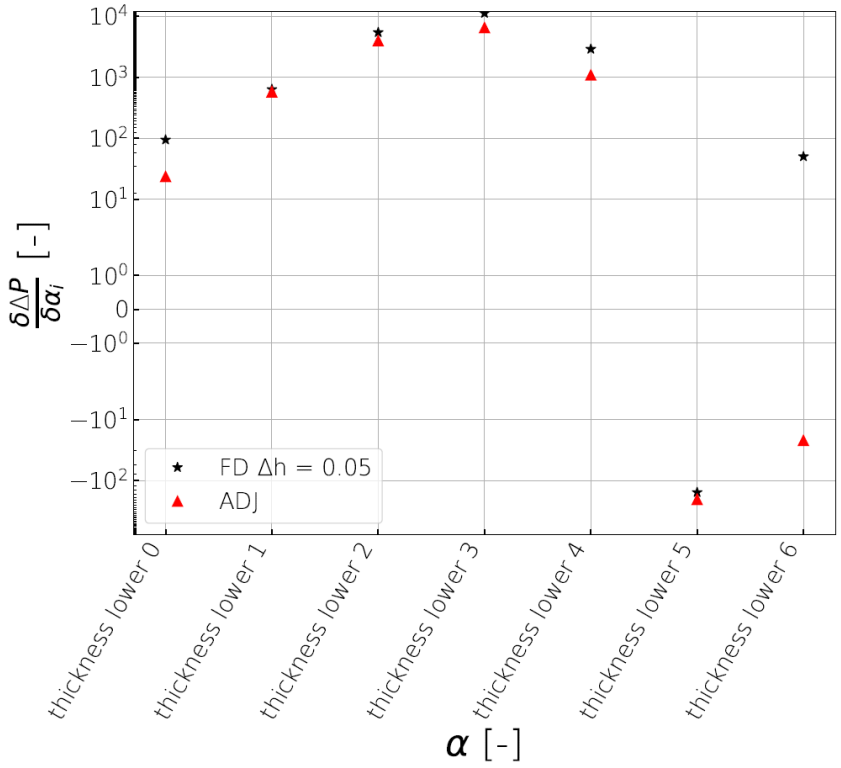

Figure B.7: Comparison between the gradients computed for the thickness variables on the lower surface of the 1st tube using a step of $\Delta h = 5\%$.

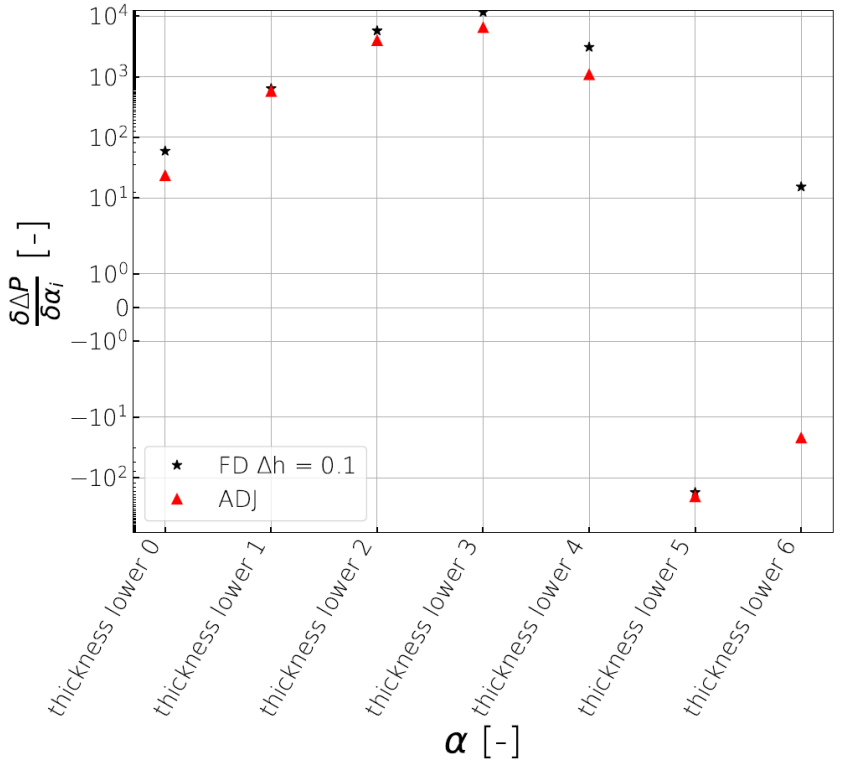

Figure B.8: Comparison between the gradients computed for the thickness variables on the lower surface of the 1st tube using a step of $\Delta h = 10\%$.

B.5. FLOWFIELDS NEAR THE ELLIPTIC TUBES

B.5.1. FLOWFIELDS NEAR THE ELLIPTIC TUBES - $P_L = P_T = 2$

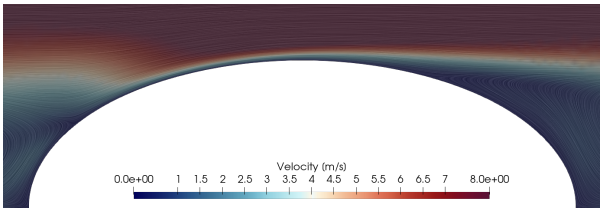

Figure B.9: Flowfield near the 6th tube of the $P_L = P_T = 2$ elliptic tube array computed with $k-\omega$ SST.

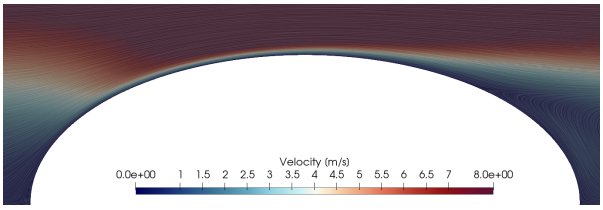

Figure B.10: Flowfield near the 6th tube of the $P_L = P_T = 2$ elliptic tube array computed with Realizable $k-\epsilon$.

B.5.2. FLOWFIELDS NEAR THE ELLIPTIC TUBES - $P_L = 1.33$ $P_T = 2.5$

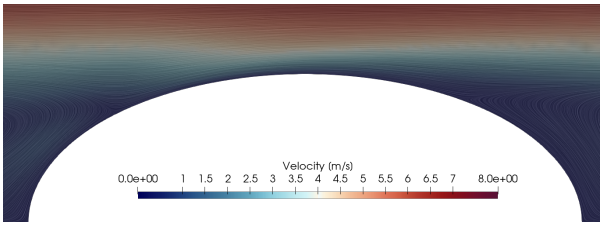

Figure B.11: Flowfield near the 6th tube of the $P_L = 1.33$ $P_T = 2.5$ elliptic tube array computed with $k-\omega$ SST.

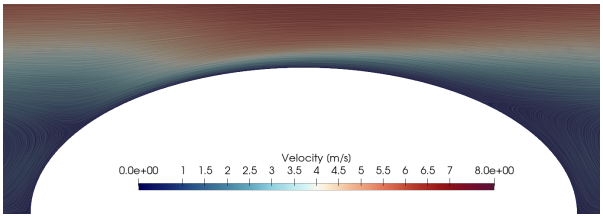

Figure B.12: Flowfield near the 6th tube of the $P_L = 1.33$ $P_T = 2.5$ elliptic tube array computed with Realizable $k-\epsilon$.

B.6. FLOWFIELDS NEAR THE OPTIMIZED ELLIPTIC TUBES

B.6.1. FLOWFIELDS NEAR THE OPTIMIZED ELLIPTIC TUBES - $P_L = P_T = 2$

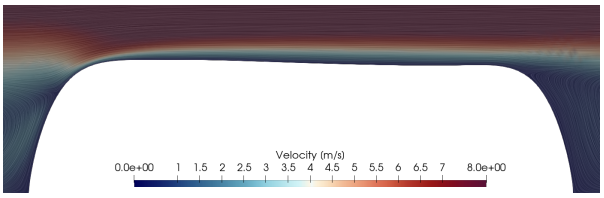

Figure B.13: Flowfield near the 6th tube of the $P_L = P_T = 2$ optimized elliptic tube array computed with $k-\omega$ SST.

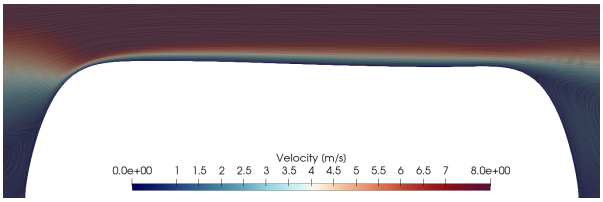

Figure B.14: Flowfield near the 6th tube of the $P_L = P_T = 2$ optimized elliptic tube array computed with Realizable $k-\epsilon$.

B.6.2. FLOWFIELDS NEAR THE OPTIMIZED ELLIPTIC TUBES - $P_L = 1.33$ $P_T = 2.5$

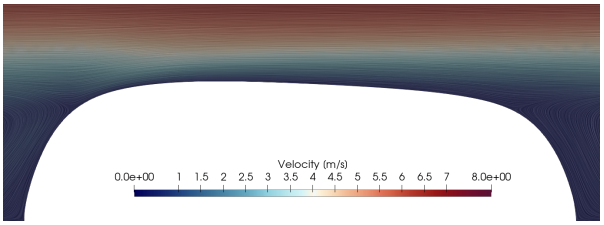

Figure B.15: Flowfield near the 6th tube of the $P_L = 1.33$ $P_T = 2.5$ optimized elliptic tube array computed with $k-\omega$ SST.

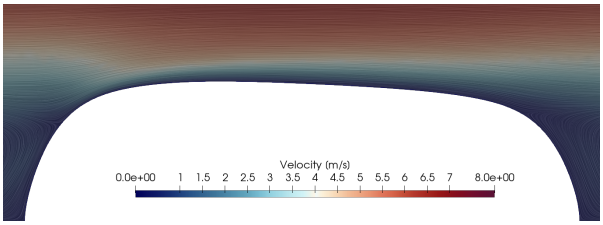

Figure B.16: Flowfield near the 6th tube of the $P_L = 1.33$ $P_T = 2.5$ optimized elliptic tube array computed with Realizable $k-\epsilon$.

C

EMPIRICAL CORRELATIONS

The following equations are valid for determining the friction coefficient and average Nusselt numbers in an in-line tube array of at least five tubes. These equations were derived from these found in the VDI Heat Transfer Atlas [22].

C.1. FRICTION COEFFICIENT

Equation C.1 shows that the friction coefficient ξ is computed as a function of a laminar and turbulent component.

$$\xi = \xi_{lam} f_{zn,1} + \left(\xi_{turb} f_{z,t} + f_{n,t}\right) F_f \tag{C.1}$$

$$F_f = 1 - exp\left(-\frac{Re + 1000}{2000}\right) \tag{C.2}$$

$$\xi_{lam} = \frac{1}{Re} \frac{280\pi \left[\left(P_L^{0.5} - 0.6\right)^2 + 0.75\right]}{\left(4 P_T P_L - \pi\right) P_T^{1.6}} \tag{C.3}$$

$$\xi_{turb} = \frac{1}{Re^{0.1(P_T/P_L)}} \left(\left(0.22 + 1.2 \frac{\left(1 - \frac{0.94}{P_T}\right)^{0.6}}{\left(P_L - 0.85\right)^{1.3}} \right) \cdot 10^{0.47((P_L/P_T) - 1.5)} + \left(0.03 \left(P_L - 1\right) \left(P_T - 1\right)\right) \right) \tag{C.4}$$

In equation C.5, the dynamic viscosity μ_w is computed using the mean wall temperature, whereas μ is computed using the mean fluid temperature.

$$f_{z,t} = \left(\frac{\mu_w}{\mu}\right)^{0.14} \tag{C.5}$$

For an array with less than 10 tubes $n_R < 10$:

$$f_{zn,l} = \left(\frac{\mu_w}{\mu}\right)^{\frac{0.57\left(\frac{n_R}{10}\right)^{0.25}}{\left(\left(\frac{4 P_T P_L}{\pi} - 1\right) Re\right)^{0.25}}} \tag{C.6}$$

For arrays with $n_R > 10$:

$$f_{zn,l} = \left(\frac{\mu_w}{\mu}\right)^{\frac{0.57}{\left(\left(\frac{4 P_T P_L}{\pi} - 1\right) Re\right)^{0.25}}} \tag{C.7}$$

For an array with less than 10 tubes $n_R < 10$:

$$f_{n,t} = \frac{1}{P_T^2} \left(\frac{1}{n_R} - \frac{1}{10} \right) \tag{C.8}$$

For arrays with $n_R > 10$:

$$f_{n,t} = 0 \tag{C.9}$$

C.2. NUSSELT NUMBER

The average Nusselt number of a tube array is a function of the Nusselt number of a single transverse tube row:

$$Nu_{l,bundle} = \frac{1+(n-1)}{n} f_A Nu_l \tag{C.10}$$

$$f_A = 1 + \frac{0.7\,(P_L/P_T - 0.3)}{\psi^{1.5}\,(P_L/P_T + 0.7)^2} \tag{C.11}$$

$$\psi = 1 - \frac{\pi}{4P_T} \tag{C.12}$$

$$Nu_l = 0.3 + \sqrt{Nu_{l,lam}^2 + Nu_{l,turb}^2} \tag{C.13}$$

$$Nu_{l,lam} = 0.664\sqrt{Re_{\psi,l}}\sqrt[3]{Pr} \tag{C.14}$$

$$Nu_{l,turb} = \frac{0.037 Re_{\psi,l}^{0.8} Pr}{1 + 2.443 Re_{\psi,l}^{-0.1}\left(Pr^{2/3} - 1\right)} \tag{C.15}$$

$$Re_{\psi,l} = \frac{U_\infty l}{\psi \nu} \tag{C.16}$$

BIBLIOGRAPHY

[1] A. Zukauskas and R. Ulinskas, *Efficiency parameters for heat transfer in tube banks,* Heat Transfer Engineering (1985), 10.1080/01457638508939614.

[2] J. L. Blackall, H. Iacovides, and J. C. Uribe, *Modeling of in-line tube banks inside advanced gas-cooled reactor boilers,* Heat Transfer Engineering **41**, 1731–1749 (2019).

[3] C. Iwaki, K. H. Cheong, H. Monji, and G. Matsui, *PIV measurement of the vertical cross-flow structure over tube bundles,* Experiments in Fluids **37**, 350 (2004).

[4] H. Iacovides, B. Launder, and A. West, *A comparison and assessment of approaches for modelling flow over in-line tube banks,* International Journal of Heat and Fluid Flow **49**, 69 (2014), 8th Symposium on Turbulence and Shear Flow Phenomena (TSFP8).

[5] A. West, *Assessment of computational strategies for modelling in-line tube banks*, PhD thesis (The University of Manchester, 2013).

[6] R. Deeb, *Numerical analysis of the effect of longitudinal and transverse pitch ratio on the flow and heat transfer of staggered drop-shaped tubes bundle,* International Journal of Heat and Mass Transfer **183** (2022), 10.1016/j.ijheatmasstransfer.2021.122123.

[7] N. Kasagi, N. Shikazono, Y. Suzuki, and T. Oku, *Assessment of high-performance compact micro bare-tube heat exchangers for electronic equipment cooling,* The Proceedings of the Thermal Engineering Conference **2003** (2003), 10.1299/jsmeted.2003.447.

[8] R. Hilbert, G. Janiga, R. Baron, and D. Thévenin, *Multi-objective shape optimization of a heat exchanger using parallel genetic algorithms,* International Journal of Heat and Mass Transfer **49**, 2567 (2006).

[9] D. Bacellar, V. Aute, H. Zhiwei, and R. Radermacher, *Design optimization and validation of high performance heat exchangers using approximation assisted optimization and additive manufacturing,* Science and Technology for the Built Environment **23** (2017), 10.1080/23744731.2017.1333877.

[10] P. Raikar, O. Bociar, C. De Servi, and N. Anand, *Shape and layout optimization of bare-tube heat exchangers using the adjoint method and cad-based parametrization,* (2024).

[11] T. D. Economon, *Simulation and adjoint-based design for variable density incompressible flows with heat transfer,* AIAA Journal **58**, 757–769 (2020).

[12] R. Agromayor, N. Anand, J.-D. Mueller, M. Pini, and L. Nord, *A unified geometry parametrization method for turbomachinery blades,* Computer-Aided Design **133**, 102987 (2021).

[13] G. Merker and H. hanke, *Heat transfer and pressure drop on the shell-side of tube-banks having oval-shaped tubes,* International Journal of Heat and Mass Transfer **29**, 1903 (1986).

[14] N. Tanatsugu, M. Oguma, T. Mizutani, and T. Yano, *Thermal design of a hydrogen heater for an air turboramjet engine,* Experimental Thermal and Fluid Science **10**, 248 (1995), aerospace Heat Exchanger Technology.

[15] A. C. Patrao, I. Jonsson, C. Xisto, A. Lundbladh, and T. Grönstedt, *Compact heat exchangers for hydrogen-fueled aero engine intercooling and recuperation,* Applied Thermal Engineering **243**, 122538 (2024).

[16] Z. Huang, J. Ling, Y. Hwang, V. Aute, and R. Radermacher, *Airside heat transfer and friction characteristics of a 0.8mm diameter bare tube heat exchanger,* Heat Transfer Engineering **41**, 1720 (2020).

[17] A. Žukauskas, *Heat transfer from tubes in crossflow,* (1972) pp. 93–160.

[18] D. Krempus, F. Beltrame, M. Majer, C. De Servi, R. Vos, and P. Colonna, *ORC Waste Heat Recovery System for the Turboshaft Engines of Turboelectric Aircraft,* in *Proceedings of the Aerospace Europe Conference 2023 10th EUCASS 9th CEAS* (EUCASS, 2023) aerospace Europe Conference 2023 : Joint 10th EUCASS - 9th CEAS Conference, 10th EUCASS - 9th CEAS Conference ; Conference date: 09-07-2023 Through 13-07-2023.

[19] D. Bacellar, V. Aute, H. Zhiwei, and R. Radermacher, *Novel heat exchanger design using computational fluid dynamics and approximation assisted optimization,* ASHRAE Winter Conference , 1 (2015).

[20] I. Kaur and P. Singh, *State-of-the-art in heat exchanger additive manufacturing,* International Journal of Heat and Mass Transfer **178**, 121600 (2021).

[21] M. Brevoort and A. Tifford, *An experimental investigation of flow across tube banks,* National Advisory Committee for Aeronautics (1942).

[22] *VDI Heat Atlas, Second Edition*, VDI-Gesellschaft Verfahrenstechnik und Chemieingenieurwesen (Springer, 2010).

[23] E. Achenbach, *On the cross flow through in-line tube banks with regard to the effect of surface roughness,* Wärme und Stoffübertragung **4**, 152 (1971).

[24] E. Achenbach, *Heat transfer from smooth and rough in-line tube banks at high reynolds number,* International Journal of Heat and Mass Transfer **34**, 199 (1991).

[25] D. Traub, *Turbulent heat transfer and pressure drop in plain tube bundles,* Chemical Engineering and Processing: Process Intensification **28**, 173 (1990).

[26] S. Ishigai and E. Nishikawa, *Structure of gas flow and its pressure loss in tube banks with tube axes normal to flow,* Trans. JSME **43**, 3310–3319 (1977).

[27] S. AIBA, H. TSUCHIDA, and T. OTA, *Heat transfer around tubes in in-line tube banks,* Bulletin of JSME **25**, 919–926 (1982).

[28] S. Beale and D. Spalding, *Numerical study of fluid flow and heat transfer in tube banks with streamwise preiodic boundary conditions,* Transactions of the Canadian Society for Mechanical Engineering **22** (1998), 10.1139/tcsme-1998-0022.

[29] S. Beale and D. Spalding, *A numerical study of unsteady fluid flow in in-line and staggered tube banks,* Journal of Fluids and Structures **13**, 723 (1999).

[30] S. Benhamadouche, I. Afgan, F. Dehoux, and R. Manceau, *Unsteady rans and large eddy simulation of the flow and heat transfer in a wall bounded pin matrix,* (2012).

[31] P. Rollet-Miet, D. Laurence, and J. Freziger, *LES and RANS of Turbulent Flow in Tube Bundles,* International Journal of Heat and Fluid Flow **20**, 241 (1999).

[32] A. M. N. Elmekawy, A. A. Ibrahim, A. M. Shahin, S. Al-Ali, and G. E. Hassan, *Performance enhancement for tube bank staggered configuration heat exchanger – cfd study,* Chemical Engineering and Processing - Process Intensification **164**, 108392 (2021).

[33] C. K. Mangrulkar, A. S. Dhoble, S. G. Chakrabarty, and U. S. Wankhede, *Experimental and CFD prediction of heat transfer and friction factor characteristics in cross flow tube bank with integral splitter plate,* International Journal of Heat and Mass Transfer **104**, 964 (2017).

[34] *Air viscosity: Sutherland's formula, national aeronautics and space administration,* (1999).

[35] T. D. Economon, F. Palacios, S. R. Copeland, T. W. Lukaczyk, and J. J. Alonso, *SU2: An Open-Source Suite for Multiphysics Simulation and Design,* AIAA Journal **54**, 828 (2016), https://doi.org/10.2514/1.J053813 .

[36] F. Palacios, M. Colonno, A. Aranake, A. Campos, S. Copeland, T. Economon, A. Lonkar, T. Lukaczyk, T. Taylor, and J. Alonso, *Stanford university unstructured (su2): An open-source integrated computational environment for multi-physics simulation and design,* (2013) https://doi.org/10.2514/6.2013-287 .

[37] *ANSYS Fluent 12.0: Theory Guide*, ANSYS, Inc. (2009).

[38] P. Spalart and S. Allmaras, *A one-equation turbulence model for aerodynamic flows,* AIAA **439** (1992), 10.2514/6.1992-439.

[39] W. Jones and B. Launder, *The prediction of laminarization with a two-equation model of turbulence, ",* Intj. Heat Mass Transfer **5**, 301 (1973).

[40] K. Y. Chien, *Predictions of channel and boundary-layer flows with a low-reynolds-number turbulence model,* AIAA Journal **20**, 33 (1982), https://doi.org/10.2514/3.51043 .

[41] S. A. Orszag, V. Yakhot, W. S. Flannery, F. E. Boysan, D. Choudhury, J. Maruzewski, and B. S. Patel, *Renormalization group modeling and turbulence simulations.* (1993).

[42] F. R. Menter, *Two-equation eddy-viscosity turbulence models for engineering applications,* AIAA Journal **32**, 1598 (1994), https://doi.org/10.2514/3.12149 .

[43] N. Kasagi, N. Shikazono, Y. Suzuki, and T. Oku, *Optimal design and assessment of high performance micro bare-tube heat exchangers,* Proc. 4th Conf. on Compact Heat Exchangers and Enhancement Technology for the Process Industries, Crete Island (2003).

[44] J. Tancabel, V. Aute, and R. Radermacher, *Review of shape and topology optimization for design of air-to-refrigerant heat exchangers,* (2018).

[45] D. Simanowitsch, A. Sudhi, A. Theiß, C. Badrya, and S. Hein, *Comparison of gradient-based and genetic algorithms for laminar airfoil shape optimization,* (2021).

[46] R. Matos, J. Vargas, T. Laursen, and F. Saboya, *Optimization study and heat transfer comparison of staggered circular and elliptic tubes in forced convection,* International Journal of Heat and Mass Transfer **44**, 3953 (2001).

[47] *Three-dimensional optimization of staggered finned circular and elliptic tubes in forced convection,* International Journal of Thermal Sciences **43**, 477 (2004).

[48] N. E. Gharbi, A. Kheiri, M. E. Ganaoui, and R. Blanchard, *Numerical optimization of heat exchangers with circular and non-circular shapes,* Case Studies in Thermal Engineering **6**, 194 (2015).

[49] J. Tancabel, V. Aute, E. Klein, C.-Y. Lee, Y. Hwang, J. Ling, J. Muehlbauer, and R. Radermacher, *Multi-scale and multi-physics analysis, design optimization, and experimental validation of heat exchangers utilizing high performance, non-round tubes,* Applied Thermal Engineering **216**, 118965 (2022).

[50] T. Albring, M. Sagebaum, and N. Gauger, *Efficient aerodynamic design using the discrete adjoint method in su2,* (2016).

[51] M. Giles and N. Pierce, *An introduction to the adjoint approach to design,* Flow, Turbulence and Combustion **65** (2000), 10.1023/A:1011430410075.

[52] J. Morgenstern, M. Buonanno, and F. Marconi, *Full configuration low boom model and grids for 2014 sonic boom prediction workshop,* 51st AIAA Aerospace Sciences Meeting including the New Horizons Forum and Aerospace Exposition 2013 (2013).

[53] N. Anand, S. Vitale, M. Pini, and P. Colonna, *Assessment of ffd and cad-based shape parametrization methods for adjoint-based turbomachinery shape optimization.* (2018).

[54] U. Kucuk and I. Tuncer, *Adjoint based shape optimization of an s-shaped duct with su2,* (2022).

[55] C. Venkatesan-Crome, R. Sanchez, and R. Palacios, *Aerodynamic optimization using fsi coupled adjoints in su2,* 7th European Conference on Computational Fluid Dynamics (2018).

[56] D. Kraft, *A Software Package for Sequential Quadratic Programming*, Deutsche Forschungs- und Versuchsanstalt für Luft- und Raumfahrt Köln: Forschungsbericht (Wiss. Berichtswesen d. DFVLR, 1988).

[57] K. Schittkowski, *The nonlinear programming method of wilson, han, and powell with an augmented lagrangian type line search function,* Numerische Mathematik **38**, 83 (1982).

[58] P. Gill, W. Murray, and M. Saunders, *Snopt: An sqp algorithm for large-scale constrained optimization*, SIAM Journal on Optimization **12**, 979 (2002).

[59] D.-R. Mohanty, A. Swain, and M. Das, *Thermal performance of mixed tube bundle composed of circular and elliptical tubes*, Thermal Science and Engineering Progress **5** (2018), 10.1016/j.tsep.2018.02.009.

[60] M. Towara, J. Lotz, and U. Naumann, *Discrete adjoint approaches for cht applications in openfoam*, in *Advances in Evolutionary and Deterministic Methods for Design, Optimization and Control in Engineering and Sciences*, edited by A. Gaspar-Cunha, J. Periaux, K. C. Giannakoglou, N. R. Gauger, D. Quagliarella, and D. Greiner (2021).

[61] *ANSYS Fluent Tutorial Guide*, ANSYS, Inc. (2017).